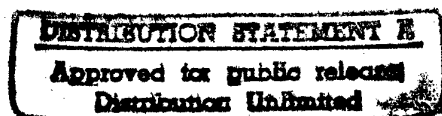


APPENDIX N° 1  
TO THE FINAL TECHNICAL REPORT  
CONTRACT DAJA N68171-95-C-9071  
(End of the First Year - 1996)

## NUMERICAL STUDY OF THE CRITICAL IMPACT VELOCITY IN SHEAR

by

M. Klósak & J.R. Klepaczko



UNIVERSITE DE METZ  
Institut Supérieur de Génie Mécanique et Productique  
Laboratoire de Physique et Mécanique des Matériaux  
U.R.A. C.N.R.S. N° 1215

Distribution unlimited

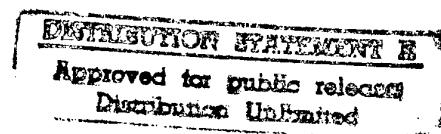
19970911 072

APPENDIX N° 1  
TO THE FINAL TECHNICAL REPORT  
CONTRACT DAJA N68171-95-C-9071  
(End of the First Year - 1996)

## NUMERICAL STUDY OF THE CRITICAL IMPACT VELOCITY IN SHEAR

by

M. Klósak & J.R. Klepaczko



DTIC QUALITY INSPECTED 4

UNIVERSITE DE METZ  
Institut Supérieur de Génie Mécanique et Productique  
Laboratoire de Physique et Mécanique des Matériaux  
U.R.A. C.N.R.S. N° 1215

Distribution unlimited

## ABSTRACT

Localization of plastic deformation in the form of shear bands is a very common failure mode in many materials. At high strain rates plastic deformation becomes nearly adiabatic which leads to the local heating of a material and, as a consequence, to the softening and formation of the adiabatic shear bands. At impact velocities of the order of 100 m/s the Critical Impact Velocity (CIV) in shear occurs. The superposition of adiabatic shear banding and adiabatic plastic waves in shear is the main interest in this Report.

A numerical study of impact shearing of a layer has been performed by the FE code ABAQUS. It was intended to verify available experimental results for VAR 4340 steel, ~52 HRC, obtained by direct impact on the Modified Double Shear specimen, [1]. In particular, the numerical study has been focussed on the effect of the impact velocity including the phenomenon of the Critical Impact Velocity in shear. An infinite thin layer fixed at one end and with a small geometrical imperfection in the middle of its height was considered. The layer was submitted in the other end to different shear velocities, from quasi-static to impact, up to 180 m/s.

Two modes of shear deformation of the layer have been found: in the first mode all deformation concentrates in the middle of the layer, and in the second near the surface where the shear velocity is imposed. The CIV could be defined as a transition between those two modes. It has been shown that impact velocities higher than the CIV leads to a substantial reduction of the localization energy.

All FE calculations have been performed with constitutive relations specially developed to reflect behavior of VAR 4340 steel. Thermal coupling, strain hardening and rate sensitivity are accounted for. Introduction of the temperature-dependent strain hardening exponent has demonstrated the importance of the proper formulation of the constitutive relations for all thermal instability problems.

Overall good correlation with experimental results and physical intuition have been achieved.

## TABLE OF CONTENTS

Abstract .....	1
1. Introduction .....	3
2. Constitutive relations .....	4
3. Thermal coupling .....	7
4. Finite element modeling .....	8
5. Results of calculations .....	11
6. Analysis and discussion .....	14
References .....	18
Figure Legends .....	20
Figures 1 to 89	

## 1. INTRODUCTION

Recent experiments with the technique of impact shearing, [1], have confirmed existence of the Critical Impact Velocity in shear, caused by adiabatic localization of shear superimposed on plastic shear waves, [2,3]. Experimental confirmation of CIV in shear is quite recent, [2], but a preliminary numerical analysis for a simple case was reported earlier, [4].

Numerical studies of adiabatic shear banding are quite numerous and they will not be discussed here, however, only few studies are focussed on adiabatic instability and localization at wide range of the nominal strain rates in shear, [5,6,7]. With the imposed shear velocity  $V$  on the layer of thickness  $h_s$ , but without definition how this velocity is applied to the layer, it is impossible to numerically find the CIV in shear. The final result of such calculations is limited to the statement that an increase of the nominal strain rate in shear,  $\dot{\Gamma}_n = V/h_s$ , may lead to the minimum of the instability strain at specific nominal strain rate,  $\dot{\Gamma}_n \approx 10^3 \text{ s}^{-1}$  for a mild steel [5,6], and that the difference between the instability strain and the strain of the final localization increases as a function of the nominal strain rate  $\dot{\Gamma}_n$ .

In order to analyse the effect of the more realistic boundary conditions in velocity imposed on the thin layer, that is the velocity starts from ZERO at one end and reaches its final value  $V$  after a short rise-time, it was decided to perform a systematic FE study.

Thus, numerical investigations were carried out in order to gather more information on the phenomenon of adiabatic shear banding from one side and CIV from the other. FE program ABAQUS was chosen for that purpose. The version used was equipped with all necessary tools to conduct the non-linear, dynamic, temperature-coupled analysis.

It was intended to demonstrate on a simple model of a thin layer with geometrical imperfection the existence of CIV in shear. The layer analysed, shown in Fig. 43, was assumed as made of VAR 4340 steel, ~52 HRC, and was subjected to the imposed velocity  $V$  with a specific rise-time on the upper surface, while being constrained at the bottom. A small geometrical imperfection was assumed in the middle height of the layer. Demonstration of the FE modeling can be found in Chapter 4, whereas results of calculations and further discussion are presented in Chapters 5 and 6.

Constitutive relations applied in the problem were specially developed to model experimental results for VAR 4340 steel, [8,9], as well as some data for similar materials,

[10,11]. They reflect very well temperature coupling and strain rate sensitivity. Constitutive relations are thoroughly discussed in the next Chapter, in return, remarks about thermal coupling are assembled in Chapter 3.

## 2. CONSTITUTIVE RELATIONS

It is known that a precise constitutive relation is the main demand in the numerical codes. A model chosen reflects later the final results. In order to approximate adiabatic instabilities, localization and wave effects, constitutive relations must include strain hardening, rate sensitivity and a wide range of temperatures.

A constitutive relation was sought to reflect plastic behavior of VAR 4340 steel, ~52 HRC, at high strain rates and wide range of temperature. The following general form was chosen

$$\tau = f_1(T) [f_2(T)f_3(\Gamma) + f_4(\dot{\Gamma}, T)] \quad (1)$$

where  $\tau$  is the shear stress, and  $f_i$  are functions of plastic strain in shear  $\Gamma$ , shear strain rate  $\dot{\Gamma}$  and absolute temperature  $T$ . Relation (1) is treated as the first approximation to constitutive modeling. Further analyses have shown that the strain hardening rate  $\partial\tau/\partial\Gamma$  is temperature dependent, for example [12]. The final general form of the constitutive relation used in majority of calculations is

$$\tau = f_1(T) [f_2(T)f_3(\Gamma, T) + f_4(\dot{\Gamma}, T)] \quad (2)$$

The explicit expressions for eqs (1) and (2) are assumed as follows

$$\tau = \frac{\mu(T)}{\mu_0} \left[ B \left( \frac{T}{T_0} \right)^{-\nu} (\Gamma_0 + \Gamma_p)^n + \tau_0 \left( 1 - \frac{T}{D} \log \frac{\dot{\Gamma}_0}{\dot{\Gamma}} \right)^m \right] \quad (3)$$

where  $B$ ,  $\mu_0$ ,  $\nu$ ,  $n$ ,  $m$  are, respectively, the modulus of plasticity, the shear modulus at

$T=300$  K, the temperature index, the strain hardening exponent and the logarithmic rate sensitivity,  $T_0$ ,  $\Gamma_0$  and  $\dot{\Gamma}_0$  are normalization constants, and  $\mu(T)$  is given by

$$\mu(T) = \mu_0(1 - AT^* - CT^{*2}); \quad T^* = T - 300 \quad (4)$$

It should be noted that application of eq. (3) is restricted to  $T \geq 300$  K.

Both relations are distinguished by different form of the strain hardening exponent  $n$ . In the first approach, eq. (1),  $n$  was assumed as a constant throughout the analysis, whereas in the second approach, eq. (2),  $n(T)$  became a decreasing function of temperature in the form, [12]

$$n(T) = n_0 \left( 1 - \frac{T}{T_m} \right) \quad (5)$$

where  $n_0$  is the strain hardening exponent  $n$  at  $T=0$  K, and  $T_m$  is the melting temperature. This modification was found essential because of the high rate of strain hardening represented by a constant, temperature-independent  $n$  which is not true for steels, including VAR 4340. The structure of the constitutive relation, eq. (3), has some elements based on the materials science approach. First of all the level of stress is normalised by  $\mu(T)/\mu_0$  which takes into account the thermal softening of the crystalline lattice. The first expression in the brackets is simply the internal stress and the second one is the rate and temperature- dependent effective stress, [13].

Total number of constants in the eqs (3) is 12 and they are assembled in Table 1. Results of numerical simulations are mainly obtained with the modified version of the constitutive relation with  $n(T)$ , however, some results with the constant value of  $n$  were also produced, mainly, in order to make comparison of the FE results where both relations are used. All FE results are included in this Report. It should be noted that modification of the constitutive equation by  $n(T)$  changes only certain temperature-dependent terms (shadow boxes in Table 1), for instance both constitutive relations have identical strain rate sensitivity.

Table 1

Constant	Value $n = \text{const}$	Value $n(T)$	Unit
B	1493.1	1493.1	MPa
$\mu_0$	80769.0	80769.0	MPa
$\nu$	<b>0.1657</b>	<b>0.39</b>	-
<b>n</b>	<b>0.113</b>	<b>equation (5)</b>	-
m	2.7763	2.7763	-
$T_0$	300.0	300.0	K
$\Gamma_0$	$1.6 \cdot 10^{-3}$	$1.6 \cdot 10^{-3}$	-
$\Gamma_n$	$1.932 \cdot 10^{-4}$	$1.932 \cdot 10^{-4}$	$s^{-1}$
A	$5.047 \cdot 10^{-4}$	$5.047 \cdot 10^{-4}$	$K^{-1}$
C	$1.036 \cdot 10^{-7}$	$1.036 \cdot 10^{-7}$	$K^{-2}$
D	2914.2	2914.2	K
$\tau_0$	622.0	622.0	MPa

All constants were obtained to fit existing experimental results [8-11], for example Figs 1 and 2 show experimental curves for VAR 4340 steel, ~52 HRC, and Fig. 3 shows curves together with those obtained from eq. (3). In order to better illustrate the constitutive relation used, the constitutive surface is presented in 3D as the shear yield stress in function of temperature and logarithm of shear strain rate. The constitutive surface is shown in Fig. 4. Of course, the surface for the yield stress is practically the same for both cases of strain hardening. The effect of temperature and strain rate on stress is more intense at lower temperatures and at higher strain rates, this is typical behavior for steels. In order to demonstrate completely the stress-strain behavior at different temperatures and strain rates the series of cross-sections of the  $\tau(\Gamma, \dot{\Gamma}, T)$  surface is shown in the form of  $\tau(\Gamma)_{\dot{\Gamma}, T}$  in figures from Fig. 5 to Fig. 10. The cross-sections at increased temperatures represent the constitutive relation with the constant strain hardening exponent ( $n=\text{const}$ , Table 1). The effect of temperature, also for  $n=\text{const}$ , is shown at different levels of plastic strain,  $0 \leq \Gamma \leq 1.0$ , in figures from Fig. 11 to Fig. 16. Finally, the effect of strain rate at different temperatures is shown in figures from Fig. 17 to Fig. 22. This set of curves has been calculated for the constant strain hardening exponent  $n$ . It is demonstrated in figures  $\tau(\Gamma)$  calculated for temperatures higher than  $T=600$  K, Figs 8 to



10, that the strain hardening rate seems to be too high which is against experimental observations, [12]. Normally the strain hardening exponent  $n$  must be a decreasing function of temperature, [12]. Consequently, the second approach to modeling of VAR 4340 steel represents a linear decrease of  $n$  as a function of temperature, [12]. The comparison between these two cases is shown in Fig. 23 for  $n(T)$  assumed in the form of eq. (5). For example, for  $T=1000$  K and  $\Gamma=1$  the difference in the flow stress is  $\sim 30$  %. When temperatures are increased, changes of  $n(T)$  as a function of temperature do not introduce much change of the yield stress in comparison to  $n=\text{const}$ , as it is shown in Fig. 24.

A complete set of the cross-sections of the constitutive surface  $\tau(\Gamma, \dot{\Gamma}, T)$  has been repeated for the assumed temperature-sensitive  $n(T)$ , eq. (5). The results are shown in Figs 25 to 42; Figs 25 to 30 show  $\tau(\Gamma)$  curves in the range of temperatures  $300 \text{ K} \leq T \leq 800 \text{ K}$ ; Figs 31 to 36 show  $\tau(T)$  curves within the range of plastic strains  $0 \leq \Gamma \leq 1.0$ ; Figs 37 to 42 illustrate  $\tau(\log \dot{\Gamma})$  within the range of temperatures  $300 \text{ K} \leq T \leq 800 \text{ K}$ .

### 3. THERMAL COUPLING

Since a large part of the plastic work is converted into heat, the deformed material heats up. The increase of temperature as a function of strain due to adiabatic heating is discussed for example in [2,14]. If the flow stress  $\tau$  is assumed in the form of eq. (1), then it follows from the energy conservation law

$$\left( \frac{dT}{d\Gamma} \right)_A = \frac{[1 - \xi(\Gamma, T)]f_1(T)[f_2(T)f_3(\Gamma, T) + f_4(\dot{\Gamma}, T)]}{J\rho_0(T)C_v(T)} \quad (6)$$

where  $\xi(\Gamma, T)$  is the coefficient representing stored energy in the lattice,  $J$  is a conversion factor of mechanical energy into heat,  $\rho_0(T)$  is the density of the metal, and  $C_v(T)$  is its specific heat at constant volume. The stored energy of cold work is usually a small fraction of the total plastic work, [15], and the value of  $\xi$  does not exceed  $\sim 0.1$ . Thus, the coefficient of conversion  $\beta$  is defined as follows

$$\beta = 1 - \xi(\Gamma, T); \quad (7)$$

$\beta$  is assumed constant in the present calculations.

Since  $\rho_o(T)$  is only weakly dependent on temperature, it can be taken as a constant. Although exact expression for the specific heat  $C_v(T)$  is temperature-dependent, for example [17], at temperatures higher than  $T=300$  K it may be also assumed as a constant.

The balance of energy with the heat conduction leads to the following relation

$$\beta\tau \frac{\partial \Gamma}{\partial t} = \rho C_v \frac{\partial T}{\partial t} - \lambda \frac{\partial^2 T}{\partial y^2} \quad (8)$$

where  $y$  is the axis of the heat conduction and  $\lambda$  is the heat conductivity (Fourier constant). Material constants associated with the process of thermal coupling are shown in Table 2.

Table 2

Constant	Value	Unit
$\beta$	0.9	-
$\lambda$	38.0	W/mK
$\rho$	7890.0	kg/m <sup>3</sup>
$C_v$	460.0	J/kgK
$T_m$	1812.0	K

The characterization of thermal coupling given above permits for numerical analyses of all temperature-coupled problems as purely adiabatic as well as with a heat conduction.

#### 4. FINITE ELEMENT MODELING

The main target of the numerical analysis was to explain differences between experiment of impact shearing by the Modified Double Shear, [1], and previous numerical calculations by the finite difference scheme where the initial conditions were not precisely specified, [5,7]. More exactly, it was not specified in the previous calculations of how the imposed velocity was applied to the layer analysed. Although the inertia effect was accounted for in [5] and [7], the final result was that the instability shear strain as well as the final localization strain have increased as a function of the imposed velocity, even for very high nominal strain rates of the order  $5 \cdot 10^4 \text{ s}^{-1}$  ( $V=100 \text{ m/s}$  for the layer height  $h_s=2.0 \text{ mm}$ ). On the contrary, experiments with MDS specimens by direct impact have shown

existence of the Critical Impact Velocity in shear [2,3]. In case of VAR 4340 steel, ~52 HRC, the CIV was estimated around ~140 m/s or the nominal strain rate  $\dot{\Gamma}_n \approx 7 \cdot 10^4 \text{ s}^{-1}$ . It appears that plastic deformation trapping near the impact surface is due to superimposed effects of adiabatic shear banding and plastic shear waves, [4]. It is impossible to find the CIV numerically when the initial boundary conditions do not reflect exactly the real situation met in experiment.

It was intended to analyse the CIV triggered by the shear banding phenomenon with a simple geometry in the form of an infinite layer in x-direction and 2 mm high, attached at the bottom surface, and submitted to the shear velocity  $V$  in x-direction at the top surface. Fig. 43 illustrates the problem considered. In fact, only a part of the infinite layer was modeled, that is 0.5 mm along the direction of impact (x-direction). Those dimensions were found quite sufficient to approximate the real behavior of an infinite layer. This simplification has helped considerably to reduce the computation time.

The geometrical imperfection was defined using equation

$$W(y) = W_0 \left[ 1 + \delta_w \sin \left( \frac{\pi}{2} - 2\pi \frac{y}{h} \right) \right] \quad (9)$$

where  $\delta_w = 0.005$  is the geometry parameter, which constitutes the imperfection of 1 %, and  $W_0$  is the mean width of the layer.

Numerical analyses were performed by the FE numerical code ABAQUS Standard. The code ABAQUS offers dynamic analysis options for both linear and nonlinear problems which can be coupled with temperature. Dynamic integration operators are characterized as implicit or explicit. ABAQUS Standard uses implicit integration for non-linear dynamic simulations. The time step for implicit integration is chosen automatically on the basis of the "half-step residual" by monitoring the values of equilibrium residuals at  $t + \Delta t/2$  once the solution at  $t + \Delta t$  has been obtained. The accuracy of the solution may be assessed and the time step adjusted appropriately, [16].

In general, two finite element models were applied: 2 dimensional (2D) and 3 dimensional (3D). The plain strain behavior was assumed in both models. The plain strain condition was satisfied by imposing no displacement in the perpendicular direction (z-direction) in 3D model, and by using available "plain strain" elements in 2D model. Taking into account the fact of two expected shearing modes, two kinds of meshing were used for each case: the first one for shearing in the mid-layer, Fig. 44 for 3D and Fig. 46 for 2D, and

the second one for plastic shearing trapped at the upper surface, Fig. 45 for 3D and Fig. 47 for 2D. The model in 3D has rather a coarse mesh, whereas 2D model is a refined version of the 3D. Fig. 48 presents comparison of numerical results for  $V=20$  m/s obtained in the form of  $\tau_A(\Gamma_n)$  at  $y=0$  (top of the layer) for both meshes. A good agreement is found (except the highly advanced localization states) which means that the coarse model (much more economic) predicts well the instability deformation  $\Gamma_c$ , however, a refined mesh should be used to carry out simulation which leads to a more precise analysis of the shear banding. The height of elements in the region of expected shear band should be based on experimental results for quenched and tempered VAR 4340 steel, the estimate the shear band thickness was of about  $20 \mu\text{m}$ , [17].

Depending on the imposed velocity at  $y=0$ , the problem was considered either with heat conduction or adiabatic. The latter case leads to the modification of equation (8) due to disparition of the last term ( $\lambda=0$ ). ABAQUS provides both type of analysis, however, certain restrictions are imposed. Thus, in the analysis with heat conduction (fully coupled temperature-displacement problem) the inertia effects are neglected, on the other hand, the analysis with wave effects is assumed adiabatic.

Table 3 gives data for performed tasks. The impact velocity  $V$  was increased from  $V=2 \cdot 10^{-5}$  m/s up to 160 m/s by 8 steps. All calculations in this series were performed for the temperature-dependent exponent,  $n(T)$ .

In case of the quasi-static loading, treated with heat conduction, 1<sup>st</sup> degree thermal conditions were imposed at the bottom and top surfaces, that is a constant temperature of 300 K was assumed.

Shear velocity  $V(t)$  at  $y=0$  is applied in the specific manner: from value of 0 to maximum  $V_m$ . The total rise-time  $t_m$  is chosen according to the Gaussian cumulative distribution function depending on the impact velocity  $V$ . The mathematical form of the rise-time function is represented by eq. (10)

$$F(x) = \int_{x_{\min}}^x \frac{1}{\sqrt{2\pi\sigma^2}} \exp\left(-\frac{(X-m)^2}{2\sigma^2}\right) dX \quad (10)$$

Schematic representation of the rise-time function is shown in Fig. 49. Assumed rise times were as follows:  $t_m=10^{-2}$  s for  $V<1$  m/s,  $t_m=10^{-6}$  s for  $1 \leq V < 20$  m/s, and  $t_m=10^{-7}$  s for  $V \geq 20$  m/s. Values of parameters  $m$  and  $\sigma$  in eq. (10) are  $m=0.5$ ,  $\sigma=0.125$ .

Table 3

Impact velocity	Nominal strain rate	Nature of analysis	Type of mesh		Type of element	
V [m/s]	$\dot{\Gamma}_n [s^{-1}]$		2D	3D	2D	3D
$2 \cdot 10^{-5}$	$10^{-2}$	heat conduction	Fig. 46	Fig. 44	CPE4T	C3D8T
0.2	$10^2$	adiabatic	Fig. 46	Fig. 44	CPE4R	C3D8R
20.0	$10^4$	adiabatic	Fig. 46	Fig. 44	CPE4R	C3D8R
60.0	$3 \cdot 10^4$	adiabatic	Fig. 46	Fig. 44	CPE4R	C3D8R
80.0	$4 \cdot 10^4$	adiabatic	Fig. 46	Fig. 44	CPE4R	C3D8R
120.0	$6 \cdot 10^4$	adiabatic	Fig. 47	Fig. 45	CPE4R	C3D8R
130.0	$6.5 \cdot 10^4$	adiabatic	Fig. 47	Fig. 45	CPE4R	C3D8R
140.0	$7 \cdot 10^4$	adiabatic	Fig. 47	Fig. 45	CPE4R	C3D8R
160.0	$8 \cdot 10^4$	adiabatic	Fig. 47	Fig. 45	CPE4R	C3D8R

Legend to Table 3:

C3D8T - 8-node thermally coupled brick;

C3D8R - 8-node linear brick, reduced integration;

CPE4T - 4-node plain strain thermally coupled quadrilateral, bilinear displacement and temperature, reduced integration;

CPE4R - 4-node plain strain quadrilateral, reduced integration.

## 5. RESULTS OF CALCULATIONS

This part of the Report presents the final results obtained from the ABAQUS simulations. The graphs were chosen to be representative for observed phenomena. They are thoroughly discussed in Chapters 5 and 6.

Fig. 50 defines position of the analysed cross-sections called A and B which behavior is studied in some graphs. In addition, the keywords appearing in the graphs are explained below:

- Nominal shear strain  $\Gamma_n = \Delta x / h_s$ , where  $\Delta x$  is the displacement of the top surface (at  $y=0$ ) in x-direction, and  $h_s$  is the height of the layer ( $h_s=2$  mm);
- Plastic shear strain  $\Gamma_A$  is the current shear strain determined in the cross-section A;
- Plastic shear strain  $\Gamma_B$  is the current shear strain determined in the cross-section B;

- iv. Critical shear strain  $\Gamma_c$  is the strain corresponding to the condition  $\partial\tau_A/\partial\Gamma=0$  (maximum stress) and can be estimated from the curves  $\tau_A(\Gamma_n)$ ;
- v.  $\tau_A$  is the shear stress at  $y=0$ , usually determined in experiments.

The complete series of calculations was focused on analyses of the instability point as determined by  $\partial\tau_A/\partial\Gamma=0$  and conditions of localization for both cases of constitutive relation,  $n=\text{const}$  and  $n(T)$ . The main parameter in those calculations was the imposed velocity  $V$ . Ten values of  $V$  have been assumed: from  $V_1=2\cdot 10^{-5}$  m/s which gives the nominal strain rate  $\dot{\Gamma}_n=10^{-2}$  s $^{-1}$  up to  $V_{10}=180$  m/s and respectively  $\dot{\Gamma}_n=9\cdot 10^4$  s $^{-1}$ . All values of  $V$  along with the nominal strain rates and modifications in constitutive relations are given in Table 4.

Table 4

N°	Impact velocity	Nominal strain rate	n const	n (T)	Critical strain n=const	Critical strain n(T)
	V [m/s]	$\dot{\Gamma}_n$ [s $^{-1}$ ]			$\Gamma_c$	$\Gamma_c$
V <sub>1</sub>	2·10 <sup>-5</sup>	10 <sup>-2</sup>	+	+	∞	∞
V <sub>2</sub>	0.2	10 <sup>2</sup>	-	+		0.346
V <sub>3</sub>	20.0	10 <sup>4</sup>	+	+	0.228	0.163
V <sub>4</sub>	60.0	3·10 <sup>4</sup>	-	+		0.135
V <sub>5</sub>	80.0	4·10 <sup>4</sup>	-	+		0.201
V <sub>6</sub>	120.0	6·10 <sup>4</sup>	+	+	~0.003	~0.002
V <sub>7</sub>	130.0	6.5·10 <sup>4</sup>	-	+		~0.002
V <sub>8</sub>	140.0	7·10 <sup>4</sup>	-	+		~0.002
V <sub>9</sub>	160.0	8·10 <sup>4</sup>	+	+	~0.003	~0.002
V <sub>10</sub>	180.0	9·10 <sup>4</sup>	+	-	~0.003	

In addition, calculated values of the instability strain  $\Gamma_c$  are given for each velocity. In order to compare the effect of strain hardening exponent  $n$  on the instability strain  $\Gamma_c$ , both cases of constitutive relations, that is  $n=\text{const}$  and  $n(T)$ , were analysed. The comparisons were done for four velocities as it is indicated in Table 4 by the positive signs. The most important differences were found, as expected, between the final

localization strain. The thermal softening manifested by decrease of  $n(T)$  leads to much higher rate of localization. The comparison is given for  $V=20$  m/s in Figs 51 and 52, the ratio of localization strains is of the order  $\sim 1.7$ . Fig. 53 demonstrates that due to geometrical imperfection the localization occurs in the middle of the layer, that is in the cross-section B in Fig. 50. Although the nominal strain rate is  $\dot{\Gamma}_n=10^4$  s $^{-1}$  ( $V=20$  m/s) the displacement field, distributions of strain rate and temperature, Figs 54 and 55, are typically found during quasi-static loading. The Marciniak plot given in Fig. 56 confirms entirely this statement. Evolution of the local strain rates in cross-sections A and B as a function of the nominal shear strain  $\Gamma_n$  is shown in Fig. 57, again this figure confirms the hypothesis of quasi-static-like deformation field. It is interesting to note that the temperature rise in the cross-section B is quite substantial, about 400 K. The next calculations for  $n=\text{const}$  and  $n(T)$  were completed for  $V=120$  m/s ( $\dot{\Gamma}=6 \cdot 10^4$  s $^{-1}$ ). Figs 58 and 59 show  $\tau_A(t)$  and  $\tau_A(\Gamma_n)$  curves at  $y=0$ . Again there is a considerable difference in values of localization strains for  $n=\text{const}$  and  $n(T)$ , about  $\sim 0.36$  and  $\sim 0.16$ . The most important observation is that the  $\tau_A(\Gamma_n)$  curve changes substantially its shape. The maximum occurs at very small nominal strain,  $\Gamma_c$  is about 0.002, and the final stage of localization occurs at  $\Gamma_n \approx 0.16$ . Thus, the instability point is reached almost instantaneously with an extended process of localization. The most important is the COMPLETE change in the displacement field shown in Fig. 60. Besides more or less uniform deformation along the layer, large deformations occur NEAR the impact end. The change of the cross-sections from B to A where the localization occurs is clear demonstration of the existence of the Critical Impact Velocity in shear, or thermoplastic wave trapping. Figs 61 and 62 show strain rate and temperature distributions along the height of the layer ( $y$ -direction). The transition between the deformation fields from the cross-sections B to A is quite obvious. Strain rate near  $y=0$  reaches very high values of the order  $\sim 7 \cdot 10^5$  s $^{-1}$  at the latest stage of localization. The increase of temperature is the highest also near  $y=0$ , the order of 500 K. The Marciniak plot changes its shape, Fig. 63. After initial destabilization near cross-section B, the localization occurs in cross-section A ( $y=0$ ). This is also visible in Fig. 64 where strain rates  $\dot{\Gamma}_A$  and  $\dot{\Gamma}_B$  are plotted as a function of the nominal strain  $\Gamma_n$ .

If the impact velocity  $V$  is still increased, for example up to 160 m/s, Figs 65 and 66, the shape of the  $\tau_A(t)$  and  $\tau_A(\Gamma_n)$  curves change completely, this occurs for both cases:

strain is completely localized near cross-section A, and displacements along the height of the layer are very small. This is characteristic displacement field as it is shown in Fig. 67, when the CIV is exceeded.

The case of  $V=180$  m/s was studied only for  $n=\text{const}$ . The distribution of strain rates along and near cross-section A is shown in Fig. 68 for three instants. The distributions of temperature is shown in Fig. 69 for the same time intervals. All deformations localize with a very high strain rate near  $y=0$  (cross-section A). This process leads to a very high increase of temperature near  $y=0$ , for example at  $t=0.162 \mu\text{s}$  the temperature exceeds 900 K. The behavior shown in Figs 68 and 69 is typical for the post-critical response of a layer or specimen during impact shearing. The distribution of strain rates and local velocities is similar to that reported in [4].

The Marciniak plot for  $V=180$  m/s shown in Fig. 70 differs much in comparison to the quasi-static strain evolution shown in Fig. 56. Deformation begins in cross-section A with a high strain rate, whereas deformation in cross-section B develops very slowly. Evolution of strain rates in A and B shown in Fig. 71 indicates that near the impact end the local strain rate exceeds value  $4 \cdot 10^6 \text{ s}^{-1}$ . The figures from 72 to 75 show results of consecutive deformation stages of the layer loaded by different velocities. This evolution is reflected in the shape of the  $\tau_A(t)$  curves, Figs 72 and 73, and also in the shape of  $\tau_A(\Gamma_n)$  curves, Figs 74 and 75.

The next part of this Report depicts evolution of particular variables as a function of the imposed velocity  $V$ .

## 6. ANALYSIS AND DISCUSSION

The sequence of previous figures clearly demonstrates a substantial evolution of shear stress, determined at  $y=0$  (the impact cross-section) as a function of time or the nominal shear strain  $\Gamma_n=V/h_s$  when the impact velocity is increased. Such curves can be determined from the MDS tests, [1]. It is of interest to compare such curves, that is  $\tau_A(\Gamma_n)$ , obtained numerically for nine different impact velocities. The comparison is shown in Figs 72 and 73 as a function of time, and in Figs 74 and 75 as a function of the nominal strain  $\Gamma_n$ . The curves shown in Figs 74 and 75 can be compared directly with experiments. Of course, in case of curve 1 the adiabatic instability does not occur because practically all



heat generated by plastic deformation is dissipated by thermal conduction. Beginning from  $V_2=0.2$  m/s ( $\dot{\Gamma}_n=100$  s<sup>-1</sup>) the adiabatic instability and localization are well defined. When the impact velocity is increased the instability point,  $(\partial\tau_A/\partial\Gamma_n)_{y=0}=0$ ,  $\Gamma_n=\Gamma_{nc}$ , translates into smaller strains, but the strain difference between instability and localization strains increases, this has been also found in [7]. Above impact velocities  $\sim 50$  m/s a competition between two mechanisms of localization occurs as it is shown in Figs 53 and 54 and Figs 60 and 61. This combination of mechanisms is manifested by the first peak of stress, a minimum and typical localization. Such behavior is clearly visible in Figs 72 and 74 for  $V_4=60$  m/s and  $V_5=80$  m/s. It is interesting to note that for velocities higher than  $\sim 50$  m/s the initial slopes of the  $\tau_A(\Gamma_n)$  curves are not equal to the elastic shear modulus  $\mu$ . The slopes found above 50 m/s are much steeper than  $\mu$ . The range of high impact velocities is shown in Fig. 75. Since within this range of impact velocities the localization occurs near  $y=0$  the first peak of stress is associated with the instantaneous localization, or in other words, with the adiabatic wave trapping. The localization strain decreases rapidly when the impact velocity exceeds 110 m/s. The CIV for VAR 4340 steel estimated from experiments is  $\sim 140$  m/s, [8]. The curve  $\tau_A(\Gamma_n)$  for  $V_8=140$  m/s resembles the experimental curve shown in Fig. 2. The highest velocity analysed with the complete constitutive relation was 160 m/s. The curve  $\tau_A(\Gamma_n)$  for  $V_9$  appears as a sharp maximum with almost infinite slope, Fig. 75. This is the post critical behavior of adiabatic wave trapping when observed with the MDS tests.

The next step in the numerical analysis was to demonstrate how particular parameters, for example the local strain rate or temperature, change in cross-sections A and B as a function of the impact velocity  $V$ . Changes of the local strain rate in cross-sections A and B are shown in Figs 76 to 79 for different levels of the nominal strain  $\Gamma_n$ . At impact velocity  $V=20$  m/s ( $\dot{\Gamma}_n=10^4$  s<sup>-1</sup>) the local strain rates do not differ much, however, when the impact velocity exceeds  $\sim 100$  m/s the local strain rates increase substantially in cross-section A in comparison to the cross-section B. When the impact velocity exceeds the CIV, estimated as  $\sim 110$  m/s for  $n(T)$  and  $\sim 120$  m/s for  $n=\text{const}$ , the local strain rates are extremely high in cross-section A and diminish to zero in cross-section B for larger nominal strains  $\Gamma_n$ . It is also interesting to compare the increments of temperature in A and B for increasing impact velocities. This is shown in Figs 80 to 83. Of

course, for the impact velocity  $V=20$  m/s and in cross-section B, the temperature increase begins from  $\sim 330$  K at  $\Gamma_n=0.1$  and ends  $\sim 570$  K at  $\Gamma_n=0.7$ , Figs 80 and 83. In this cross-section the increases of temperature are even higher in comparison to the cross-section A. When the impact velocity approaches the CIV the increments of temperature in A are quite high, from  $T_A=580$  K for  $\Gamma_n=0.1$  to more than 900 K for higher values of  $\Gamma_n$ , Figs 81 to 83.

The effect of the impact velocity on the post-critical behavior of the layer is shown in Figs 84 and 85. The level of inercy of the layer is so high that the slope of the initial part of the curves  $\tau_s(\Gamma_n)$  determined in cross-section A is not any more equal to the elastic slope  $\mu$ . The slope normalised by  $\mu$ , the shear modulus, is shown in two scales,  $\log V$  in Fig. 84 and in the linear one, Fig. 85. The normalised slope diminishes starting from the impact velocity  $\sim 25$  m/s. The slope of almost zero appears when the velocity exceeds the CIV.

The most important demonstration of the consecutive phases of the layer deformation is shown in Figs 86 and 87. Within the region of relatively low velocities, called Zone 1, practically all localization occurs in the middle of the layer (cross-section B). The critical strain  $\Gamma_c$  diminishes rapidly from infinity for the isothermal case to finite values due to thermal coupling. Within Zone 2 there is a competition between deformation in the cross-sections A and B caused by the propagation of plastic shear waves. It is interesting to note that for velocities higher than  $\sim 75$  m/s the critical strain  $\Gamma_c$  slightly increases. This is caused by the interaction of plastic deformation around the geometrical defect with plastic waves emitted from the cross-section A.

Finally, when the CIV is reached localization occurs exclusively within the cross-section A, and at higher velocities the critical strain  $\Gamma_c$  approaches very small values. Adiabatic shearing occurs almost instantaneously in A.

Experiments performed with MDS specimens made of VAR 4340 steel, [8], clearly indicated on a decrease of the fracturing energy when the impact velocity was increased. In order to estimate this effect by the FE method the energies up to the constant value of the negative slope  $\partial\tau_A/\partial\Gamma_n \approx -7000$  MPa were calculated for increasing impact velocities. The results are shown in Figs 88 and 89. The energies were calculated as integral of  $\tau_s(\Gamma_n)$  curves for nine impact velocities  $V$ . A considerable reduction of deformation energy occurs when the impact velocity exceeds the CIV. In Fig. 89 are shown the energies as a

function of the logarithm of the nominal strain rate  $\dot{\Gamma}_n = V/h_s$ . Of course, the shape of the curves is similar to that of Fig.88. The drop of the energy is so high that a different scales should be used to show the energy level for velocities exceeding the CIV. The calculated ratio of the energy drop before and post CIV reaches value about ONE HUNDRED.

In conclusion, the effect of the CIV in shear must be taken into account in all fragmentation processes developed by impact, [18]. When the local velocity of sliding exceeds the CIV for a particular material the energy of fragmentation or perforation should diminish rapidly by interaction of the Adiabatic Shear Banding and the Critical Impact Velocity in shear. It has been demonstrated in this study that the FE technique is advanced enough in order to find more details on the mechanisms of fast plastic deformation coupled with temperature and plastic waves.

## REFERENCES

- [1] J.R.Klepaczko, An experimental technique for shear testing at high and very high strain rates. The case of mild steel, *Int. J. Impact Engng.* **15** (1994), 25.
- [2] J.R.Klepaczko, Plastic shearing at high and very high strain rates, *Proc. Conf. EURODYMAT 94, J. de Phys., IV, Coll. C8*, (1994), C8-35.
- [3] J.R.Klepaczko, Recent Progress in Testing of Materials in Impact Shearing, in: *Dynamic Fracture, Failure and Deformation, PVP-Vol. 300*, ASME, NY (1995), 165.
- [4] F.H.Wu and L.B.Freund, Deformation Trapping due to Thermoplastic Instability in One-dimensional Wave Propagation, *J. Mech. Phys. Solids*, **32** (1984), 119.
- [5] J.R.Klepaczko, P.Lipinski and A.Molinari, An analysis of the thermoplastic catastrophic shear in some metals, in: *Impact Loading and Dynamic Behavior of Materials*, DGM Informationsgesellschaft Verlag, Vol. 2 (1988), 695.
- [6] J.R.Klepaczko, Some results and new experimental technique in studies of adiabatic shear bands, *Arch. Mech.*, **46** (1994), 201.
- [7] J.R.Klepaczko and B.Rezaig, A numerical study of adiabatic shear banding in mild steel by dislocation mechanics based constitutive relations, *Mech. of Materials*, (1996), accepted.
- [8] J.R.Klepaczko, Experimental Investigation of Adiabatic Shear Banding at Different Impact Velocities, Final Technical Report, US Army European Res. Office, Contr. DAJA49-90-C-0052 (Jan. 1993).
- [9] J.G.Cowie, The Influence of Second-phase Dispersions on Shear Instability and Fracture Toughness of Ultrahigh Strength 4340 steel, US Army Mat. Tech. Lab. Report, MTL-TR 89-20 (March 1989).
- [10] L.W.Meyer and E.Staskewitsch, Mechanical Behaviour of Some Steels under Dynamic Loading, in: *Impact Loading and Dynamic Behaviour of Materials*, DGM Informationsgesellschaft Verlag, Vol. 1, (1988), 331.
- [11] S.Tanimura and J.Duffy, Strain Rate Effects and Temperature History Effects for Three Different Tempers of 4340 Steel, Brown Univ. Div. of Engng. Tech. Report N° DAAG 29-81-K-0121/4, Providence (1984).
- [12] J.R.Klepaczko, A practical stress-strain-strain rate-temperature constitutive relation of the power form, *J. Mech. Working Technology*, **15** (1987), 143.

- [13] J.R.Klepaczko, Modeling of structural evolution at medium and high strain rates, FCC and BCC metals, in: Constitutive Relations and Their Physical Basis, Proc. 8-th Risö Mater. Symp., Risö (1987), 387.
- [14] J.R.Klepaczko and J.Duffy, Strain Rate History Effects in Body-Centered-Cubic Metals, in: Mechanical Testing for Deformation Metal Development, ASTM STP 765, ASTM (1982), 251.
- [15] M.B.Bever, D.L.Holt and A.L.Titchener, The Stored Energy of Cold Work, in: Progress in Materials Science, Vol. 17, Pergamon Press, Oxford (1973).
- [16] ABAQUS Manual, Version 5.4, Hibbitt, Karlsson and Sorensen, Inc. (1994).
- [17] J.H.Beatty, L.W.Meyer, M.A.Meyers and S.Nemat-Nasser, Formulation of Controlled Adiabatic Shear Bands in AISI 4340 High Strength Steel, in: Shock Waves and High-Strain-Rate Phenomena in Materials, Marcel Dekker Inc., N.Y. (1992), 645.
- [18] D.C.Erlich, D.R.Curran and L.Seaman, Further Development of a Computational Shear Band Model, Report AMMRC-TR-80-3, SRI International, (March 1980).

## FIGURE LEGENDS

- Fig.1 Experimental curves for VAR 4330 steel at strain rates:  $\dot{\Gamma}=7.1 \cdot 10^{-4} \text{ s}^{-1}$  and  $\dot{\Gamma}=3.1 \text{ s}^{-1}$ .
- Fig.2 Experimental curves for VAR 4330 steel at strain rates:  $\dot{\Gamma}=1.12 \cdot 10^4 \text{ s}^{-1}$  and  $\dot{\Gamma}=1.97 \cdot 10^4 \text{ s}^{-1}$ .
- Fig.3 Comparison of experimental  $\tau=\tau(\Gamma)$  curves with the constitutive relation applied in ABAQUS.
- Fig.4 Surface of yield shear stress as a function of temperature and logarithm of strain rate, the case of the constant strain hardening exponent  $n$ .
- Fig.5 Shear stress vs. plastic strain for different strain rates at  $T=300 \text{ K}$ ;  $n=\text{const}$ .
- Fig.6 Shear stress vs. plastic strain for different strain rates at  $T=400 \text{ K}$ ;  $n=\text{const}$ .
- Fig.7 Shear stress vs. plastic strain for different strain rates at  $T=500 \text{ K}$ ;  $n=\text{const}$ .
- Fig.8 Shear stress vs. plastic strain for different strain rates at  $T=600 \text{ K}$ ;  $n=\text{const}$ .
- Fig.9 Shear stress vs. plastic strain for different strain rates at  $T=700 \text{ K}$ ;  $n=\text{const}$ .
- Fig.10 Shear stress vs. plastic strain for different strain rates at  $T=800 \text{ K}$ ;  $n=\text{const}$ .
- Fig.11 Shear stress vs. temperature for different strain rates at  $\Gamma_p=0$ ;  $n=\text{const}$ .
- Fig.12 Shear stress vs. temperature for different strain rates at  $\Gamma_p=0.05$ ;  $n=\text{const}$ .
- Fig.13 Shear stress vs. temperature for different strain rates at  $\Gamma_p=0.1$ ;  $n=\text{const}$ .
- Fig.14 Shear stress vs. temperature for different strain rates at  $\Gamma_p=0.2$ ;  $n=\text{const}$ .
- Fig.15 Shear stress vs. temperature for different strain rates at  $\Gamma_p=0.5$ ;  $n=\text{const}$ .
- Fig.16 Shear stress vs. temperature for different strain rates at  $\Gamma_p=1.0$ ;  $n=\text{const}$ .
- Fig.17 Shear stress as a function of logarithm of strain rate for different levels of plastic strain at  $T=300 \text{ K}$ ;  $n=\text{const}$ .
- Fig.18 Shear stress as a function of logarithm of strain rate for different levels of plastic strain at  $T=400 \text{ K}$ ;  $n=\text{const}$ .
- Fig.19 Shear stress as a function of logarithm of strain rate for different levels of plastic strain at  $T=500 \text{ K}$ ;  $n=\text{const}$ .
- Fig.20 Shear stress as a function of logarithm of strain rate for different levels of plastic strain at  $T=600 \text{ K}$ ;  $n=\text{const}$ .

- Fig.21 Shear stress as a function of logarithm of strain rate for different levels of plastic strain at  $T=700$  K;  $n=\text{const}$ .
- Fig.22 Shear stress as a function of logarithm of strain rate for different levels of plastic strain at  $T=800$  K;  $n=\text{const}$ .
- Fig.23 Comparison of  $\tau=\tau(\Gamma)$  curves for both constitutive relations,  $n=\text{const}$  and  $n(T)$ .
- Fig.24 Yield shear stress vs. temperature; comparison of both constitutive relations,  $n=\text{const}$  and  $n(T)$ .
- Fig.25 Shear stress vs. plastic strain for different strain rates at  $T=300$  K;  $n=n(T)$ .
- Fig.26 Shear stress vs. plastic strain for different strain rates at  $T=400$  K;  $n=n(T)$ .
- Fig.27 Shear stress vs. plastic strain for different strain rates at  $T=500$  K;  $n=n(T)$ .
- Fig.28 Shear stress vs. plastic strain for different strain rates at  $T=600$  K;  $n=n(T)$ .
- Fig.29 Shear stress vs. plastic strain for different strain rates at  $T=700$  K;  $n=n(T)$ .
- Fig.30 Shear stress vs. plastic strain for different strain rates at  $T=800$  K;  $n=n(T)$ .
- Fig.31 Shear stress vs. temperature for different strain rates at  $\Gamma_p=0$ ;  $n=n(T)$ .
- Fig.32 Shear stress vs. temperature for different strain rates at  $\Gamma_p=0.05$ ;  $n=n(T)$ .
- Fig.33 Shear stress vs. temperature for different strain rates at  $\Gamma_p=0.1$ ;  $n=n(T)$ .
- Fig.34 Shear stress vs. temperature for different strain rates at  $\Gamma_p=0.2$ ;  $n=n(T)$ .
- Fig.35 Shear stress vs. temperature for different strain rates at  $\Gamma_p=0.5$ ;  $n=n(T)$ .
- Fig.36 Shear stress vs. temperature for different strain rates at  $\Gamma_p=1.0$ ;  $n=n(T)$ .
- Fig.37 Shear stress as a function of logarithm of strain rate for different levels of plastic strain at  $T=300$  K;  $n=n(T)$ .
- Fig.38 Shear stress as a function of logarithm of strain rate for different levels of plastic strain at  $T=400$  K;  $n=n(T)$ .
- Fig.39 Shear stress as a function of logarithm of strain rate for different levels of plastic strain at  $T=500$  K;  $n=n(T)$ .
- Fig.40 Shear stress as a function of logarithm of strain rate for different levels of plastic strain at  $T=600$  K;  $n=n(T)$ .
- Fig.41 Shear stress as a function of logarithm of strain rate for different levels of plastic strain at  $T=700$  K;  $n=n(T)$ .
- Fig.42 Shear stress as a function of logarithm of strain rate for different levels of plastic strain at  $T=800$  K;  $n=n(T)$ .
- Fig.43 The infinite layer in x-direction with geometrical defect in the middle.

- Fig.44 Finite element mesh applied in ABAQUS code to simulate the plastic shearing in the middle of the layer - 2D model.
- Fig.45 Finite element mesh applied in ABAQUS code to simulate the plastic shearing at the upper surface of the layer - 2D model.
- Fig.46 Finite element mesh applied in ABAQUS code to simulate the plastic shearing in the middle of the layer - 3D model.
- Fig.47 Finite element mesh applied in ABAQUS code to simulate the plastic shearing at the upper surface of the layer - 3D model.
- Fig.48 Shear stresses determined at  $y=0$  vs. nominal strain for  $V=20$  m/s; comparison of results obtained by 2D and 3D with the ABAQUS code.
- Fig.49 Boundary conditions for shear velocity at  $y=0$ .
- Fig.50 Definition of the position of cross-sections A and B.
- Fig.51 Time history of shear stresses determined at  $y=0$  for impact velocity  $V=20$  m/s; comparison for two constitutive relations,  $n=\text{const}$  and  $n(T)$ .
- Fig.52 Shear stresses determined at  $y=0$  vs. nominal strain for impact velocity  $V=20$  m/s; comparison for two constitutive relations,  $n=\text{const}$  and  $n(T)$ .
- Fig.53 Deformed shape of the layer for impact velocity  $V=20$  m/s.
- Fig.54 Distribution of strain rates along the height of the layer at different times for  $V=20$  m/s.
- Fig.55 Distribution of temperature along the height of the layer at different times for  $V=20$  m/s.
- Fig.56 Plastic shear strain  $\Gamma_A$  in cross-section A vs. plastic shear strain  $\Gamma_B$  in cross-section B, shear velocity  $V=20$  m/s.
- Fig.57 Shear strain rate  $\dot{\Gamma}$  vs. nominal strain  $\Gamma_n$  at  $V=20$  m/s.
- Fig.58 Time history of shear stresses determined at  $y=0$  for impact velocity  $V=120$  m/s; comparison for two constitutive relations,  $n=\text{const}$  and  $n(T)$ .
- Fig.59 Shear stresses determined at  $y=0$  vs. nominal strain for impact velocity  $V=120$  m/s; comparison for two constitutive relations,  $n=\text{const}$  and  $n(T)$ .
- Fig.60 Deformed shape of the layer for impact velocity  $V=120$  m/s.
- Fig.61 Distribution of strain rates along the height of the layer at different times for  $V=120$  m/s.



- Fig.62 Distribution of temperature along the height of the layer at different times for  $V=120$  m/s.
- Fig.63 Plastic shear strain  $\Gamma_A$  in cross-section A vs. plastic shear strain  $\Gamma_B$  in cross-section B for shear velocity  $V=120$  m/s.
- Fig.64 Shear strain rate  $\dot{\Gamma}$  vs. nominal strain  $\Gamma_n$  for  $V=120$  m/s.
- Fig.65 Time history of shear stresses determined at  $y=0$  for impact velocity  $V=160$  m/s; comparison of two constitutive relations,  $n=\text{const}$  and  $n(T)$ .
- Fig.66 Shear stresses determined at  $y=0$  vs. nominal strain for impact velocity  $V=160$  m/s; comparison of two constitutive relations,  $n=\text{const}$  and  $n(T)$ .
- Fig.67 Deformed shape of the layer for impact velocity  $V=160$  m/s.
- Fig.68 Distribution of strain rates along the height of the layer at different times for  $V=180$  m/s.
- Fig.69 Distribution of temperature along the height of the layer at different times for  $V=180$  m/s.
- Fig.70 Plastic shear strain  $\Gamma_A$  in cross-section A vs. plastic shear strain  $\Gamma_B$  in cross-section B for shear velocity  $V=180$  m/s.
- Fig.71 Shear strain rate  $\dot{\Gamma}$  vs. nominal strain  $\Gamma_n$  at  $V=180$  m/s.
- Fig.72 Time history of shear stresses determined at  $y=0$  for the assumed shear velocities, range:  $V=20\div 80$  m/s.
- Fig.73 Time history of shear stresses determined at  $y=0$  for the assumed shear velocities, range:  $V=120\div 160$  m/s.
- Fig.74 Shear stresses determined at  $y=0$  vs. nominal strain for the assumed shear velocities, range:  $V=2\cdot 10^{-5}\div 80$  m/s.
- Fig.75 Shear stresses determined at  $y=0$  vs. nominal strain for the assumed shear velocities, range:  $V=120\div 160$  m/s.
- Fig.76 Strain rate in cross-sections A and B vs. logarithm of shear velocity for nominal strain  $\Gamma_n=0.1$ ;  $n=\text{const}$ .
- Fig.77 Strain rate in cross-sections A and B vs. logarithm of shear velocity for nominal strain  $\Gamma_n=0.3$ ;  $n=\text{const}$ .
- Fig.78 Strain rate in cross-sections A and B vs. logarithm of shear velocity for nominal strain  $\Gamma_n=0.5$ ;  $n=\text{const}$ .

- Fig.79 Strain rates in cross-sections A and B vs. logarithm of shear velocity for nominal strain  $\Gamma_n = 0.7$ ;  $n=\text{const.}$
- Fig.80 Profile of temperatures calculated in cross-sections A and B as a function of logarithm of shear velocity for nominal strain  $\Gamma_n = 0.1$ ;  $n=\text{const.}$
- Fig.81 Profile of temperatures calculated in cross-sections A and B as a function of logarithm of shear velocity for nominal strain  $\Gamma_n = 0.3$ ;  $n=\text{const.}$
- Fig.82 Profile of temperatures calculated in cross-sections A and B as a function of logarithm of shear velocity for nominal strain  $\Gamma_n = 0.5$ ;  $n=\text{const.}$
- Fig.83 Profile of temperatures calculated in cross-sections A and B as a function of logarithm of shear velocity for nominal strain  $\Gamma_n = 0.7$ ;  $n=\text{const.}$
- Fig.84 Normalised rigidity coefficient (inversed slope of the apparent  $\tau_s(\Gamma_n)$  lines) as a function of logarithm of shear velocity.
- Fig.85 Normalised rigidity coefficient (inversed slope of the apparent  $\tau_s(\Gamma_n)$  lines) as a function of shear velocity.
- Fig.86 Critical strain  $\Gamma_c$  vs. logarithm of the imposed velocity  $V$  determined from the ABAQUS simulations.
- Fig.87 Critical strain  $\Gamma_c$  vs. imposed velocity  $V$  determined from the ABAQUS simulations.
- Fig.88 Total plastic energy dissipated in the layer vs. logarithm of the impact velocity  $V$ .
- Fig.89 Total plastic energy dissipated in the layer vs. logarithm of the nominal strain rate.

FIGURES 1 TO 89

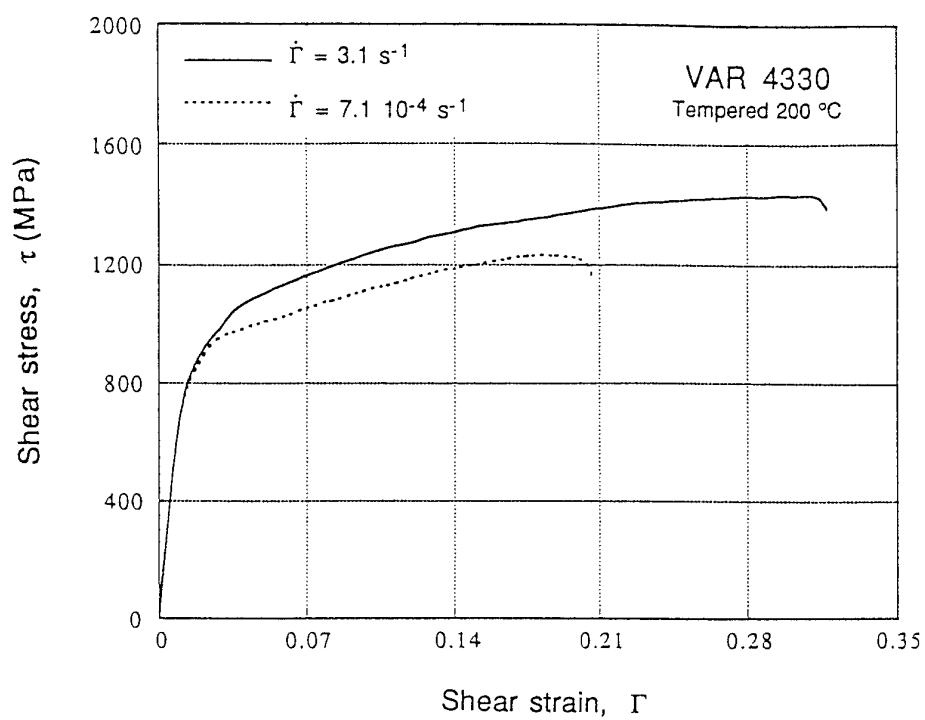


Fig. 1

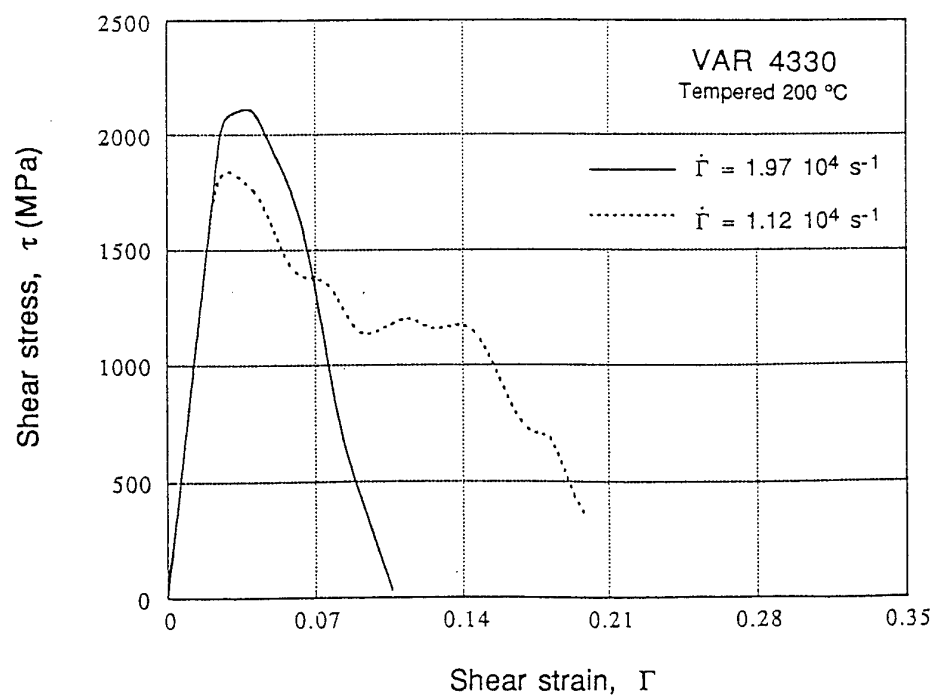


Fig. 2

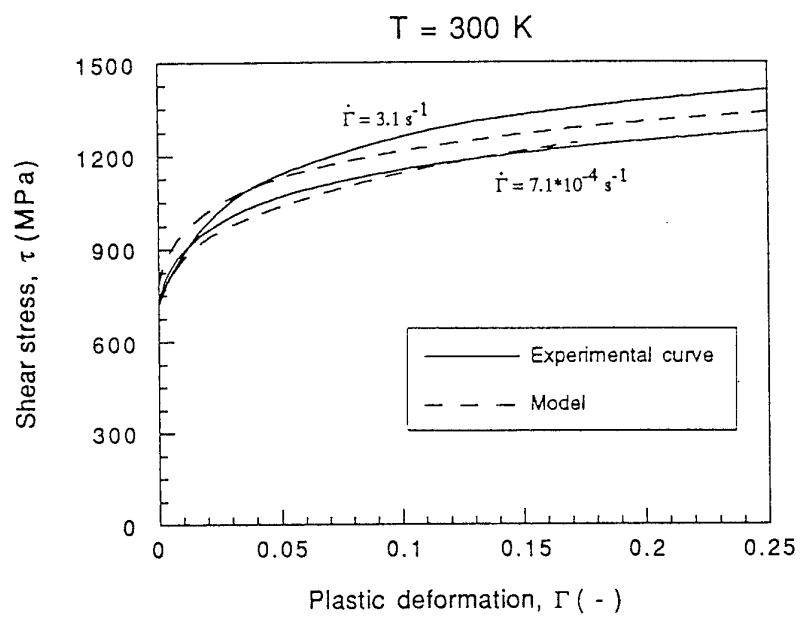


Fig. 3

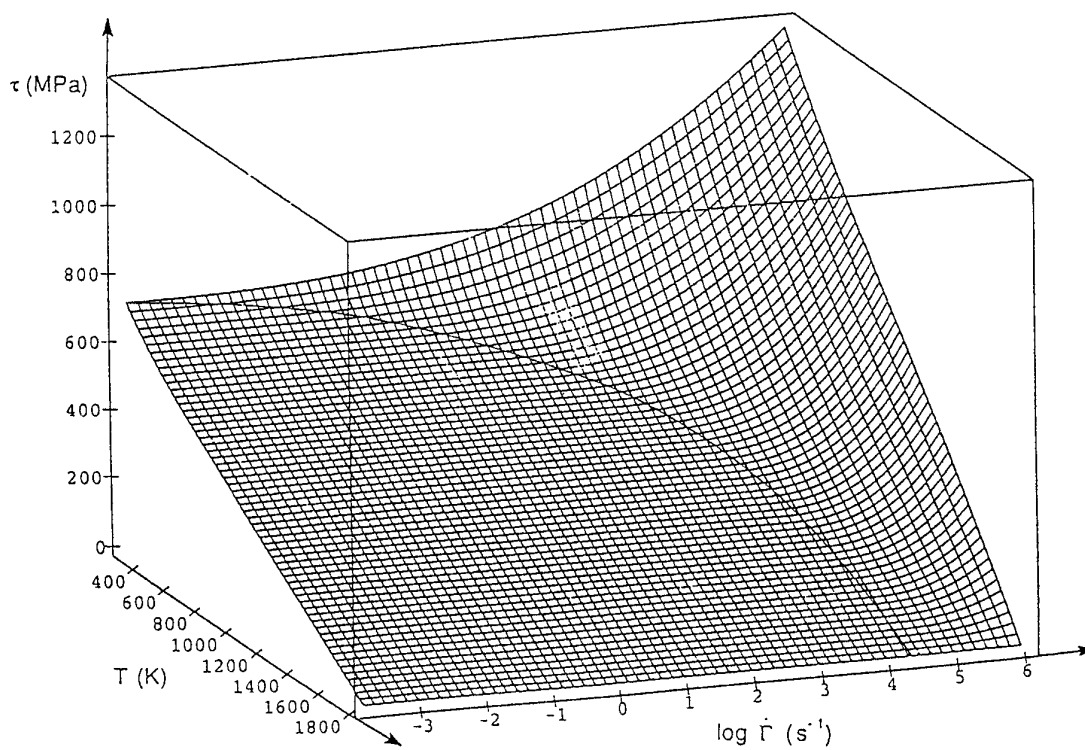


Fig. 4

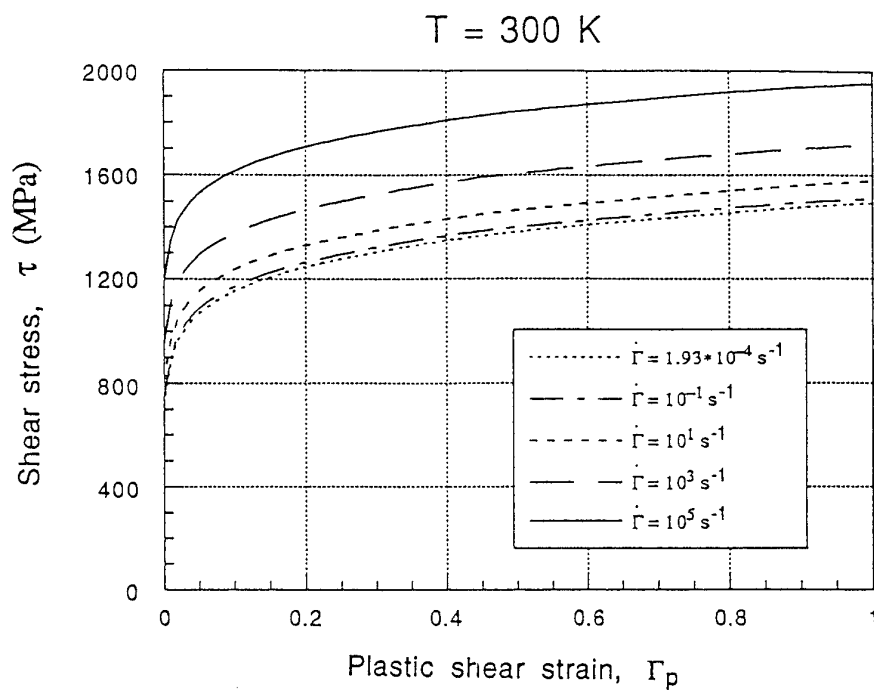


Fig. 5

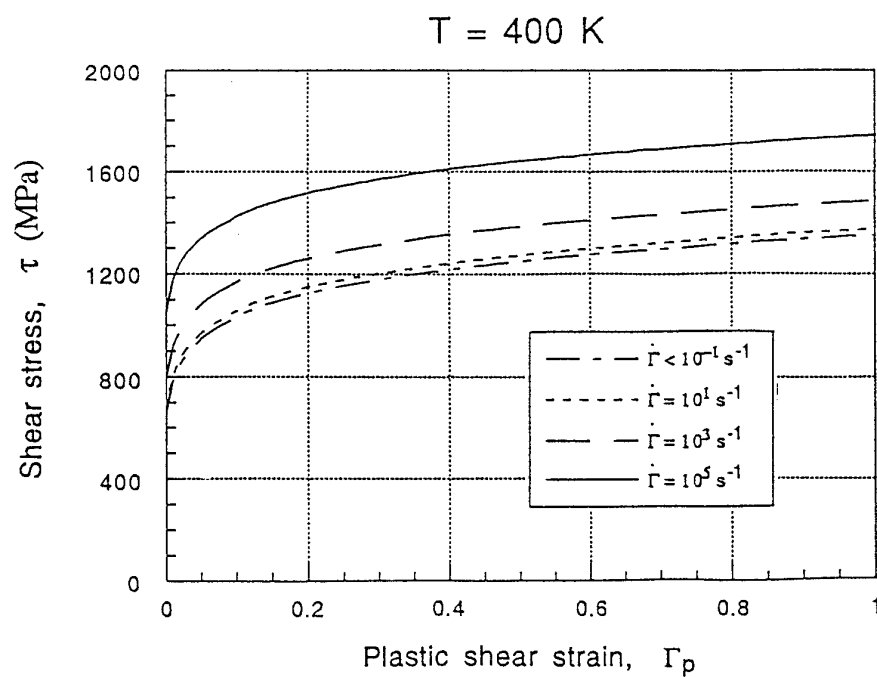


Fig. 6

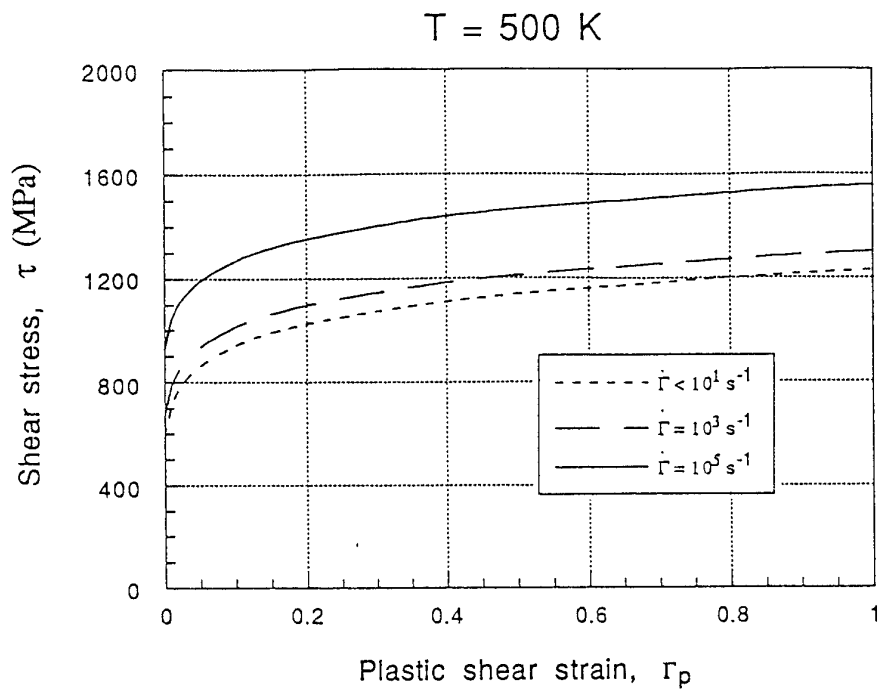


Fig. 7

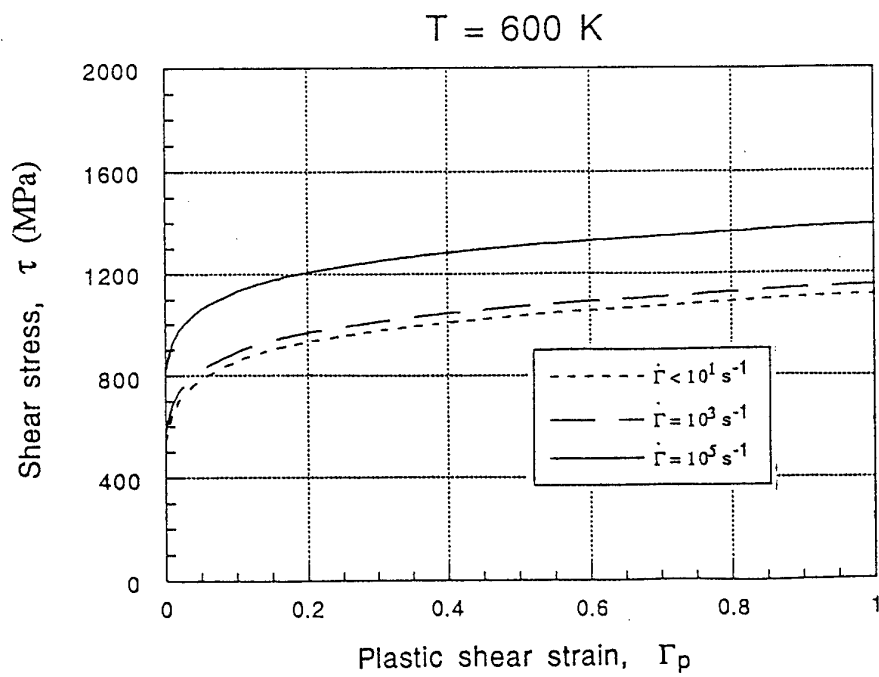


Fig. 8

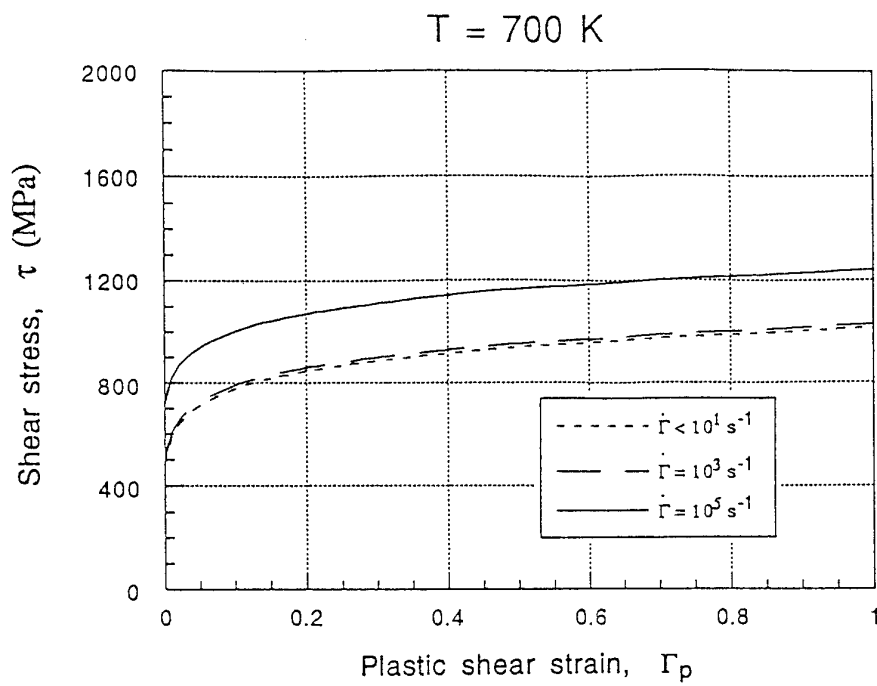


Fig. 9

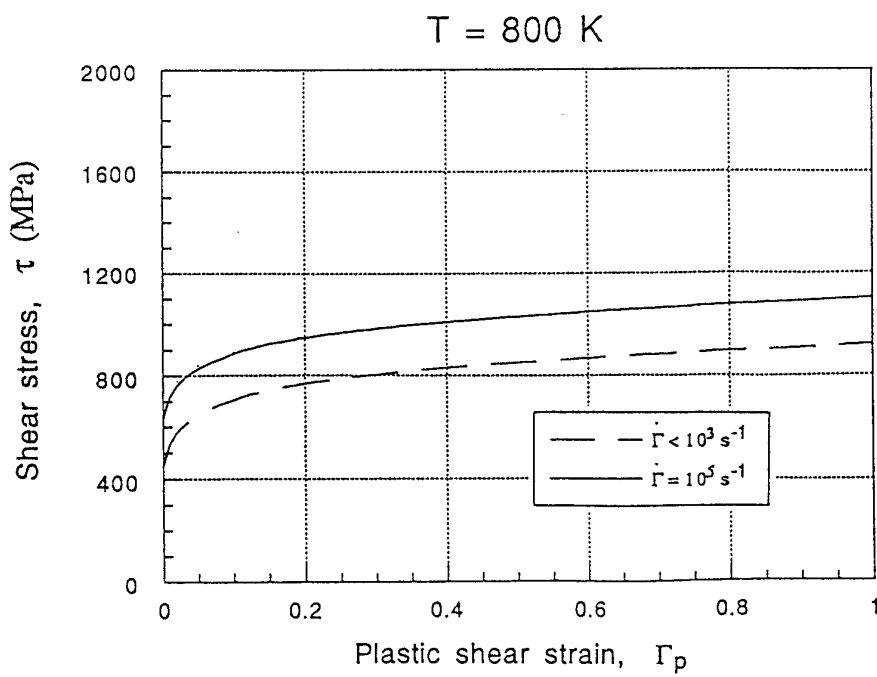


Fig. 10



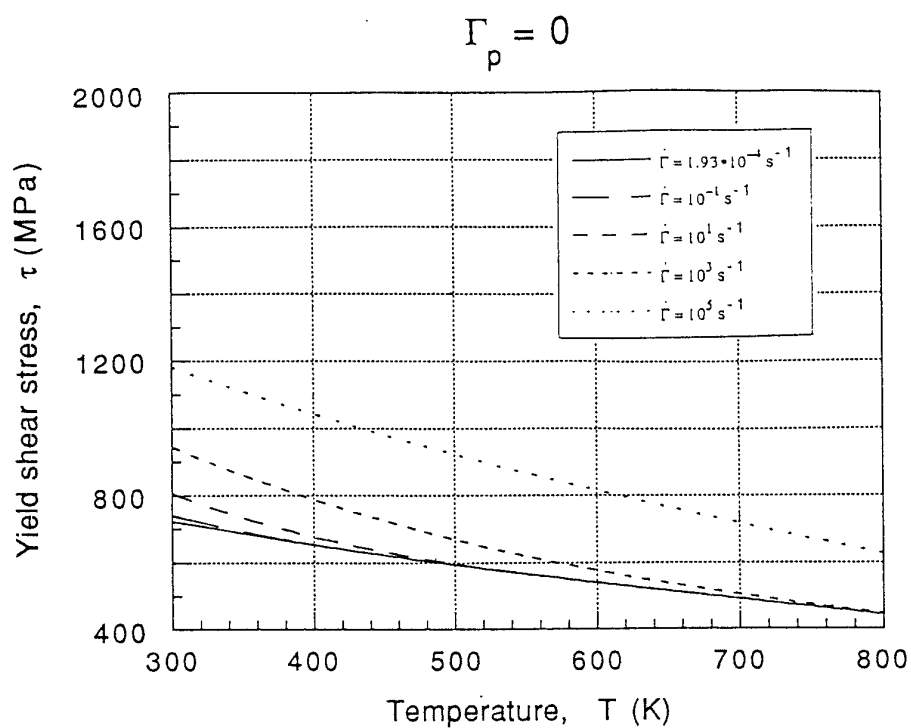


Fig. 11

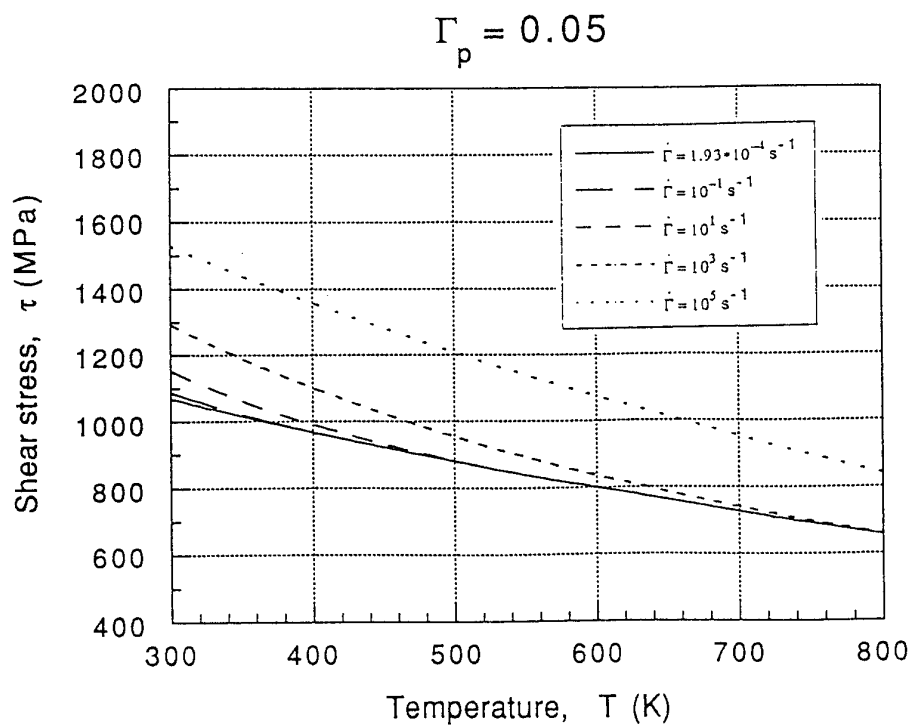


Fig. 12

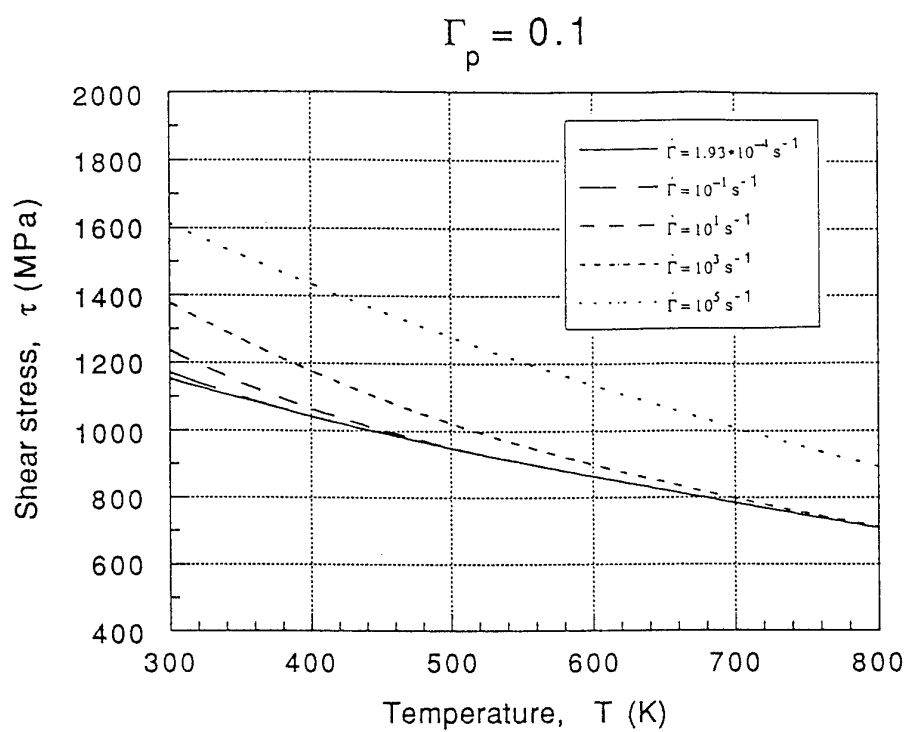


Fig. 13

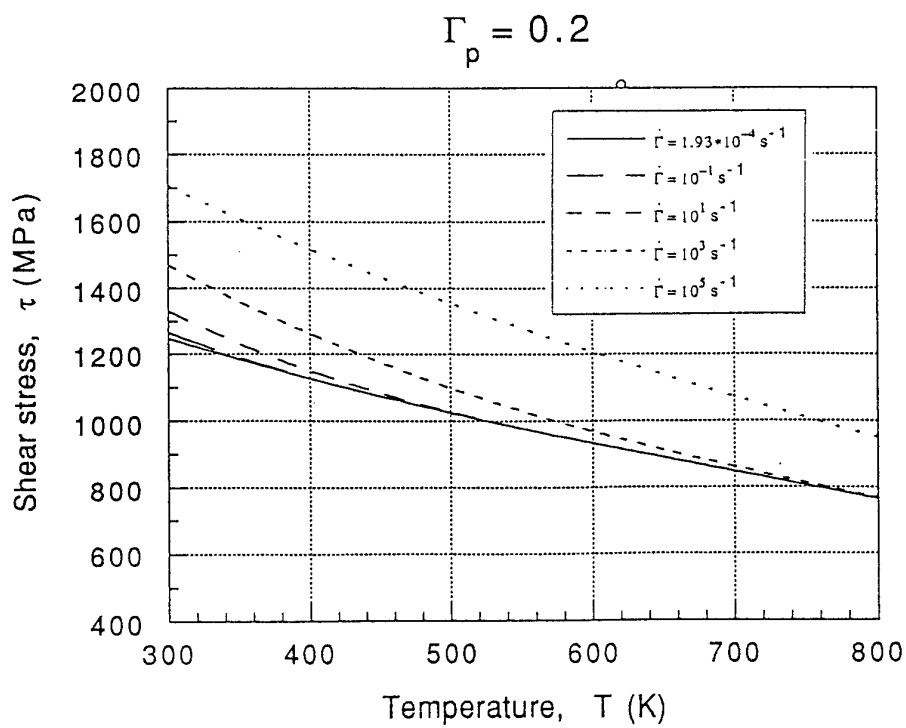


Fig. 14

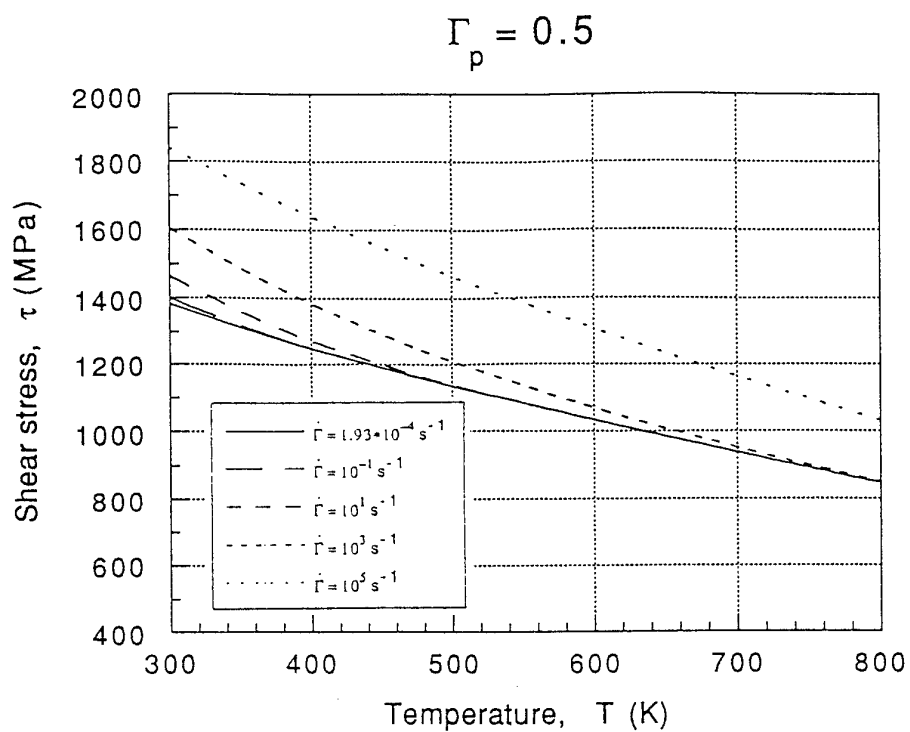


Fig. 15

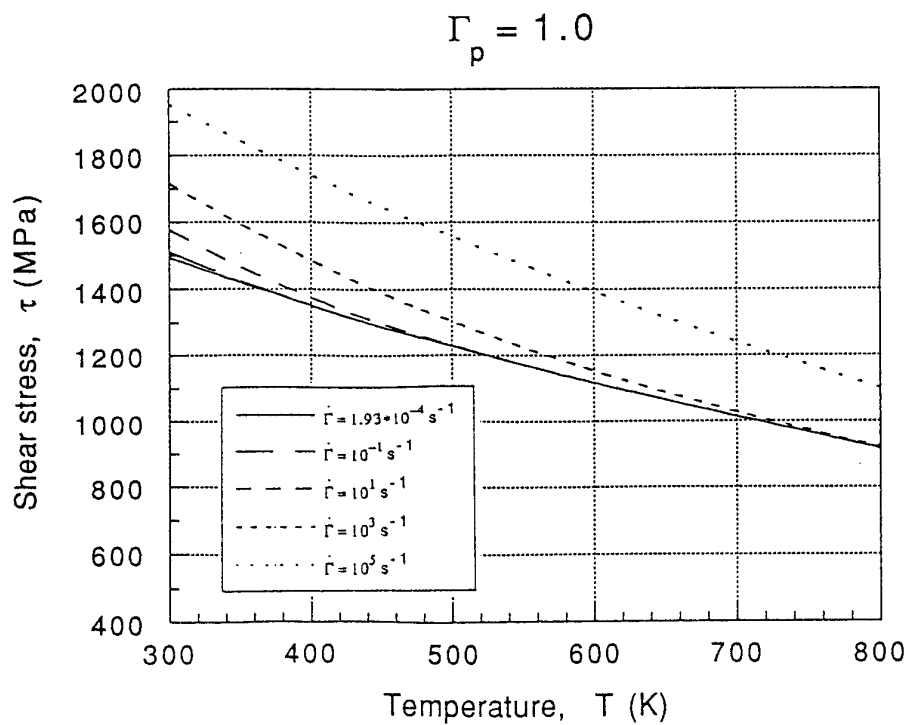


Fig. 16

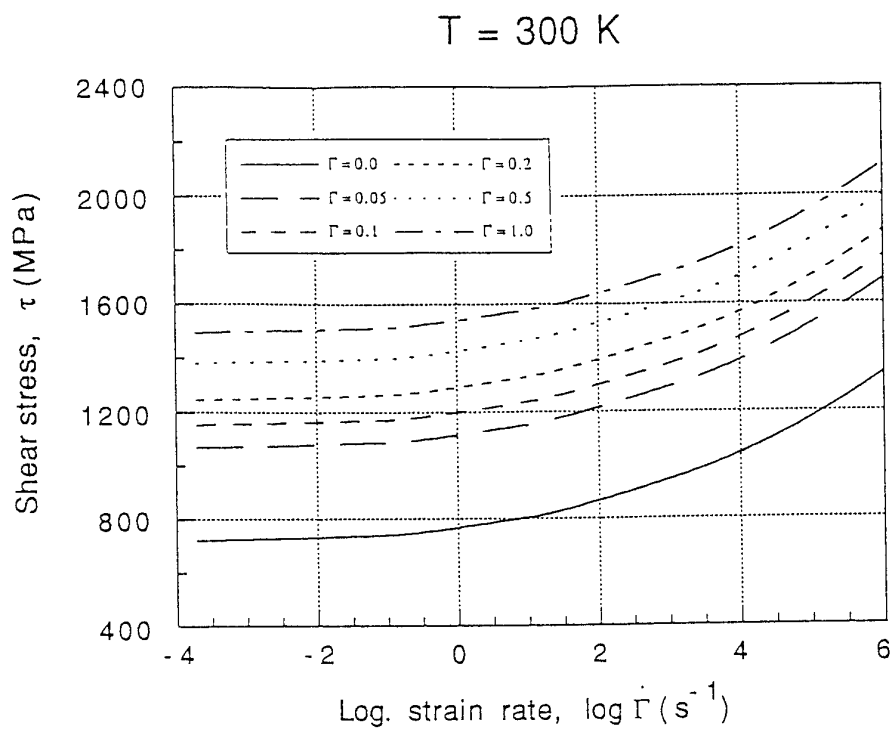


Fig. 17

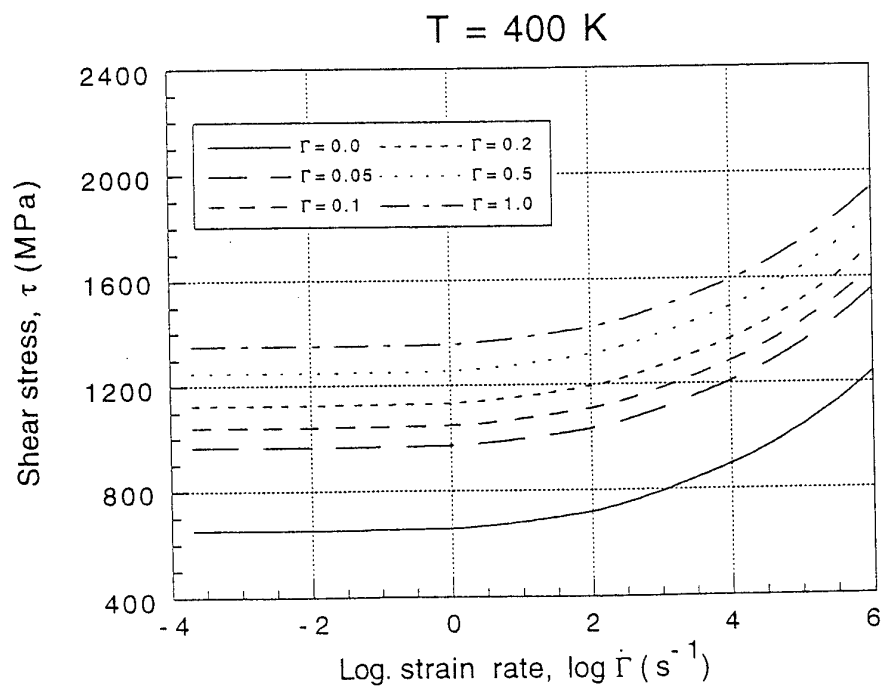


Fig. 18

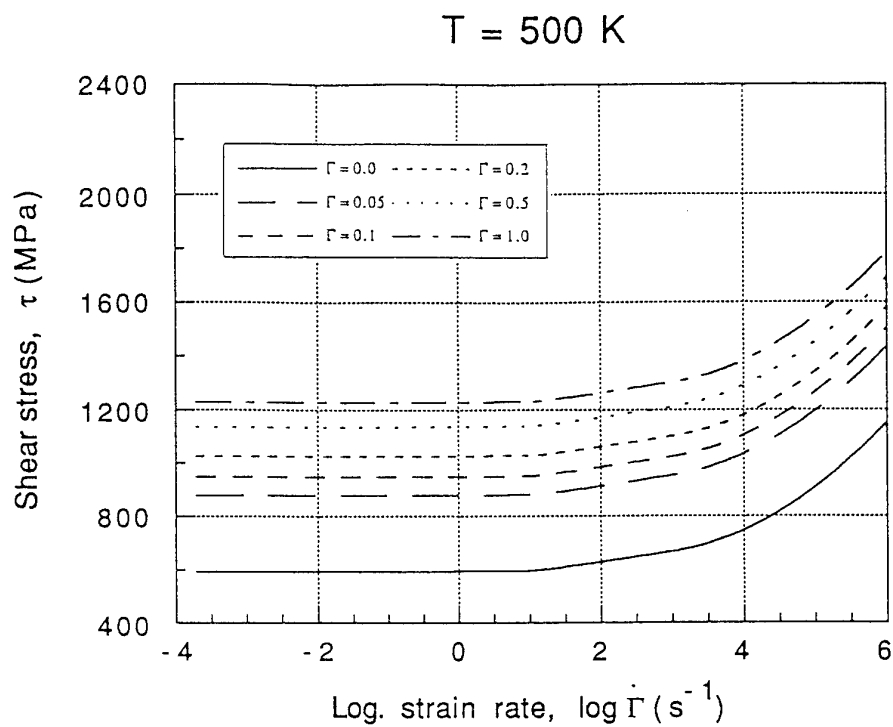


Fig. 19

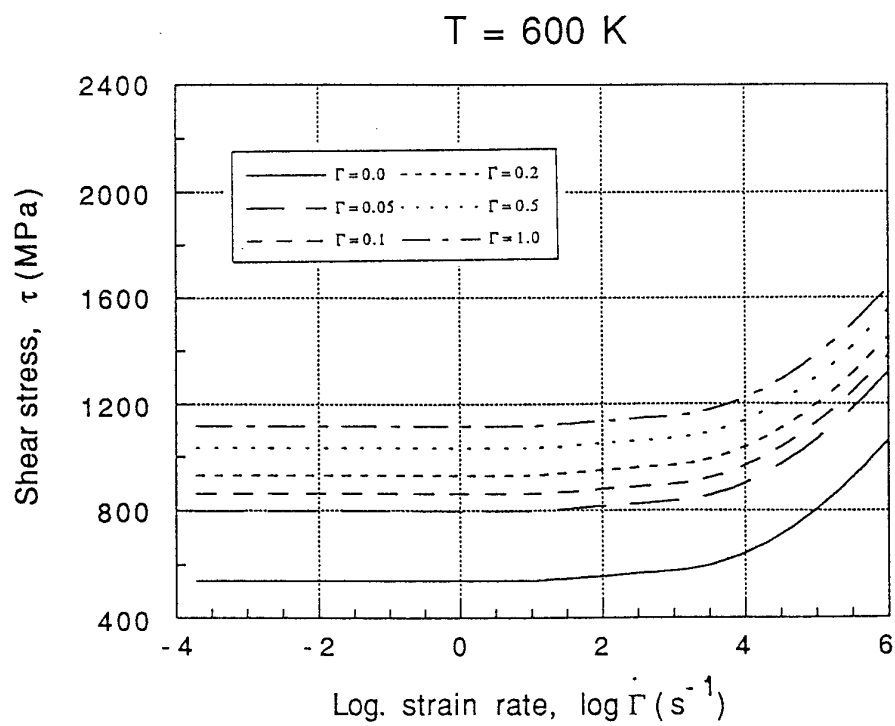


Fig. 20

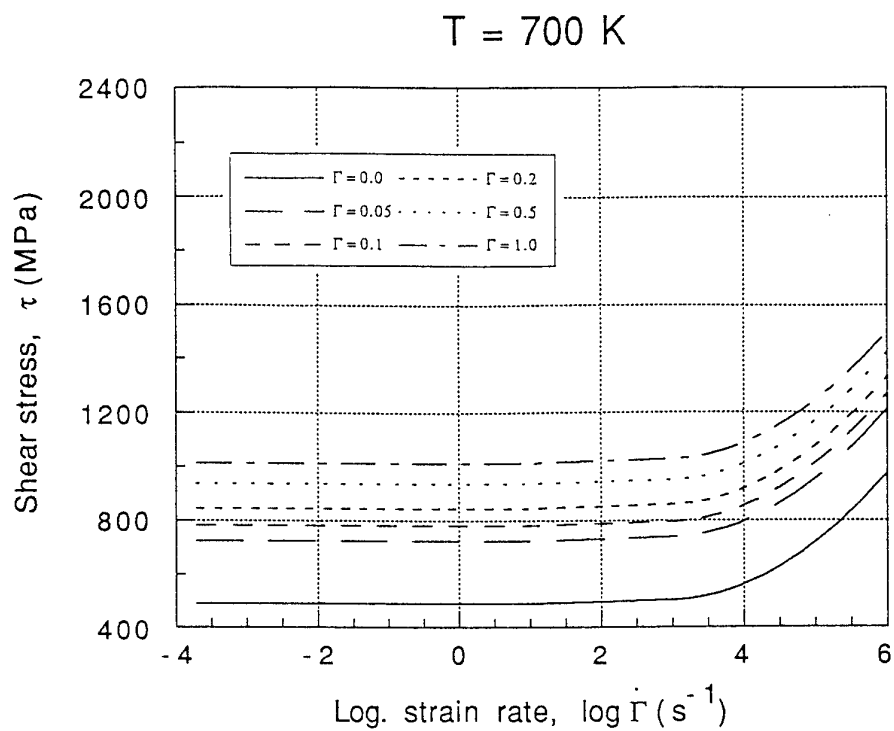


Fig. 21

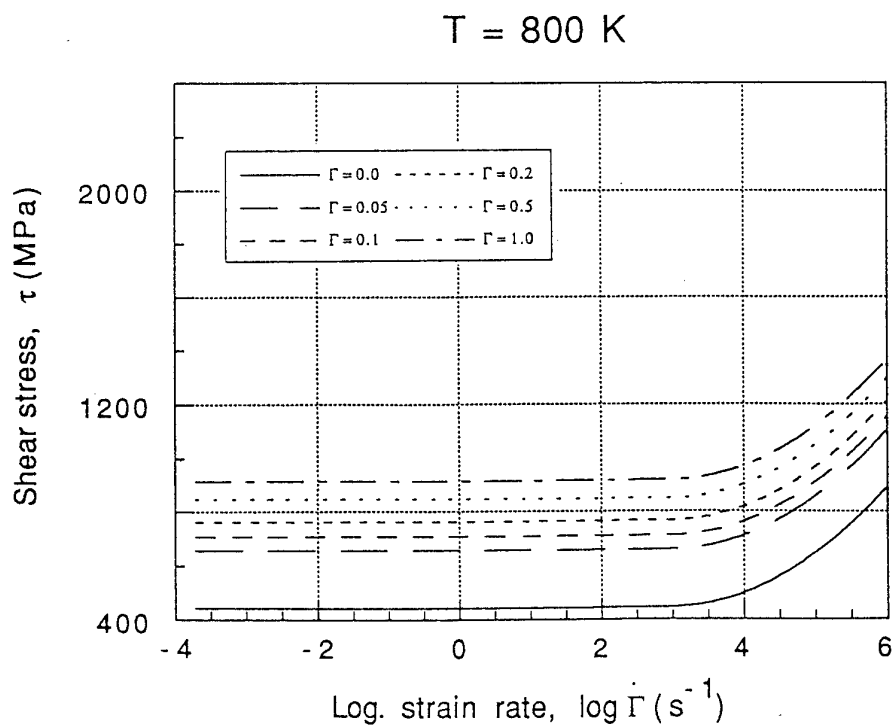


Fig. 22

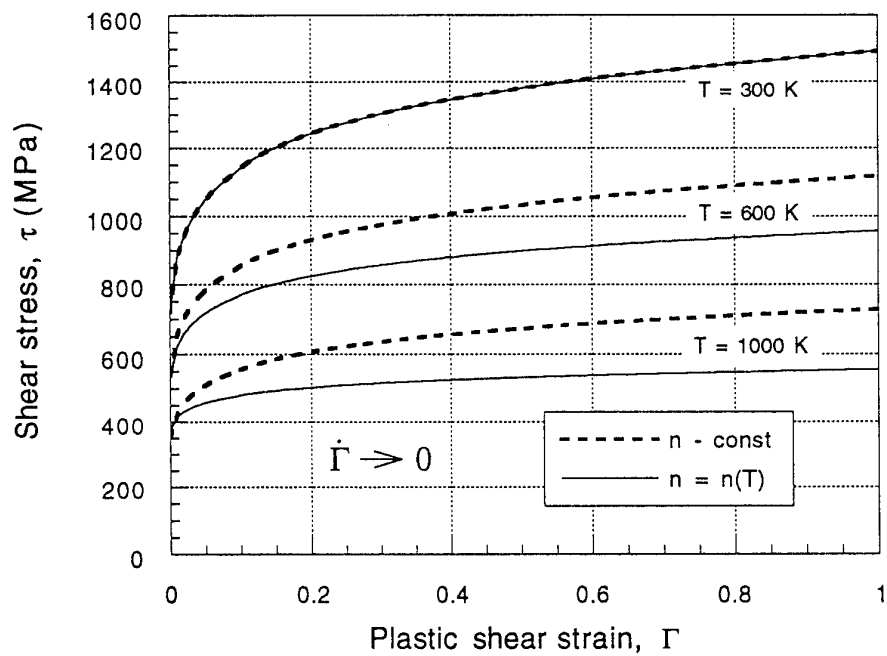


Fig. 23

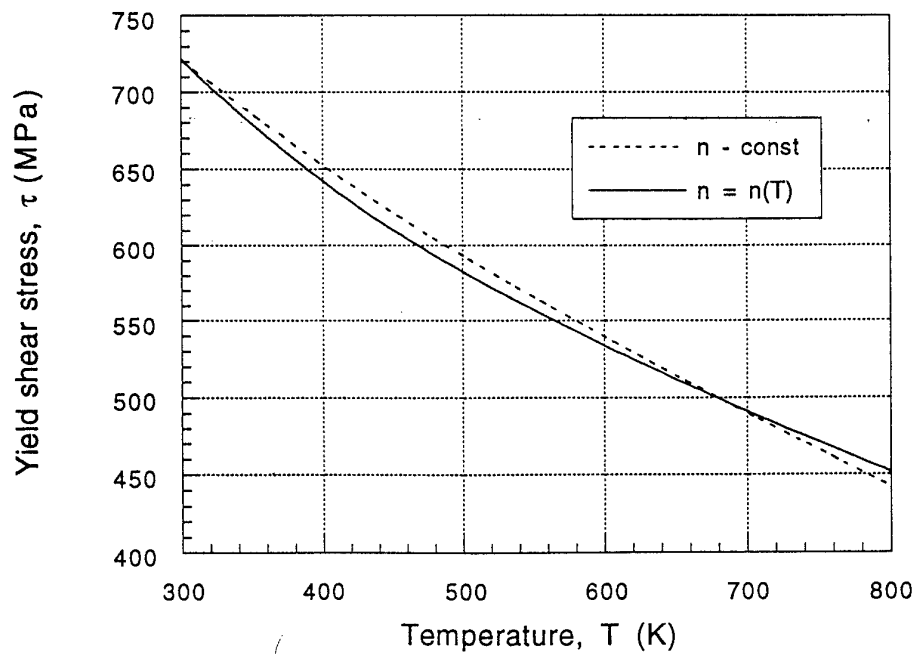


Fig. 24

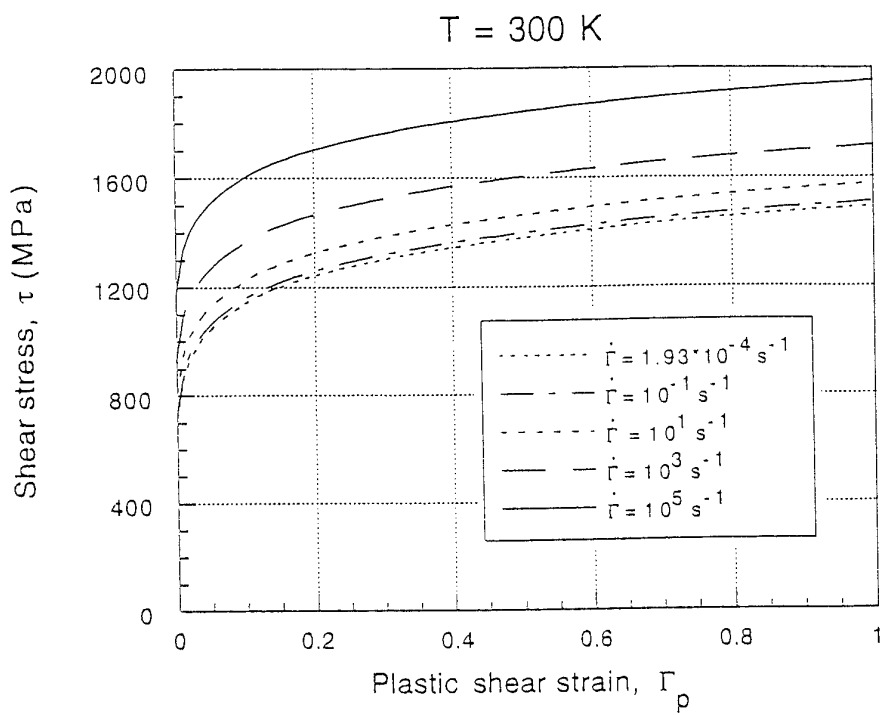


Fig. 25

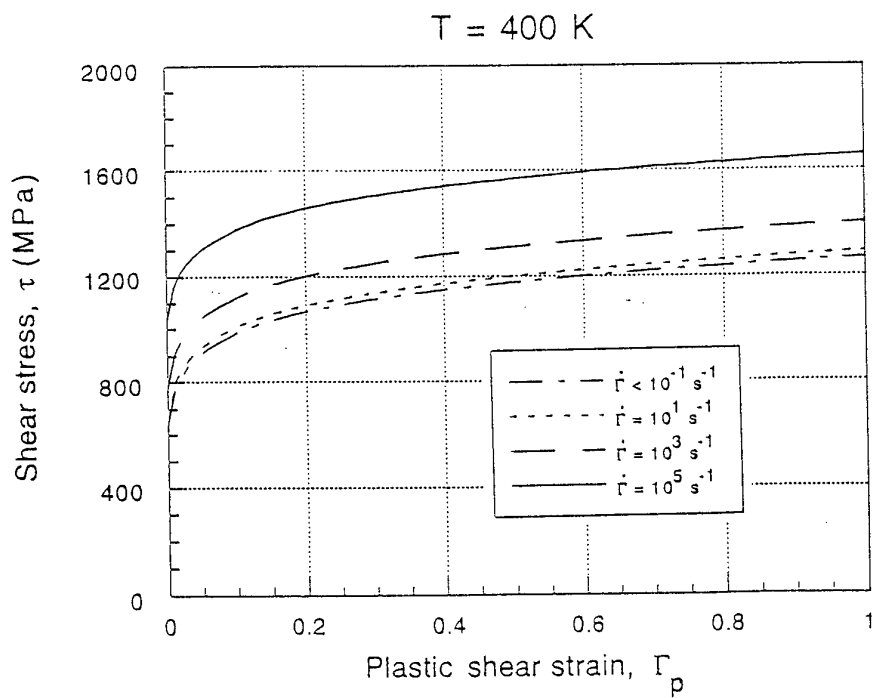


Fig. 26



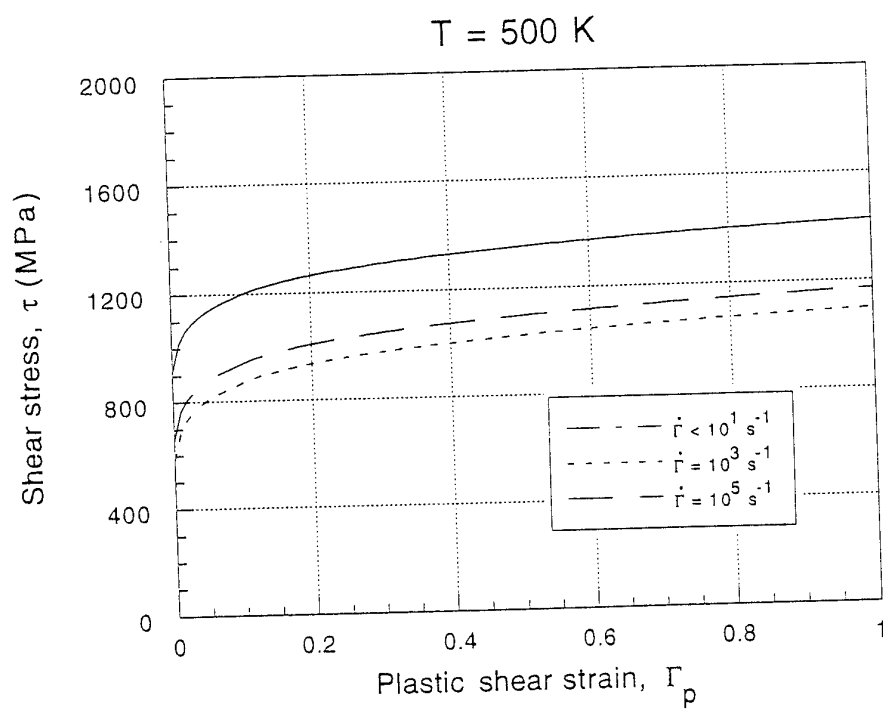


Fig. 27

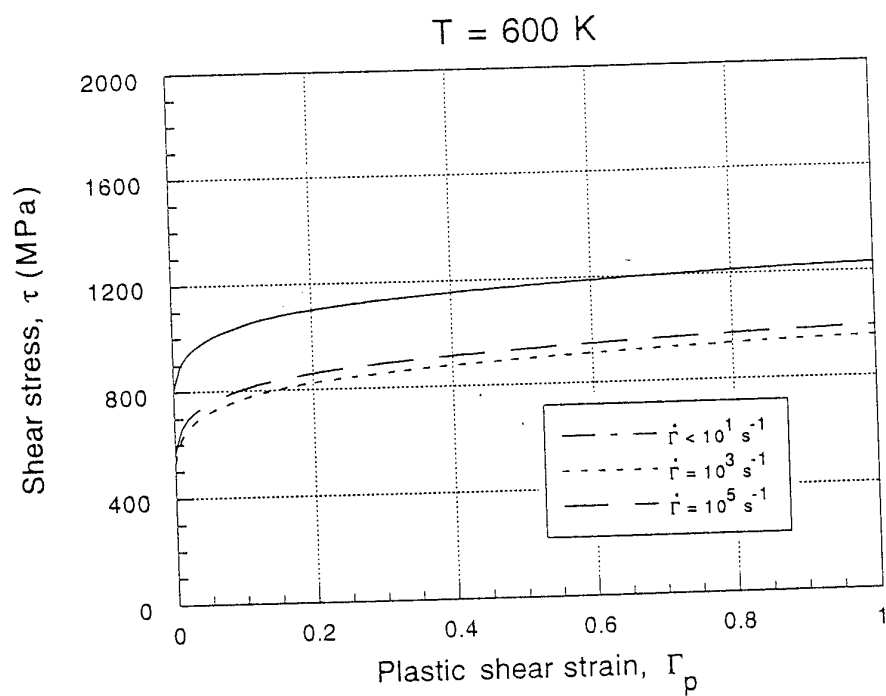


Fig. 28

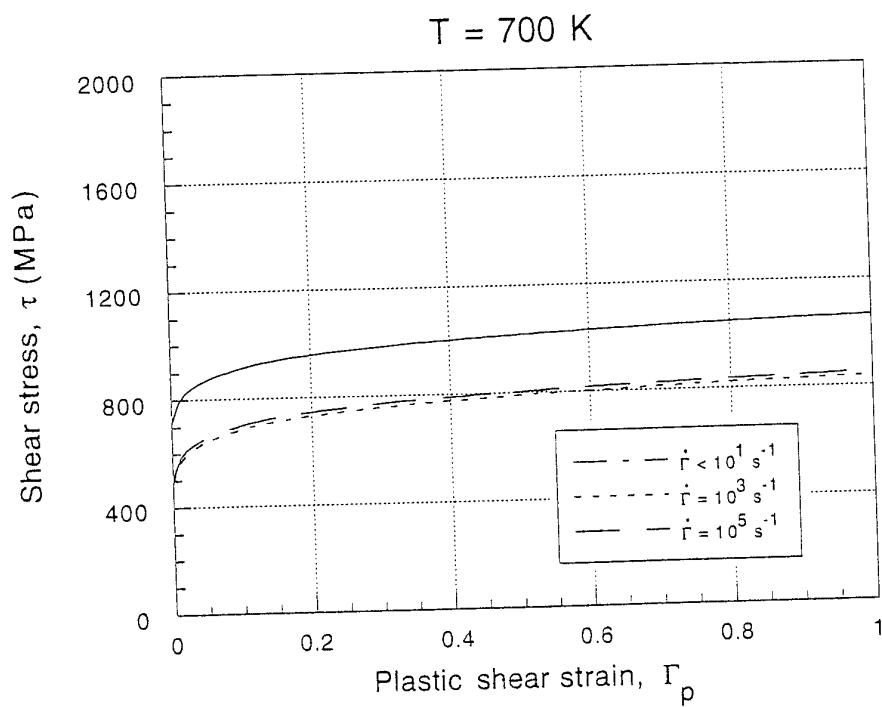


Fig. 29

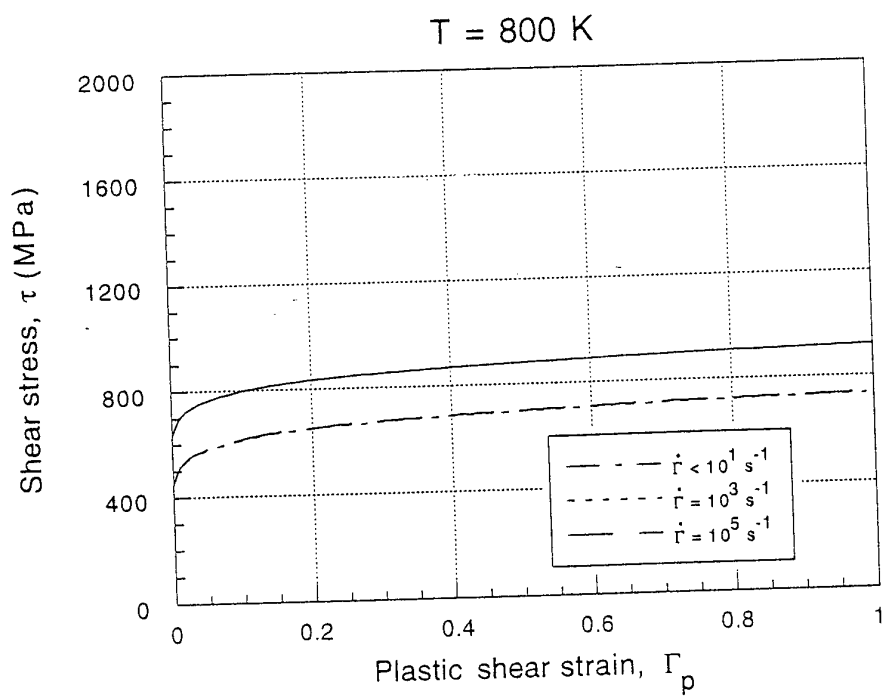


Fig. 30

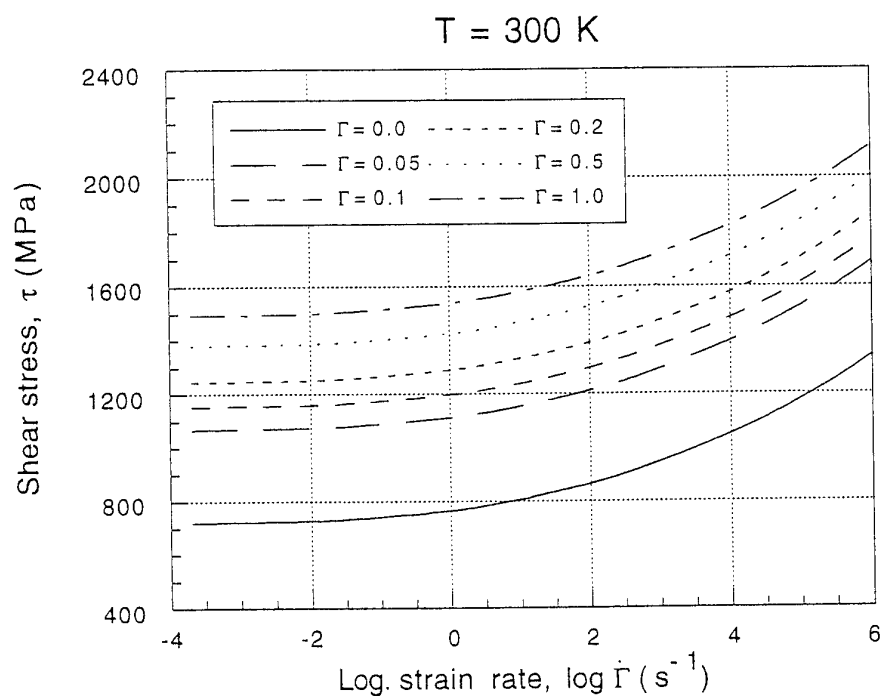


Fig. 31

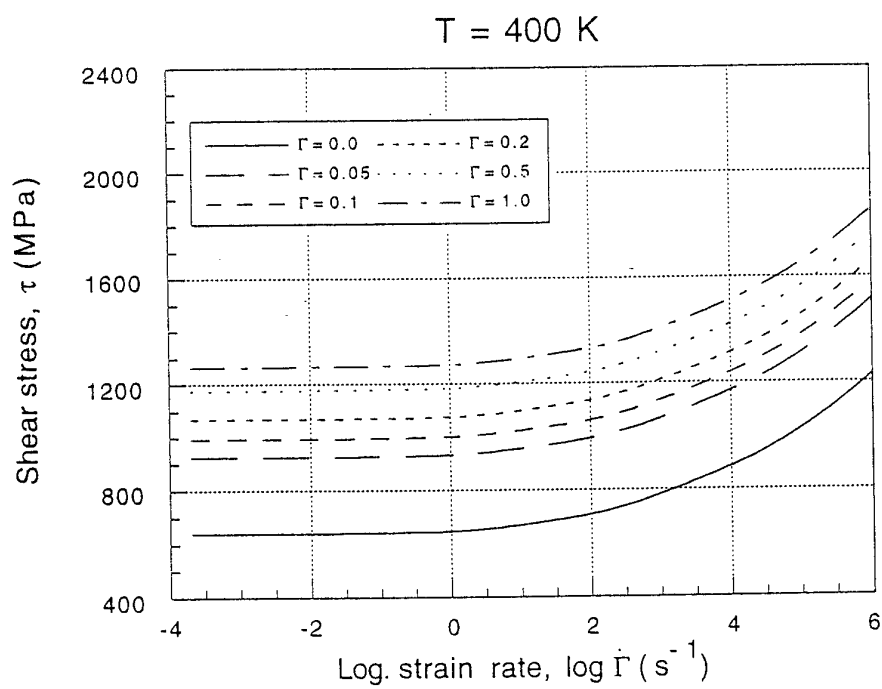


Fig. 32

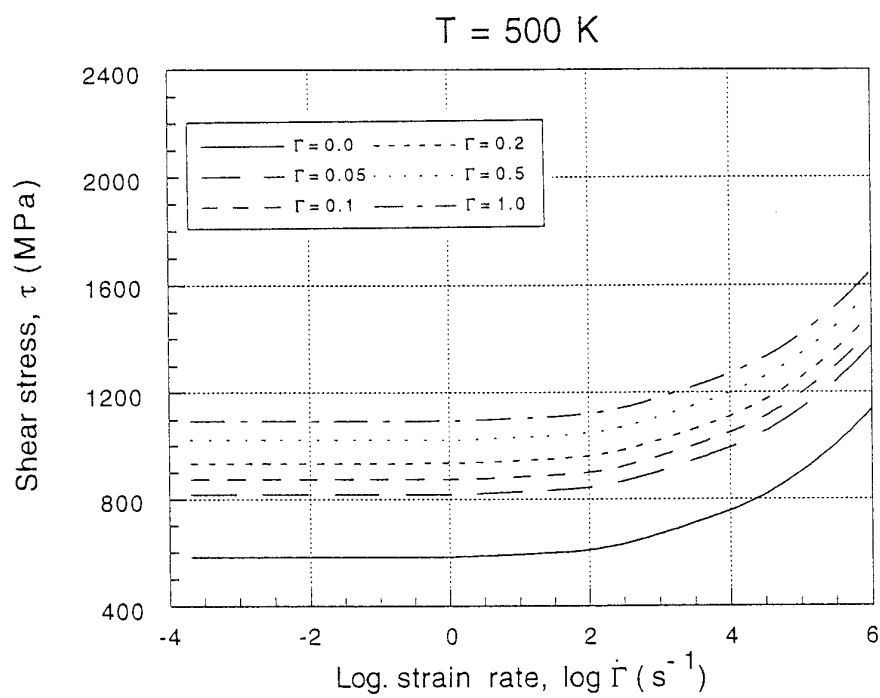


Fig. 33

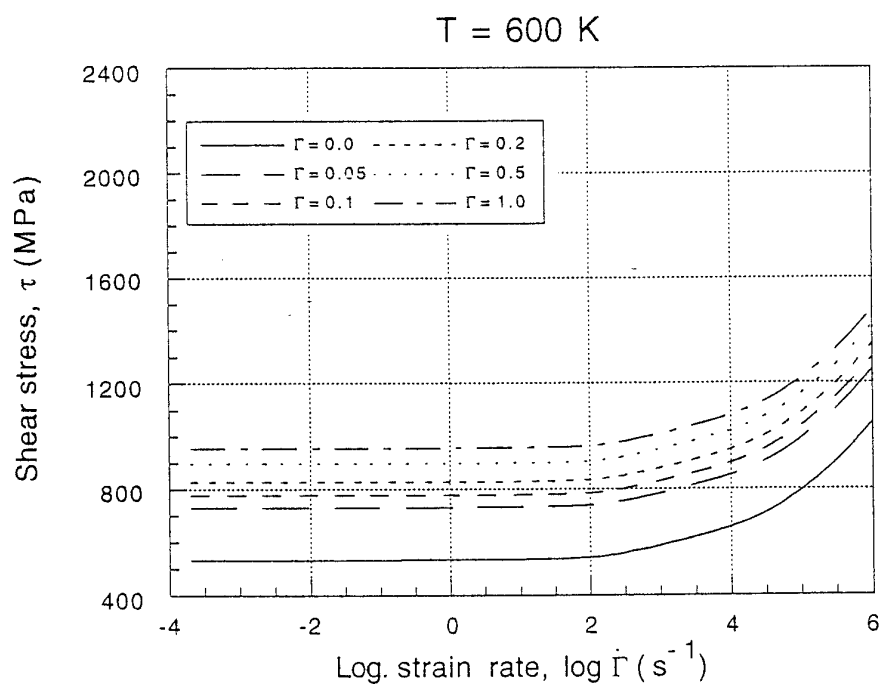


Fig. 34

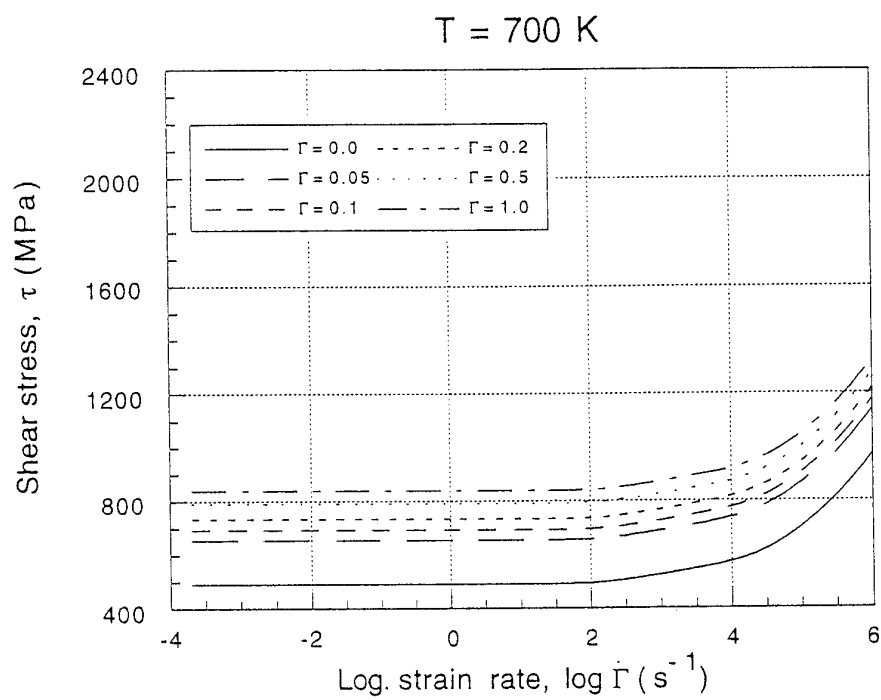


Fig. 35

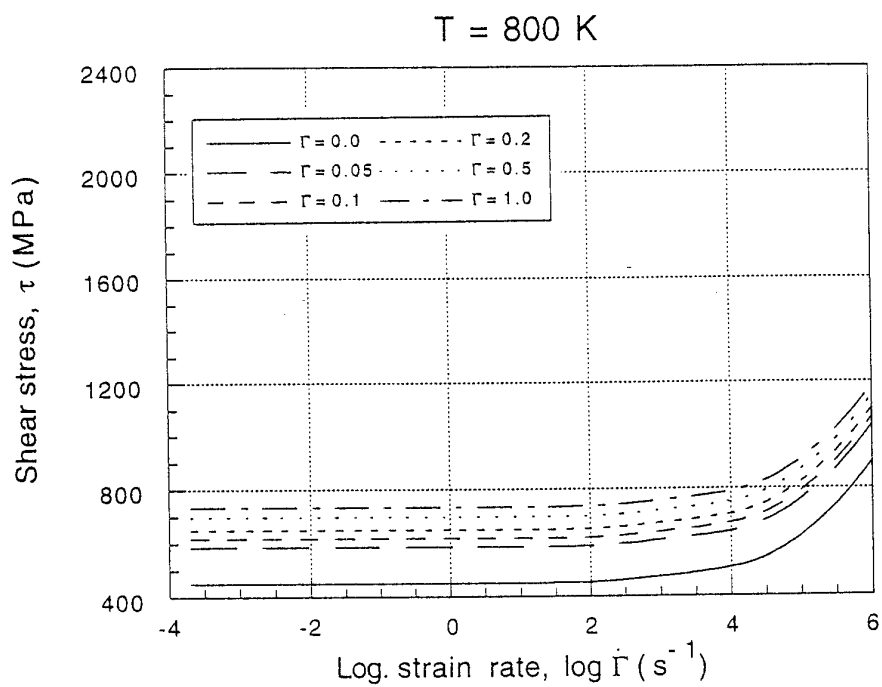


Fig. 36

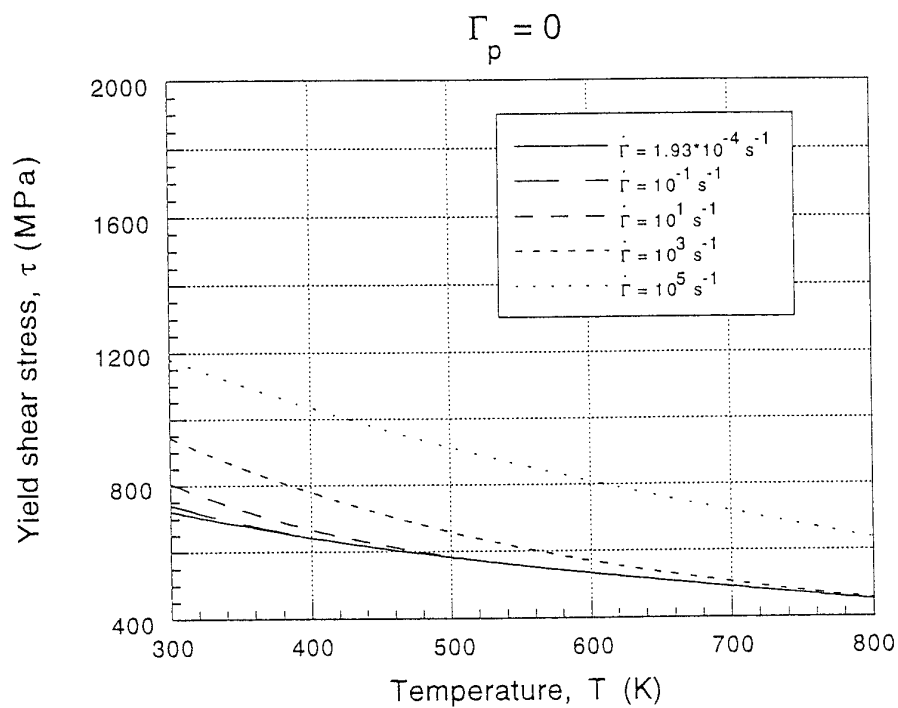


Fig. 37

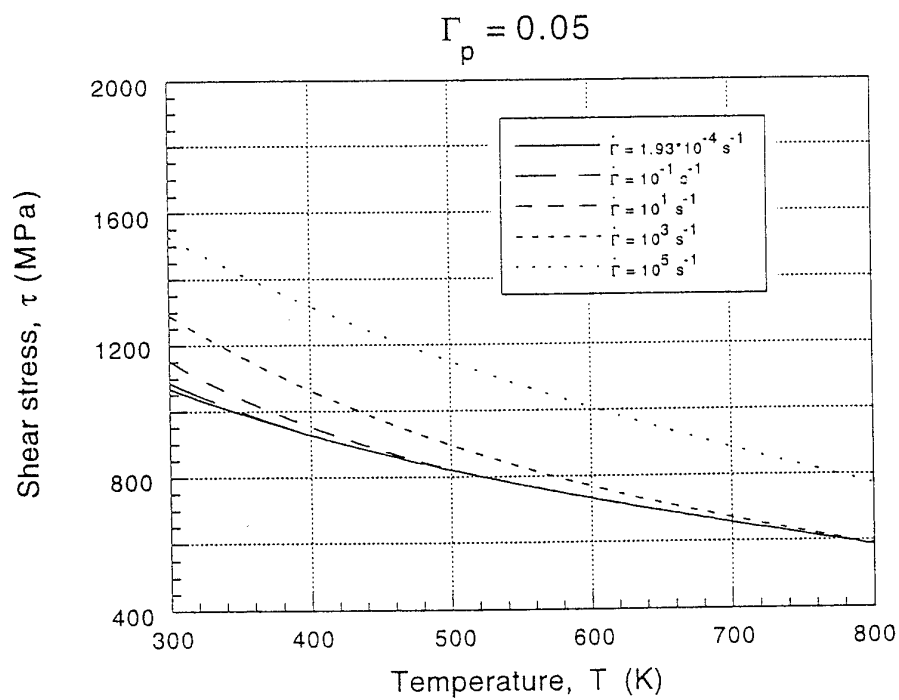


Fig. 38

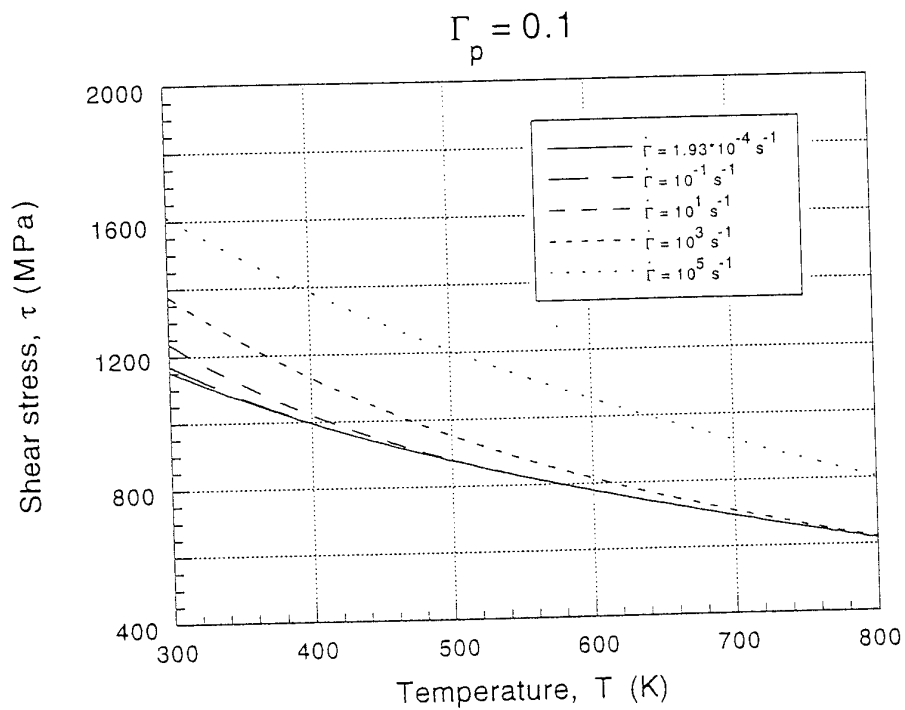


Fig. 39

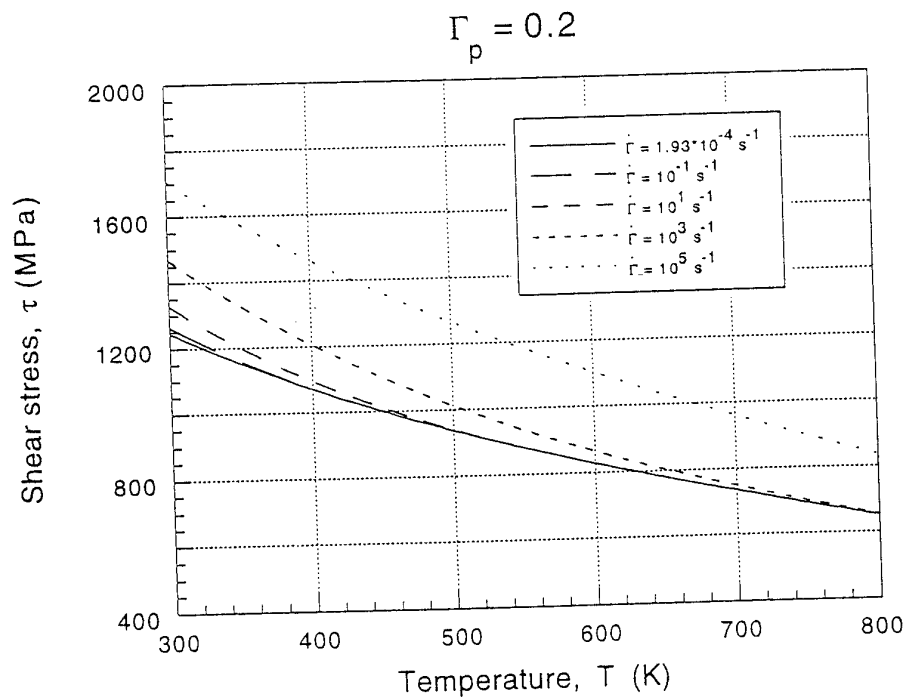


Fig. 40

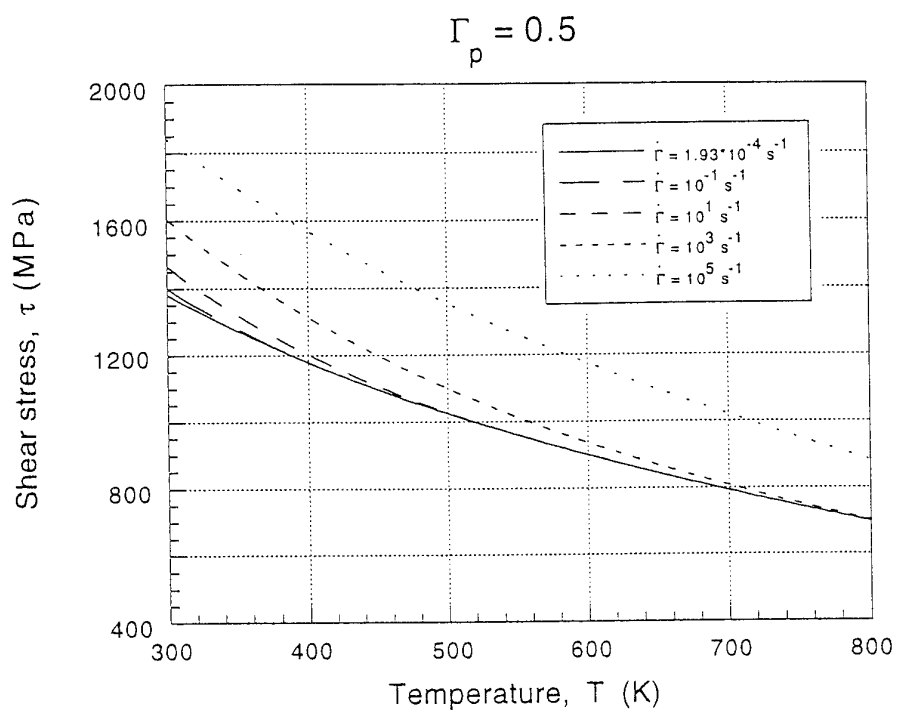


Fig. 41

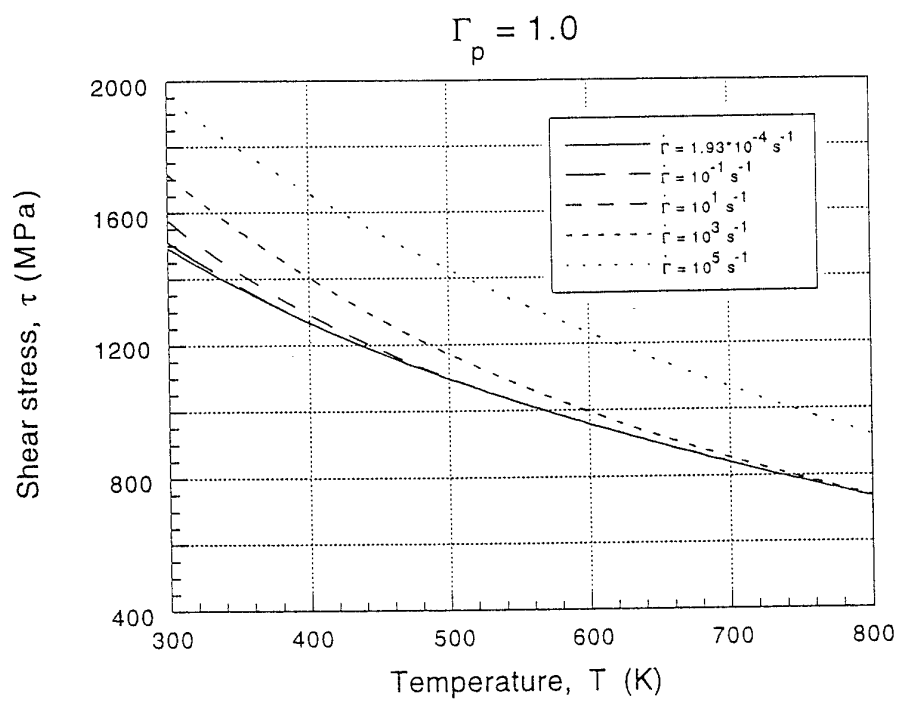


Fig. 42



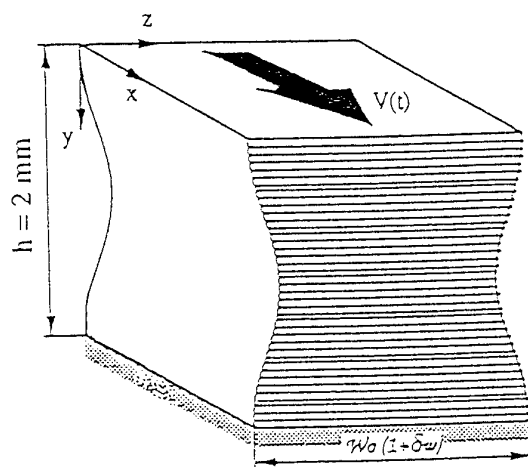
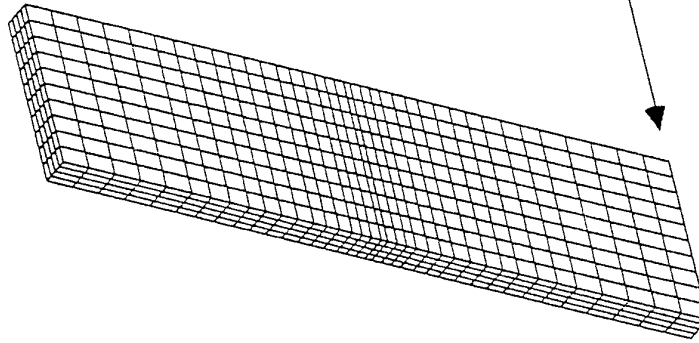


Fig. 43

# ABAQUS

$y = 0.0$  Boundary Conditions:  $V = V_{\text{impact}}$



## PROBLEM SIZE

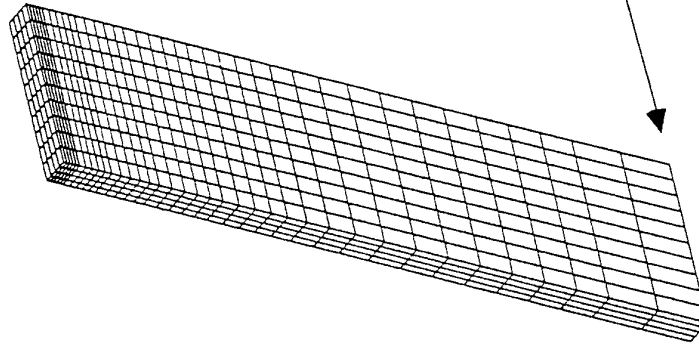
NUMBER OF ELEMENTS IS	296
NUMBER OF NODES IS	1074
NUMBER OF NODES DEFINED BY THE USER	570
NUMBER OF INTERNAL NODES GENERATED BY THE PROGRAM	504
TOTAL NUMBER OF VARIABLES IN THE MODEL	1710
(DEGREES OF FREEDOM PLUS ANY LAGRANGE MULTIPLIER VARIABLES)	69
MAXIMUM D.O.F. WAVEFRONT ESTIMATED AS	63
RMS WAVEFRONT ESTIMATED AS	

TYPE OF ELEMENT: C3D8R (or C3D8T)

Fig. 44

# ABAQUS

$y = 0.0$  Boundary Conditions:  $V = V_{\text{impact}}$



$y = 0.02$  Boundary Conditions:  $\Delta x = 0$



## PROBLEM SIZE

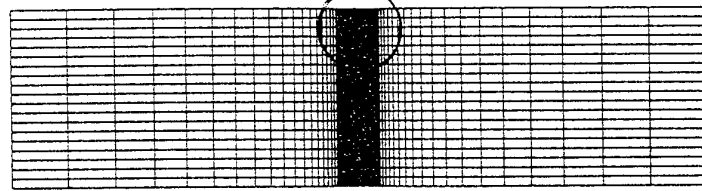
NUMBER OF ELEMENTS IS	296
NUMBER OF NODES IS	1074
NUMBER OF NODES DEFINED BY THE USER	570
NUMBER OF INTERNAL NODES GENERATED BY THE PROGRAM	504
TOTAL NUMBER OF VARIABLES IN THE MODEL	1710
(DEGREES OF FREEDOM PLUS ANY LAGRANGE MULTIPLIER VARIABLES)	69
MAXIMUM D.O.F. WAVEFRONT ESTIMATED AS	63
RMS WAVEFRONT ESTIMATED AS	

TYPE OF ELEMENT: C3D8R (or C3D8T)

Fig. 45

# ABAQUS

$y = 0.0$  Boundary Conditions:  $V = V_{\text{impact}}$



$y = 0.02$  Boundary Conditions:  $\Delta x = 0$

## PROBLEM SIZE

NUMBER OF ELEMENTS IS 1140  
 NUMBER OF NODES IS 2341  
 NUMBER OF NODES DEFINED BY THE USER 1220  
 NUMBER OF INTERNAL NODES GENERATED BY THE PROGRAM 1121  
 TOTAL NUMBER OF VARIABLES IN THE MODEL 2440  
 (DEGREES OF FREEDOM PLUS ANY LAGRANGE MULTIPLIER VARIABLES)  
 MAXIMUM D.O.F. WAVEFRONT ESTIMATED AS 46  
 RMS WAVEFRONT ESTIMATED AS 46

TYPE OF ELEMENT: CPE4R (or CPE4T)

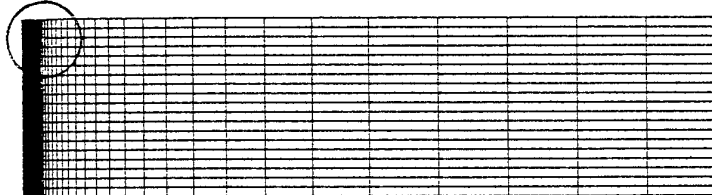
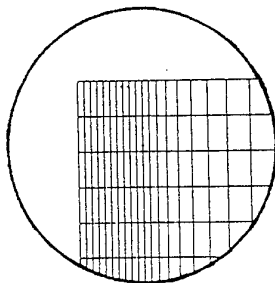
Fig. 46

# ABAQUS

$y = 0.0$  Boundary Conditions:  $V = V_{\text{impact}}$



$y = 0.02$  Boundary Conditions:  $\Delta x = 0$



## PROBLEM SIZE

NUMBER OF ELEMENTS IS	665
NUMBER OF NODES IS	1366
NUMBER OF INTERNAL NODES GENERATED BY THE PROGRAM	720
TOTAL NUMBER OF VARIABLES IN THE MODEL	646
(DEGREES OF FREEDOM PLUS ANY LAGRANGE MULTIPLIER VARIABLES)	1440
MAXIMUM D.O.F. WAVEFRONT ESTIMATED AS	46
RMS WAVEFRONT ESTIMATED AS	45

TYPE OF ELEMENT: CPE4R (or CPE4T)

Fig. 47

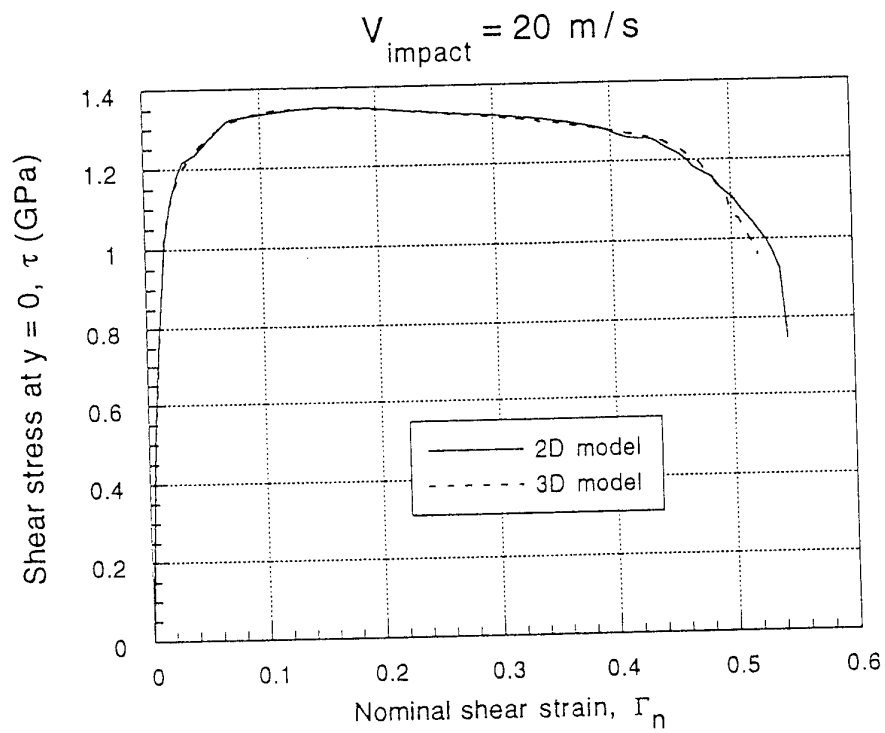


Fig. 48

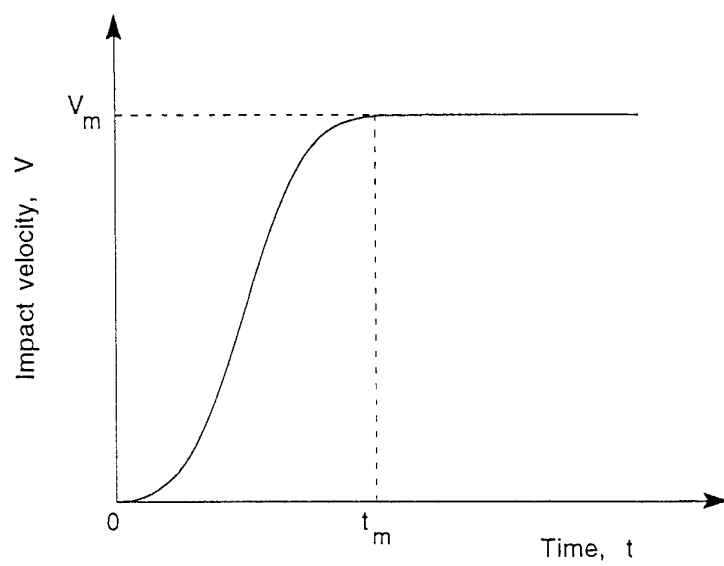


Fig. 49

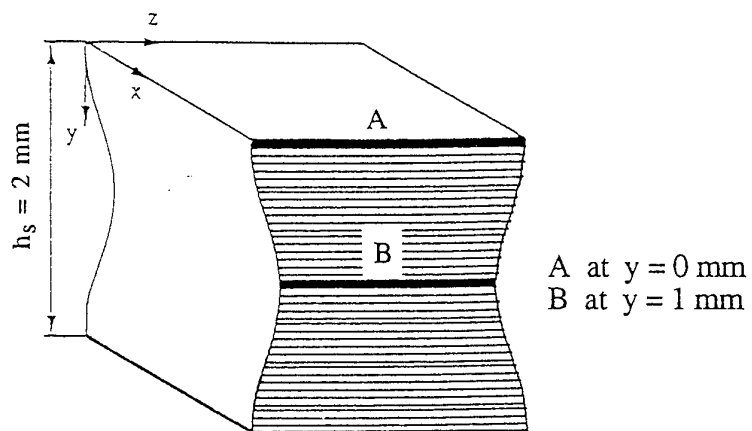


Fig. 50

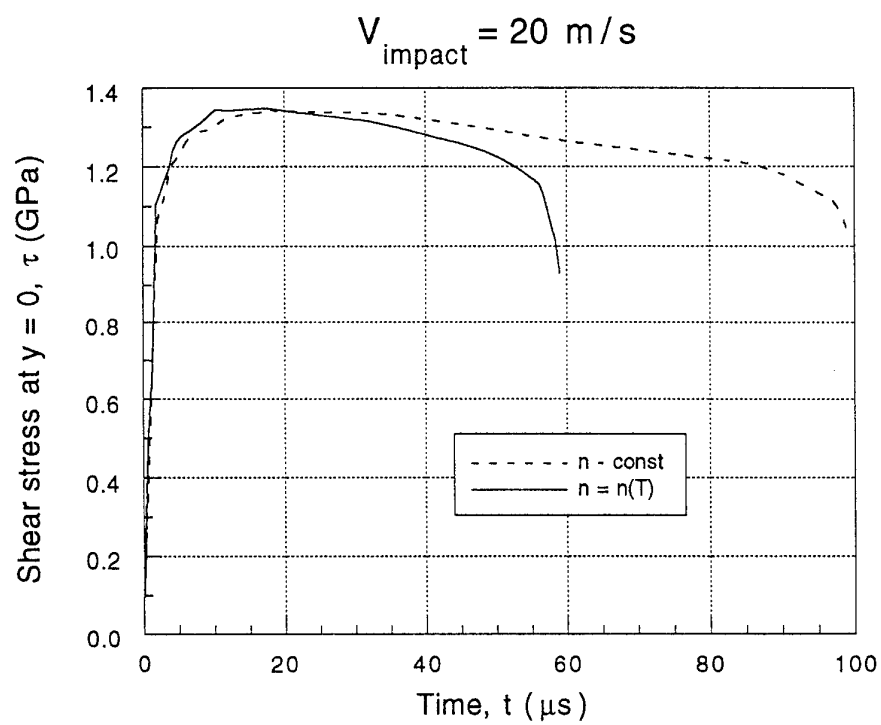


Fig. 51

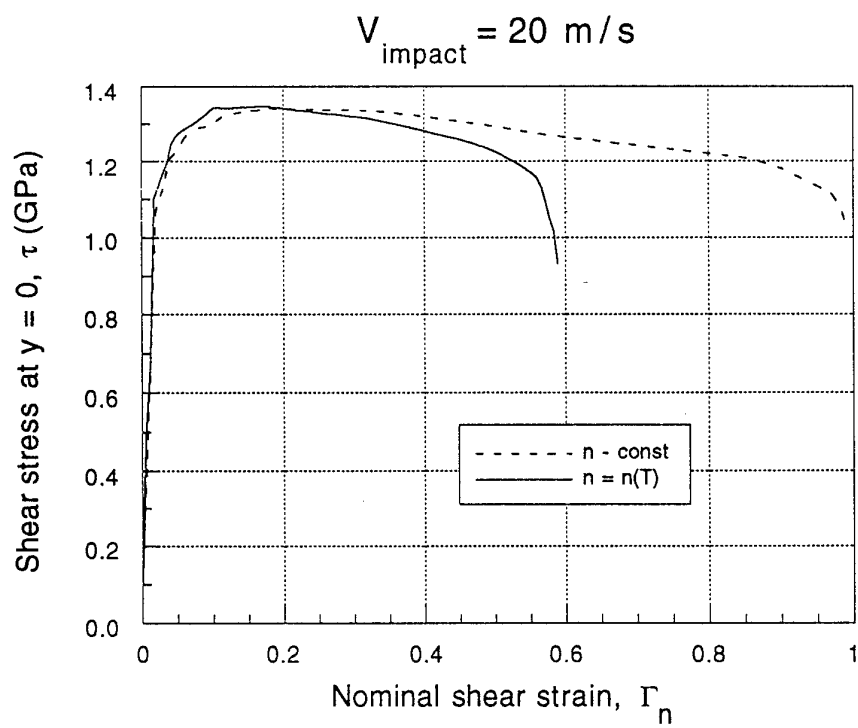
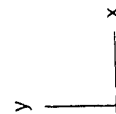
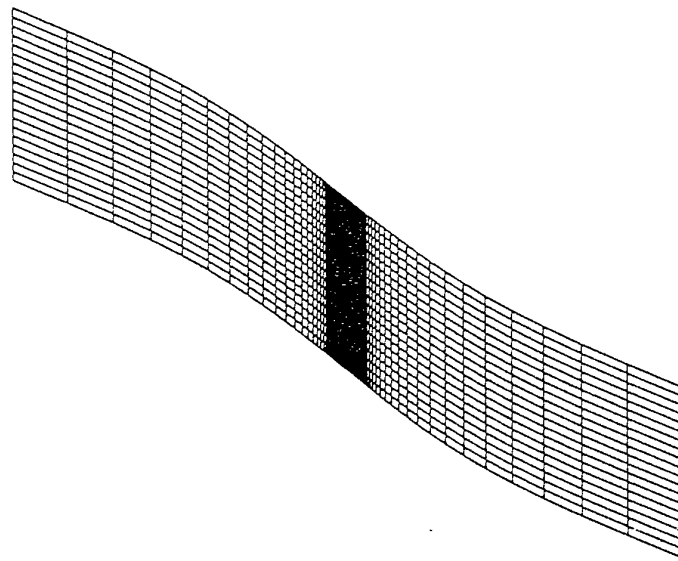


Fig. 52



ABAQUS



$V_{\text{impact}} = 20 \text{ m/s}$

Fig. 53

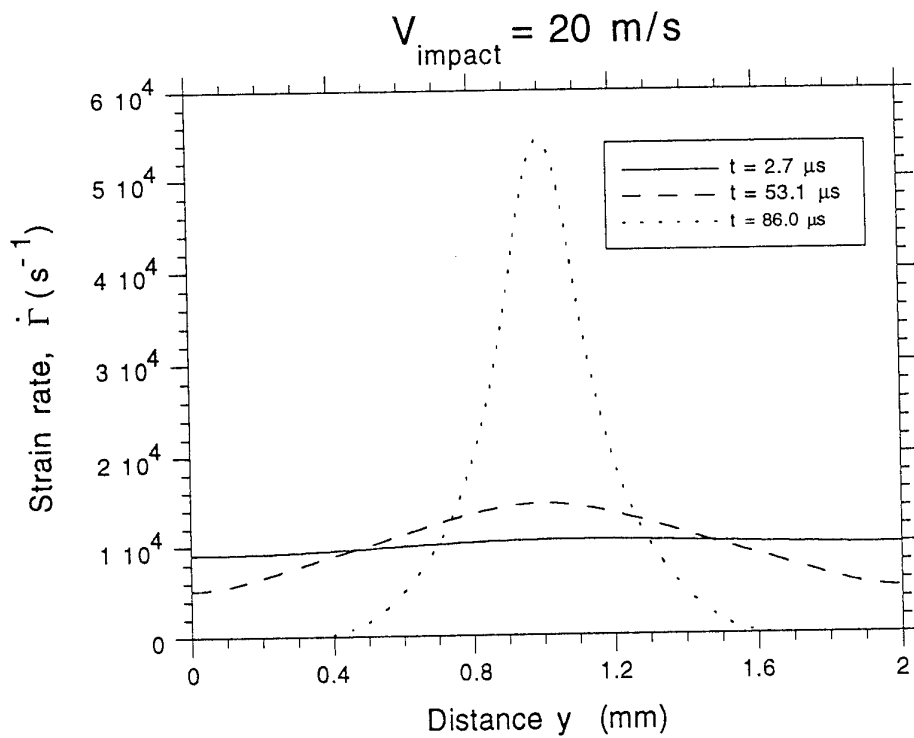


Fig. 54

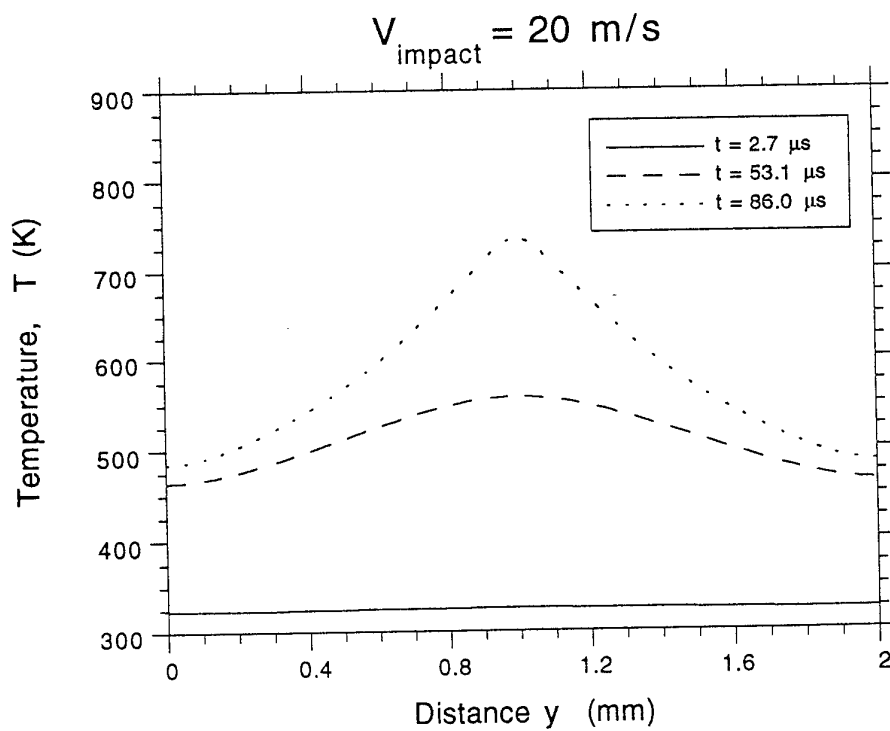


Fig. 55

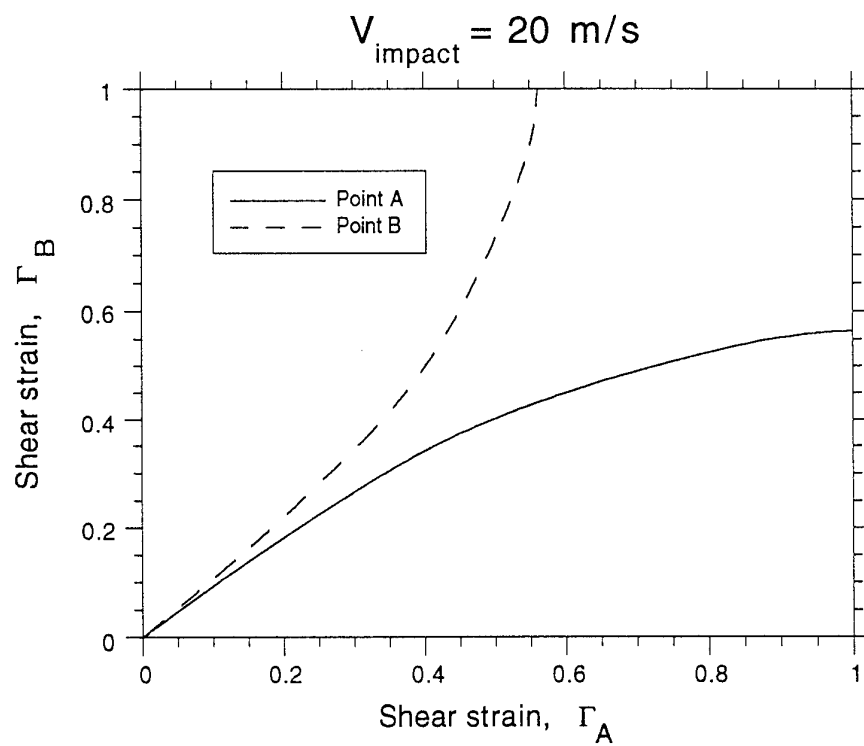


Fig. 56

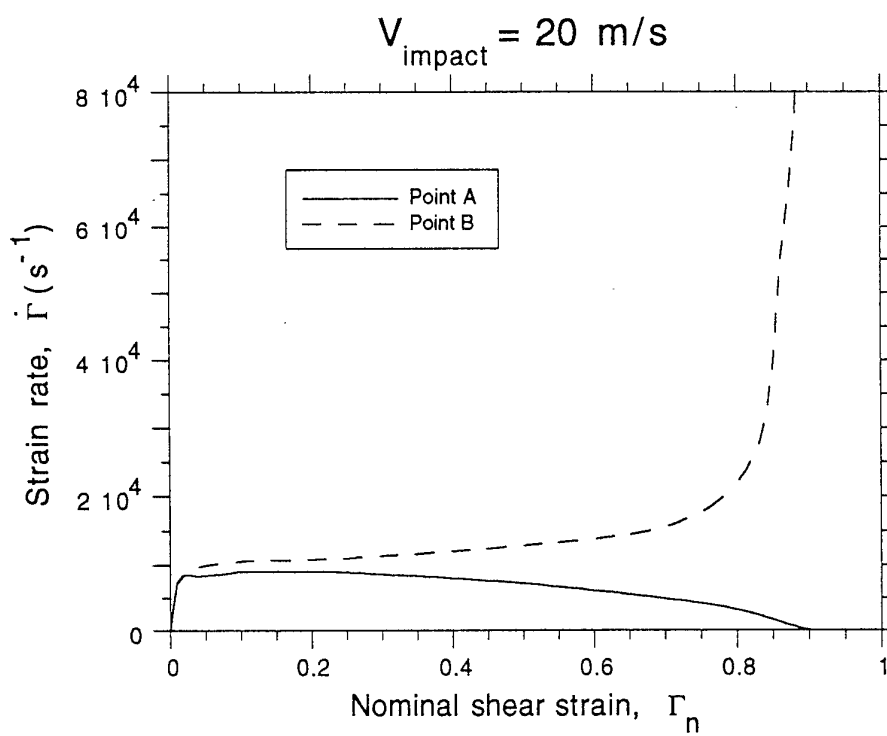


Fig. 57

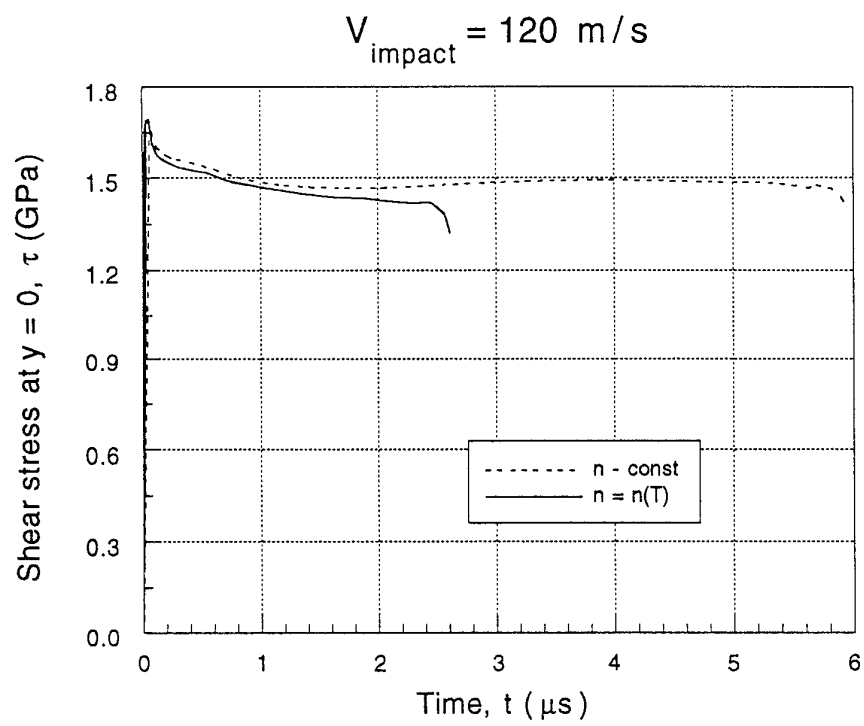


Fig. 58

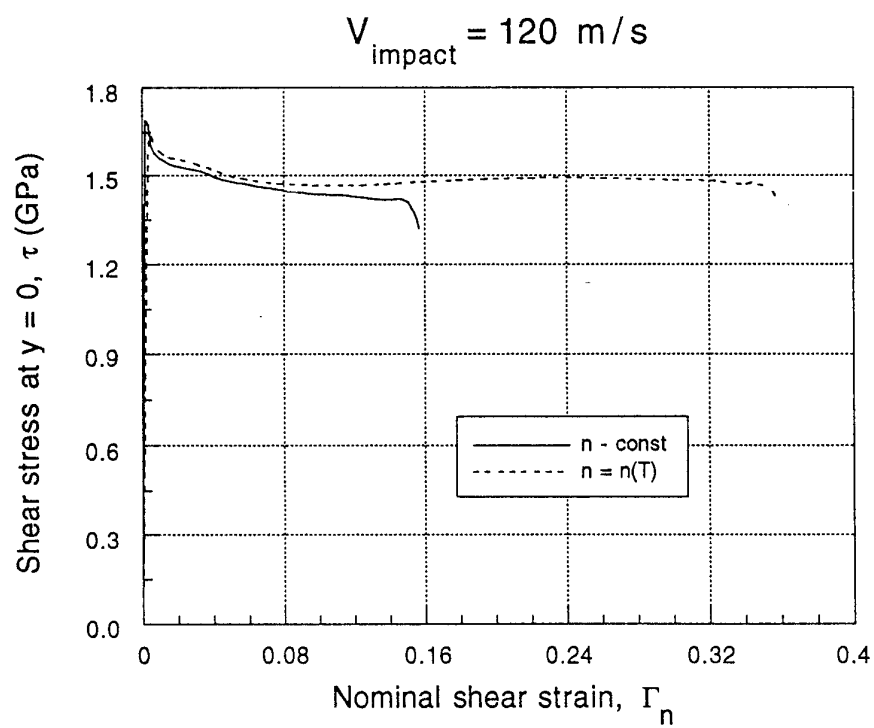
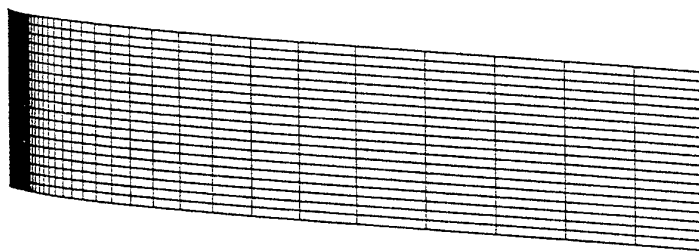
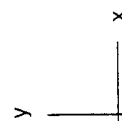


Fig. 59

ABAQUS



$V_{\text{impact}} = 120 \text{ m/s}$

Fig. 60

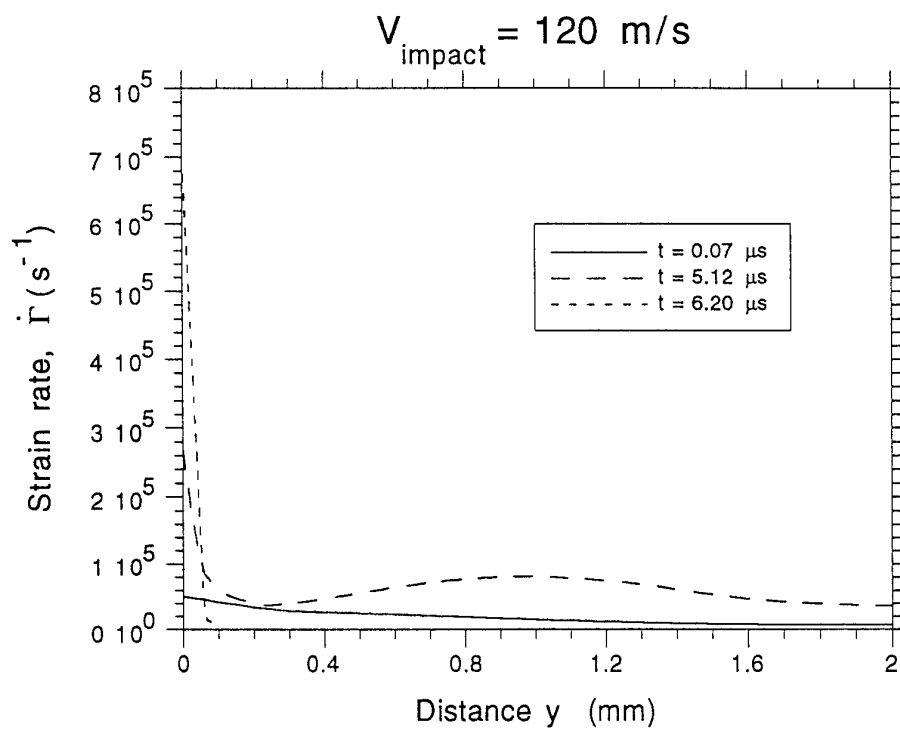


Fig. 61

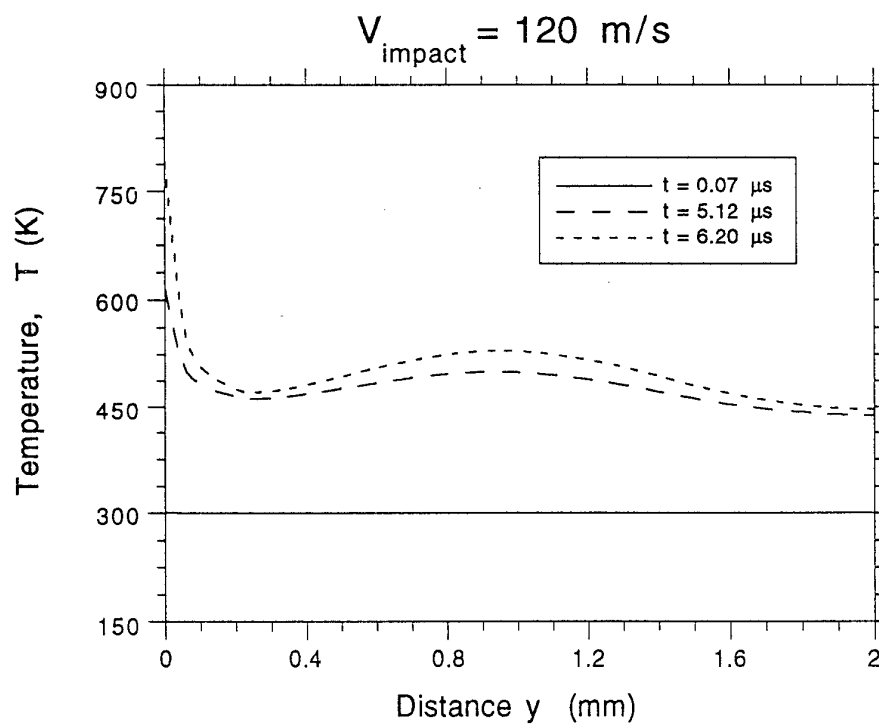


Fig. 62

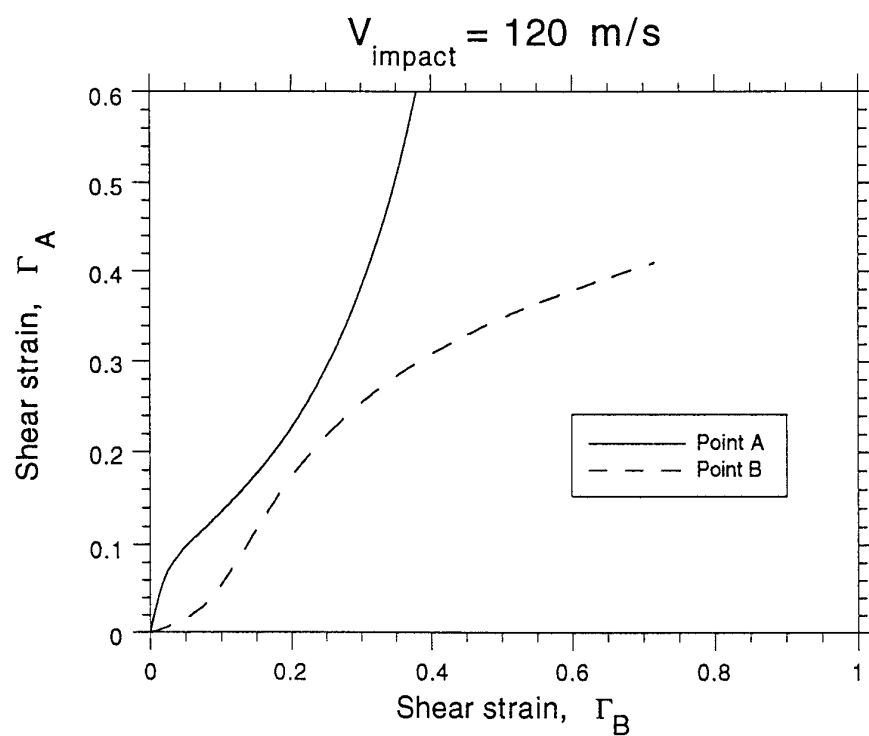


Fig. 63

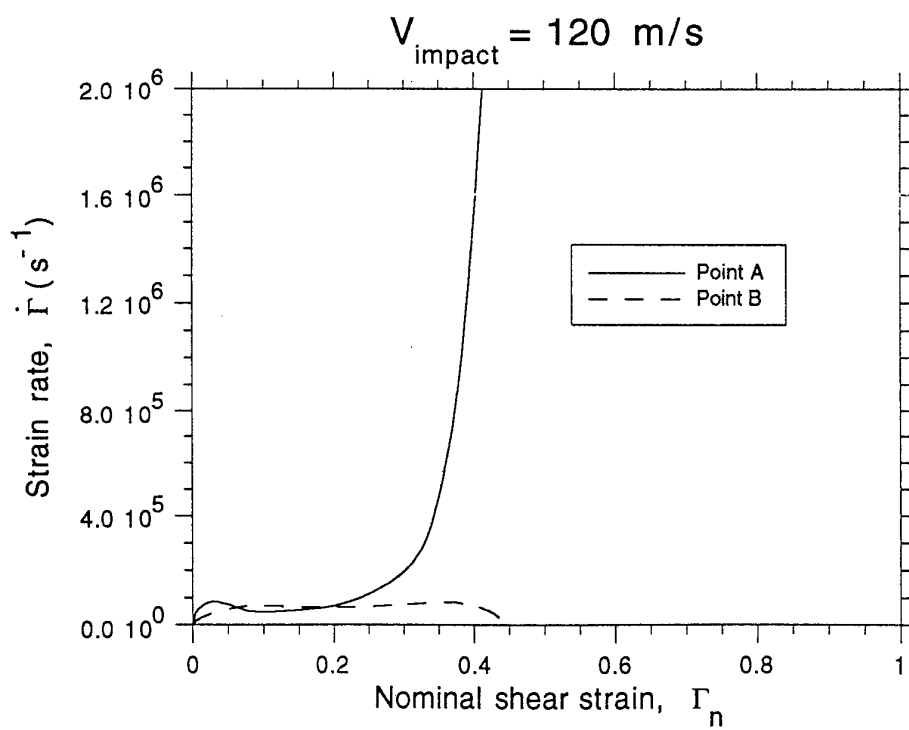


Fig. 64

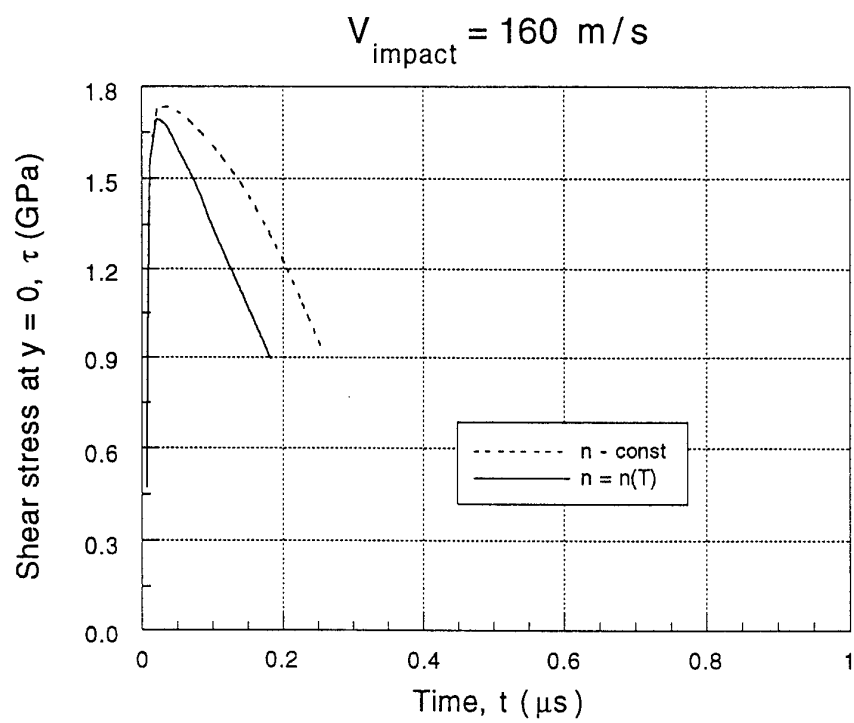


Fig. 65

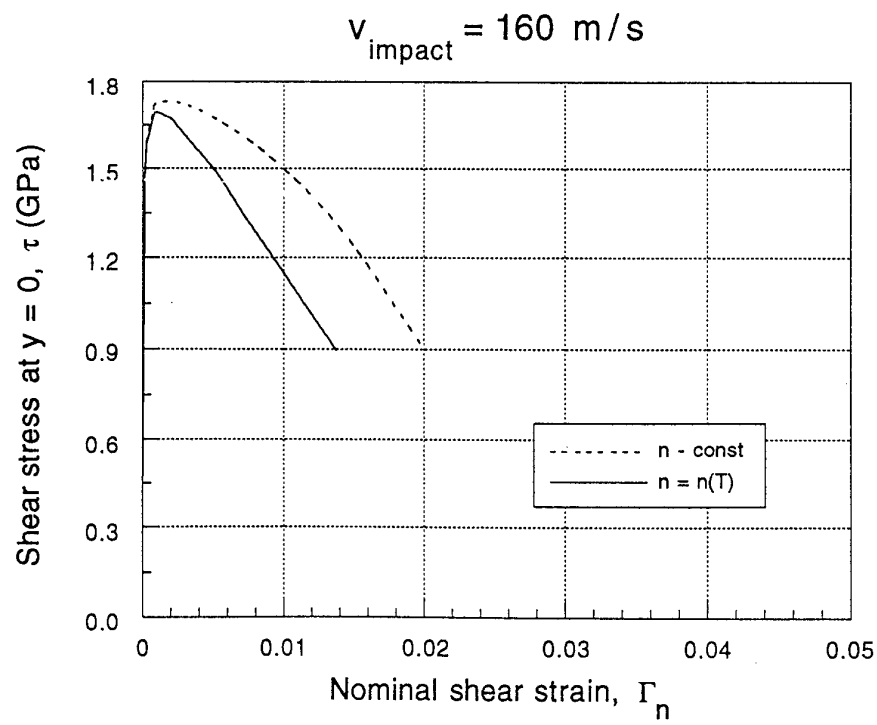
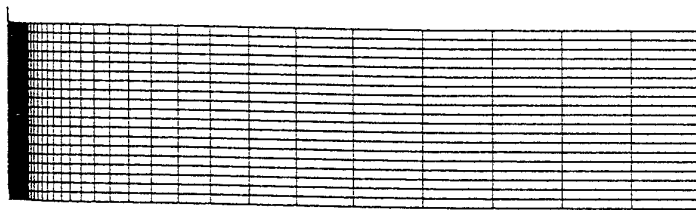
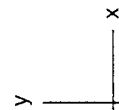


Fig. 66



ABAQUS



$V_{\text{impact}} = 160 \text{ m/s}$

Fig. 67

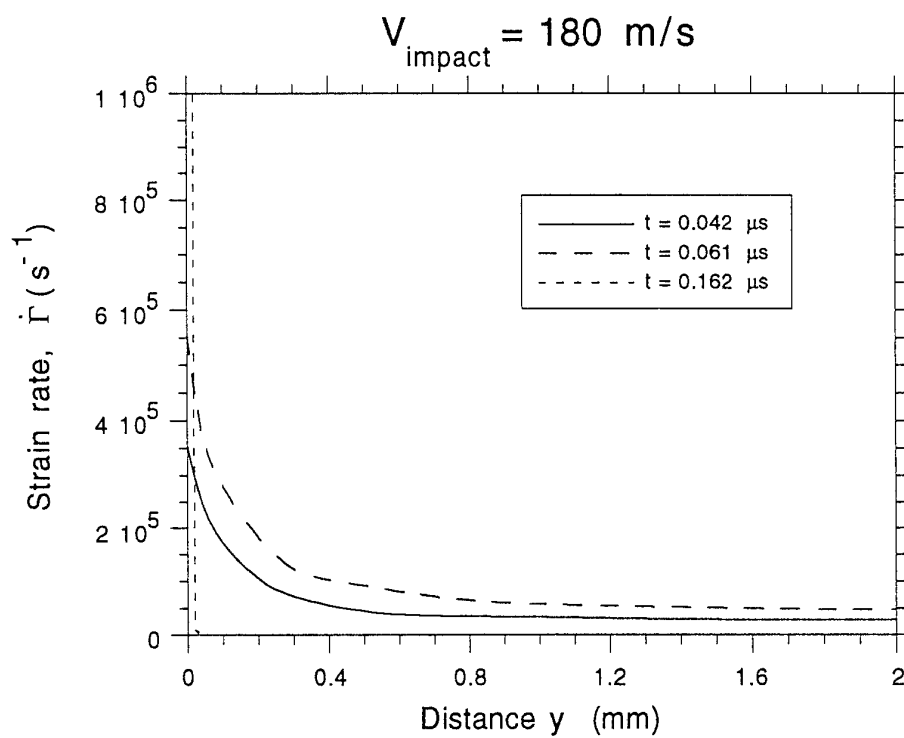


Fig. 68

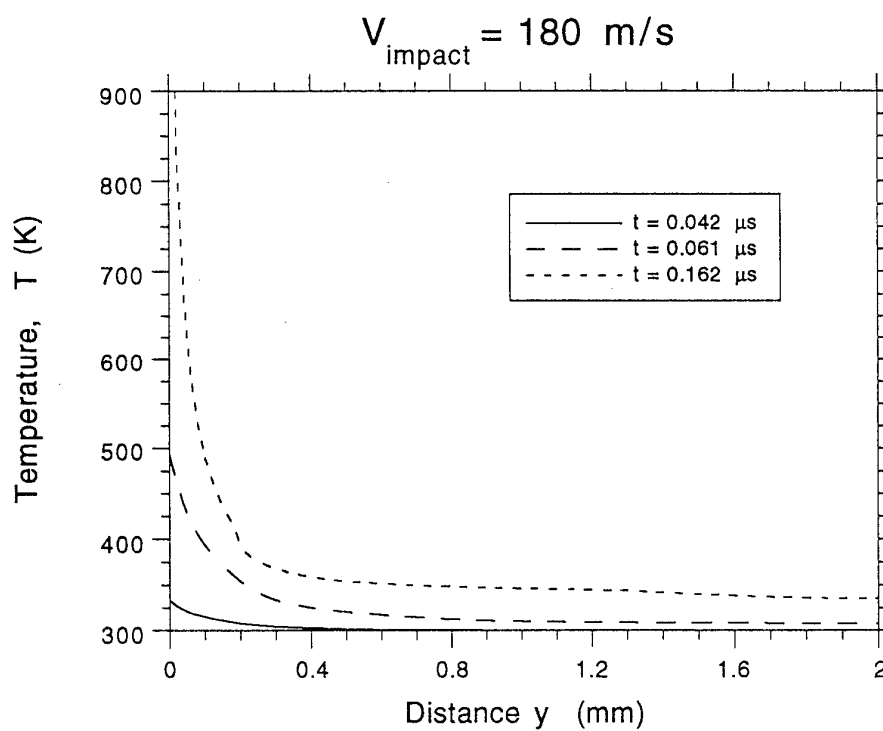


Fig. 69

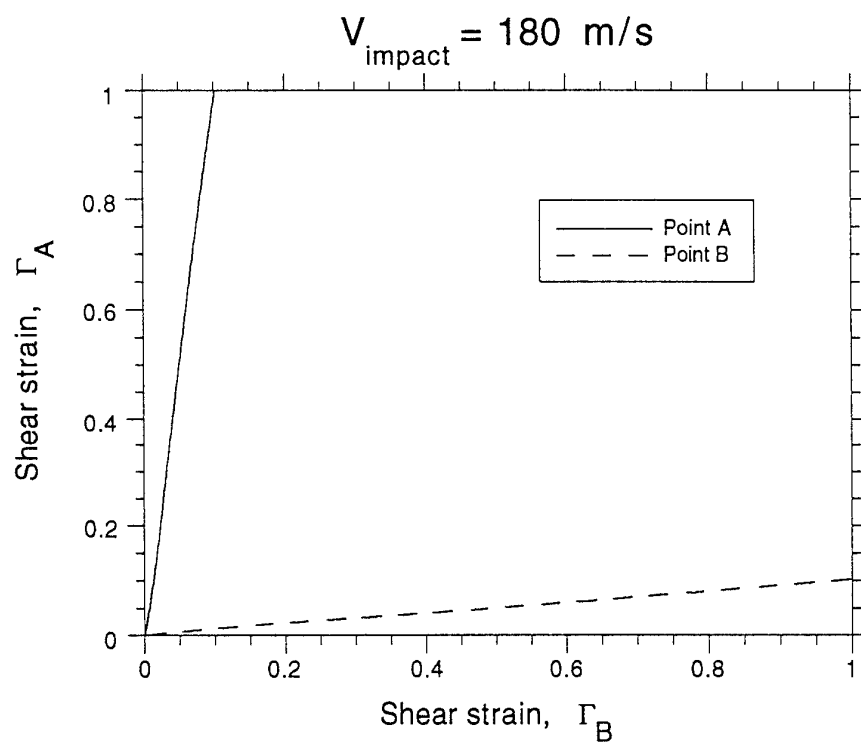


Fig. 70

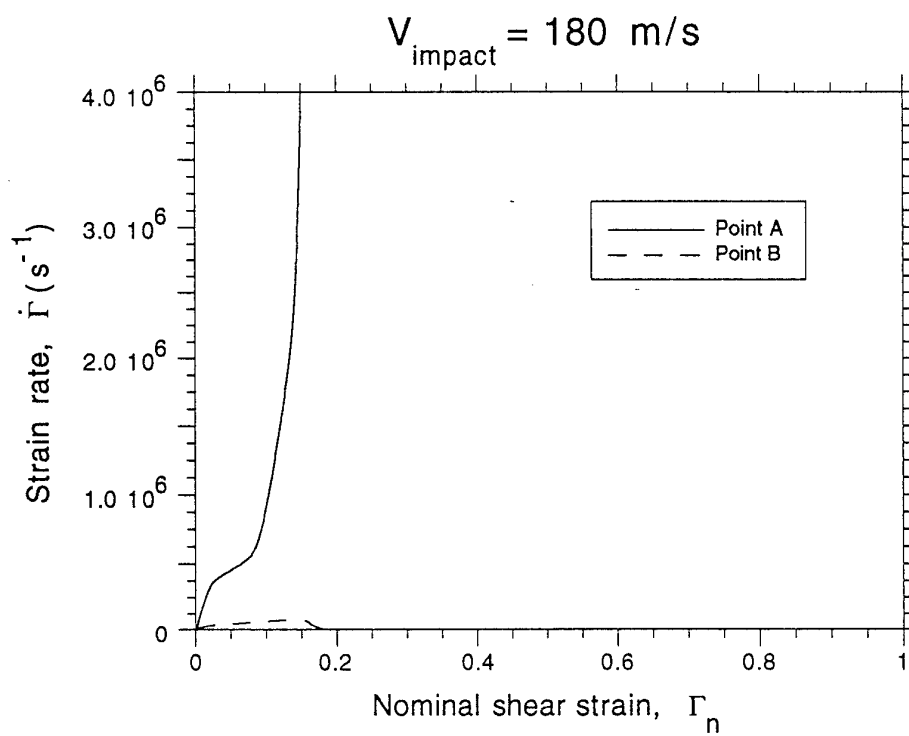


Fig. 71

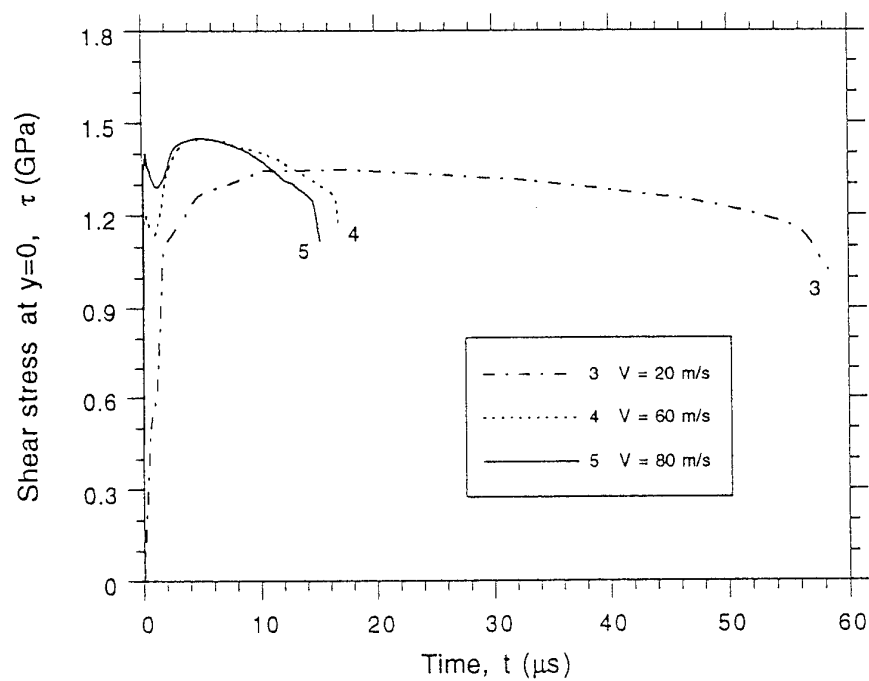


Fig. 72

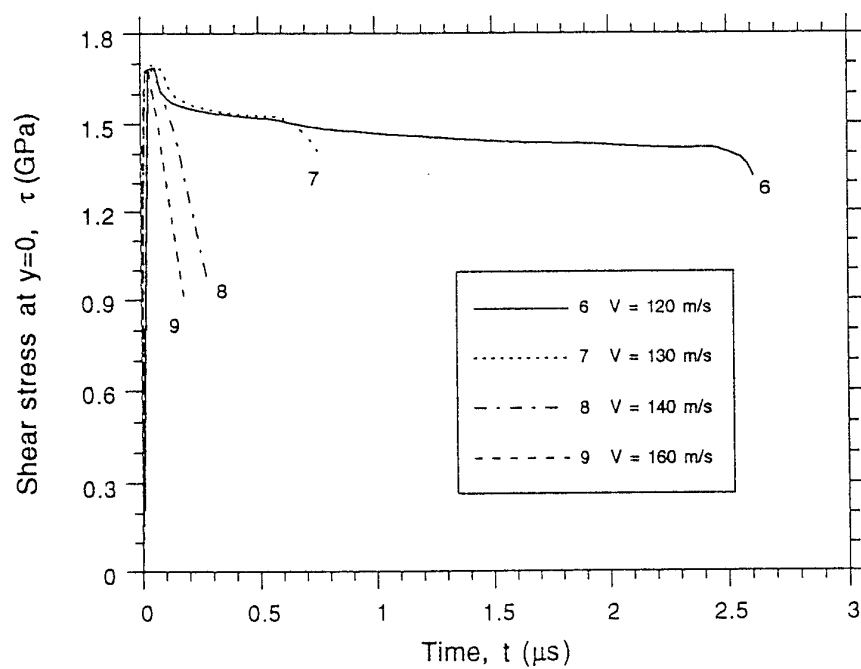


Fig. 73

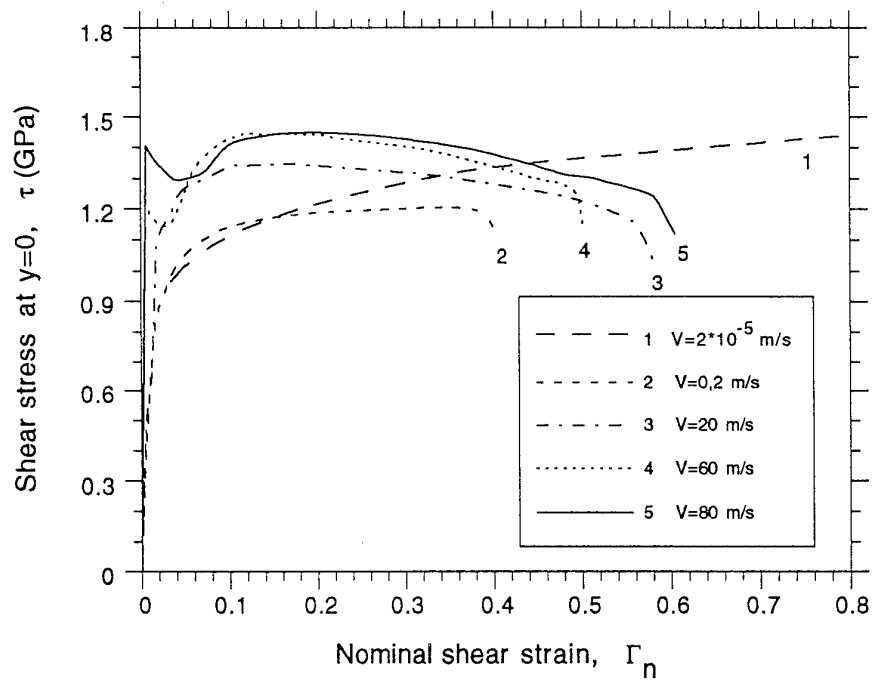


Fig. 74

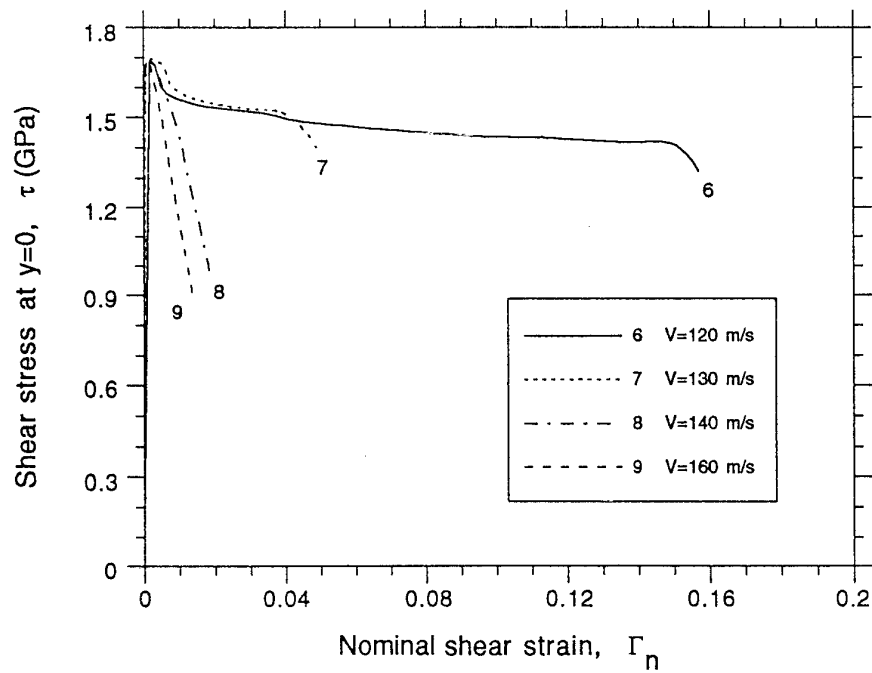


Fig. 75

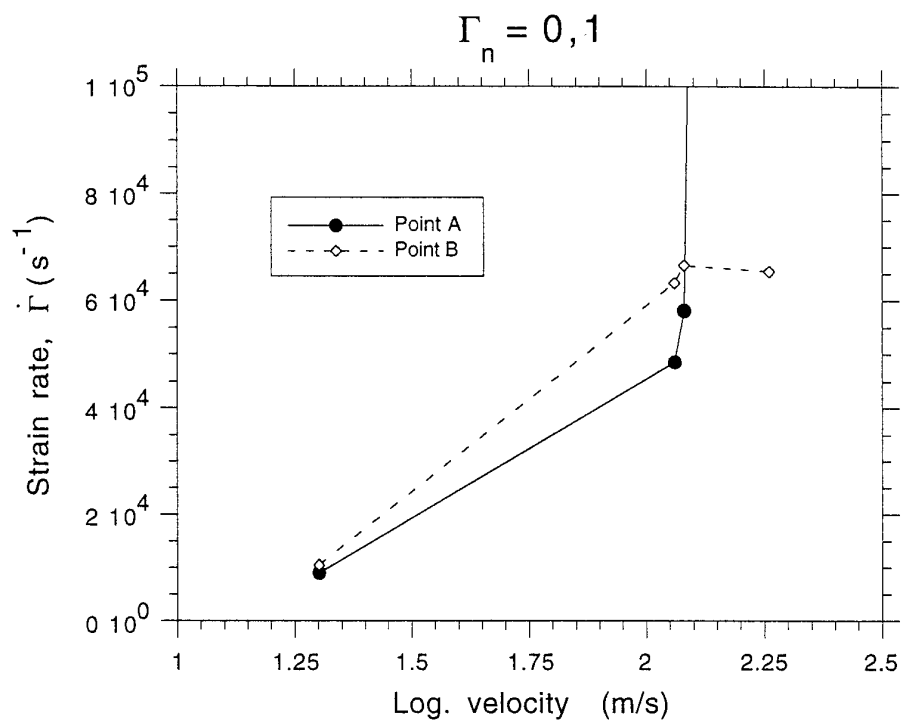


Fig. 76

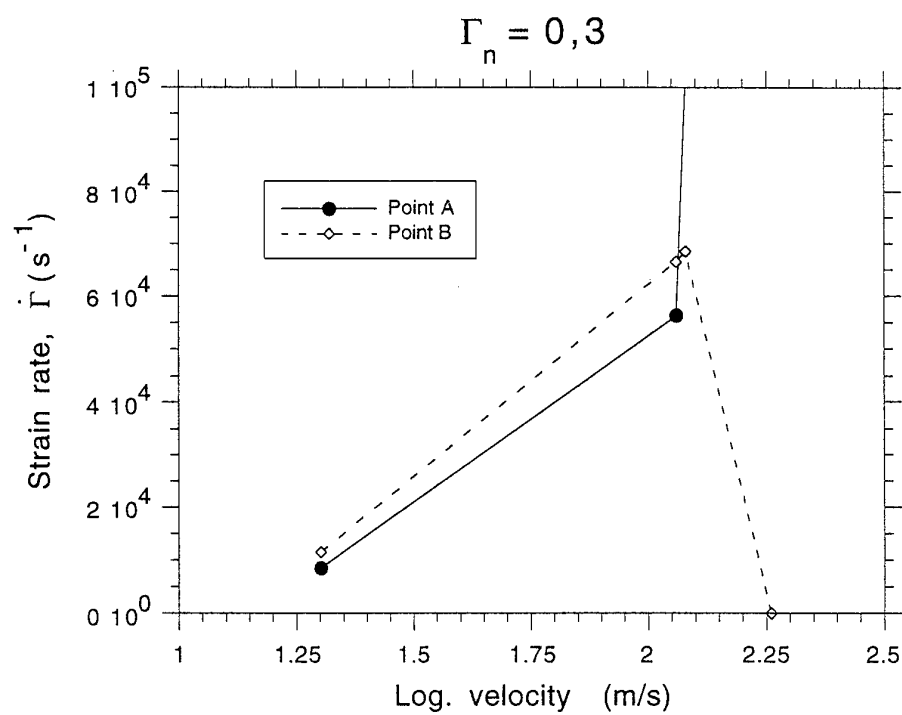


Fig. 77

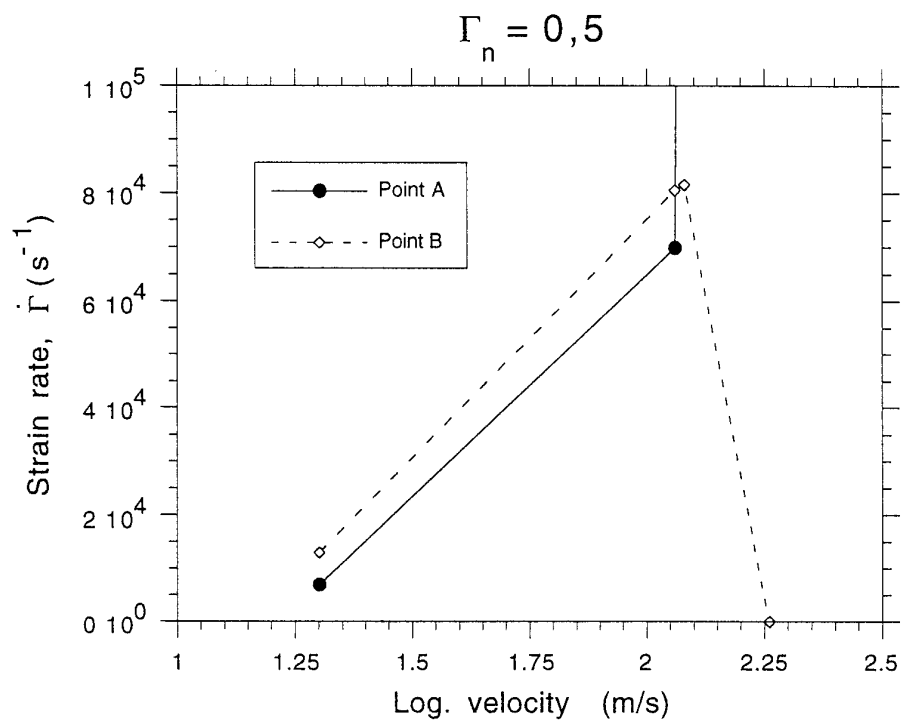


Fig. 78

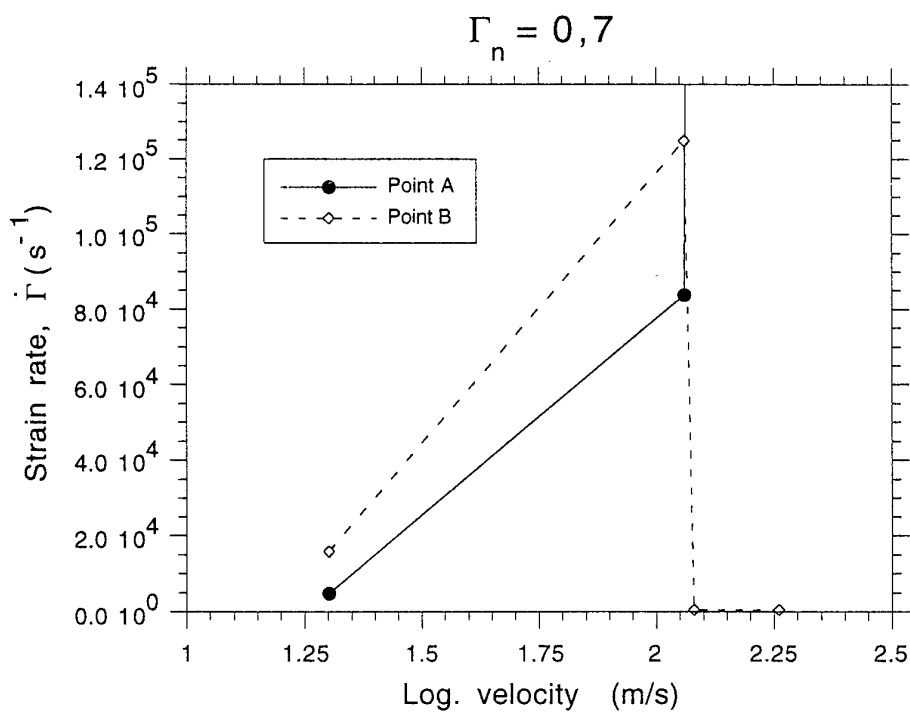


Fig. 79

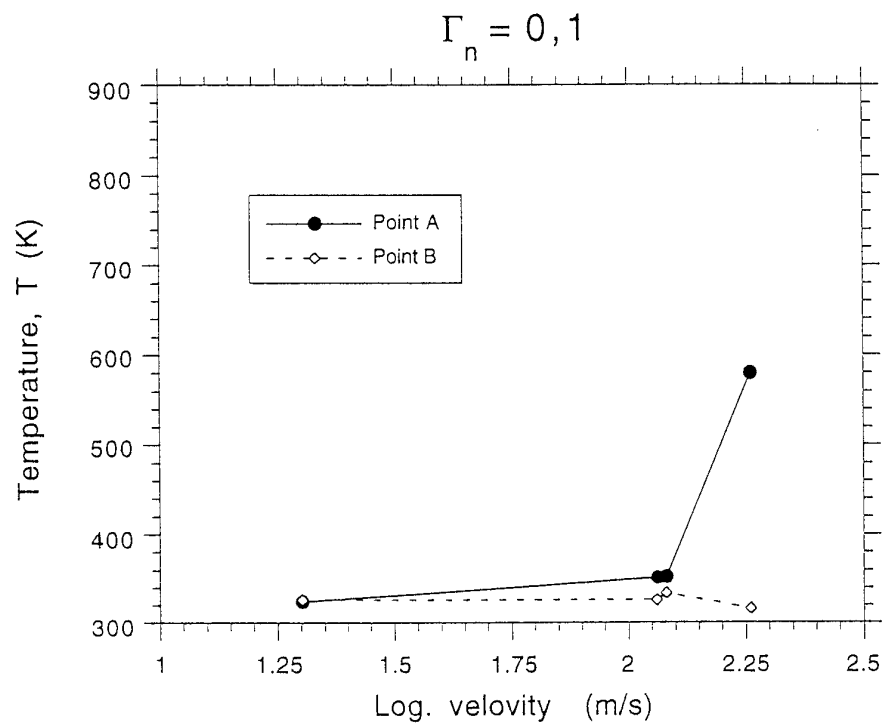


Fig. 80

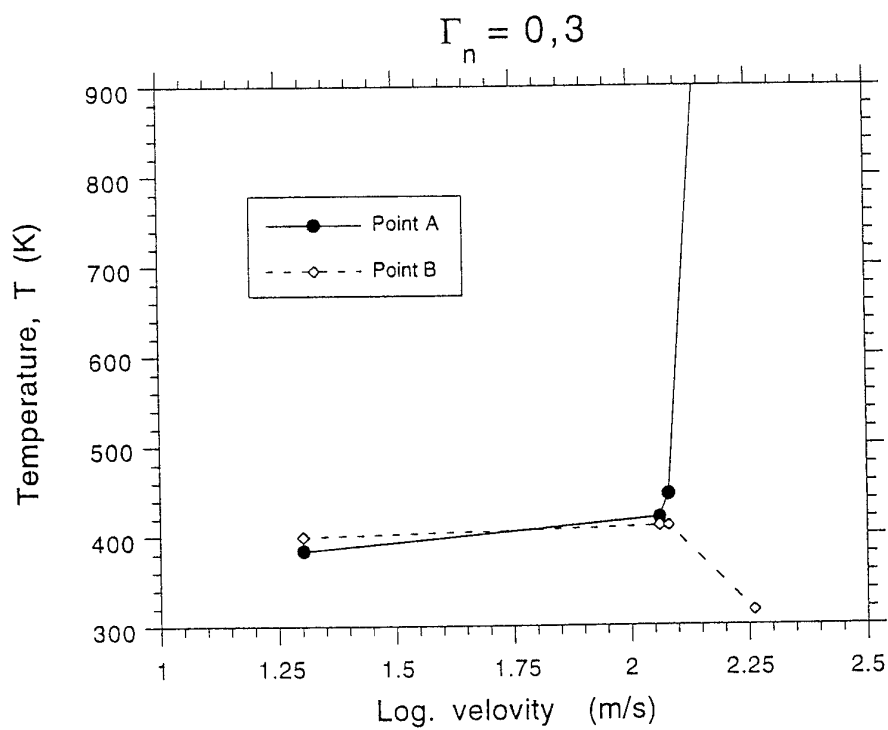


Fig. 81



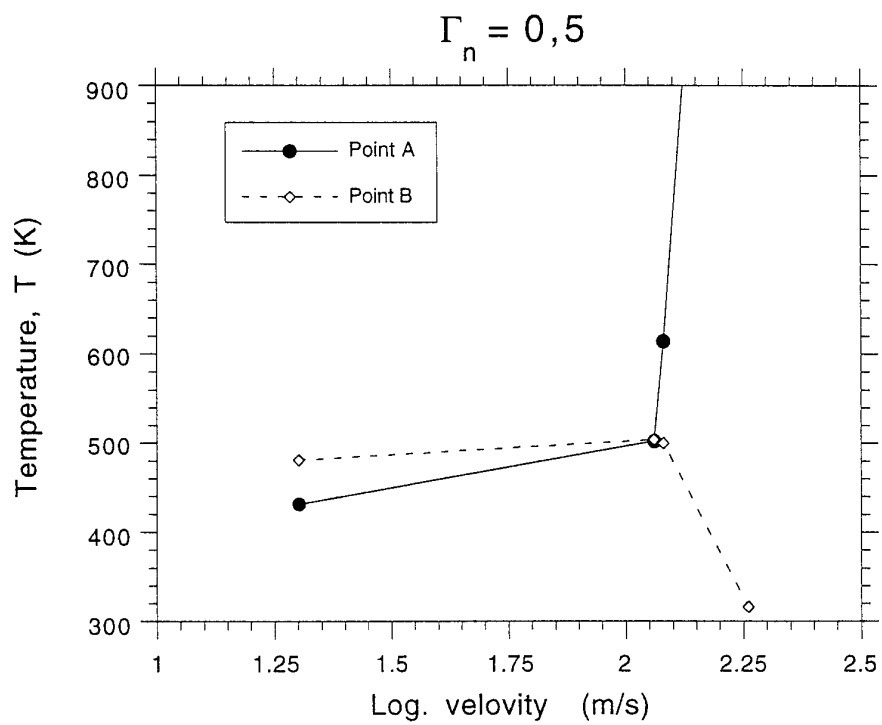


Fig. 82

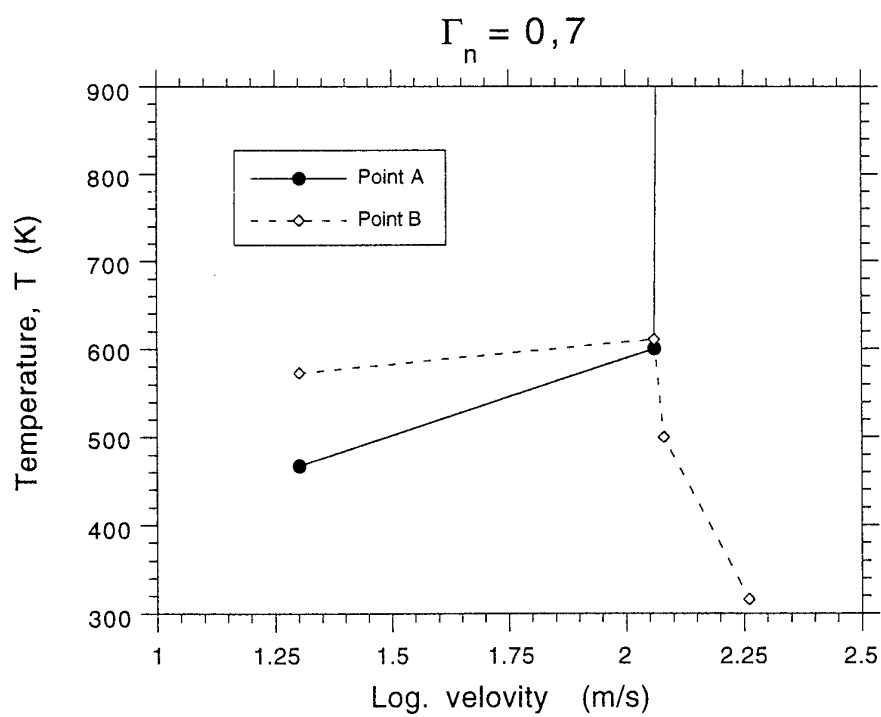


Fig. 83

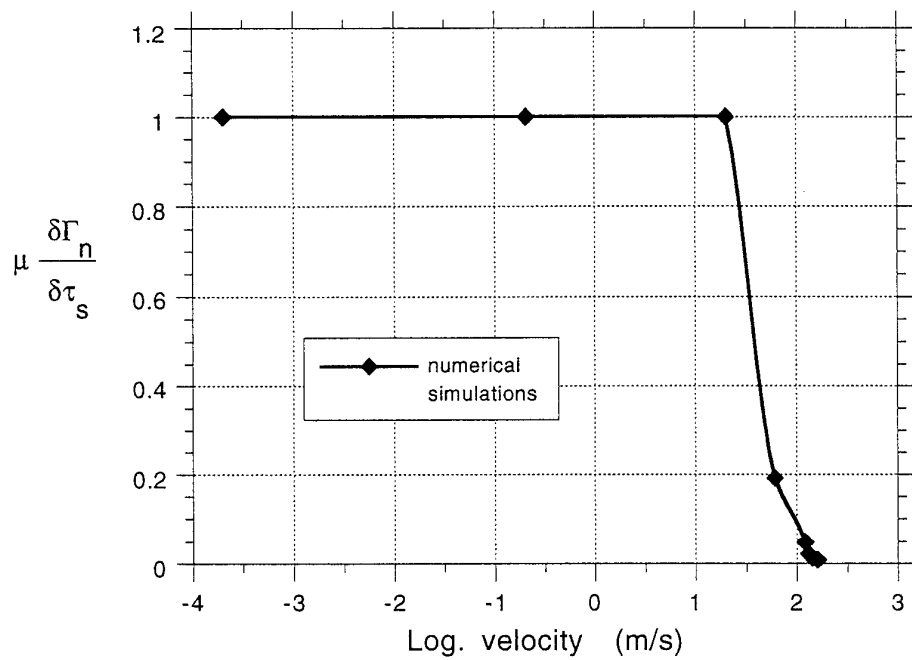


Fig. 84

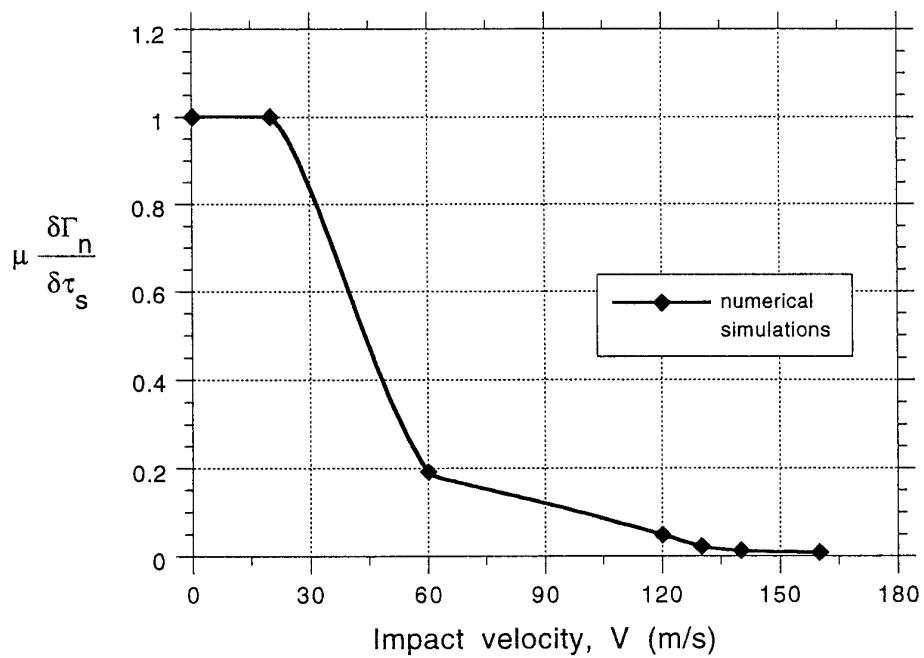


Fig. 85

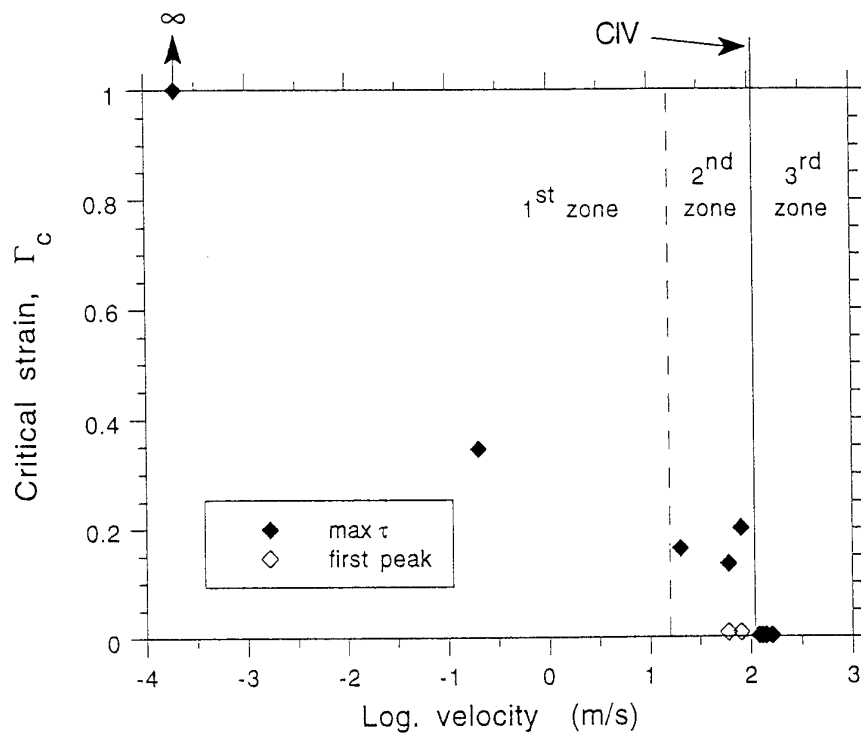


Fig. 86

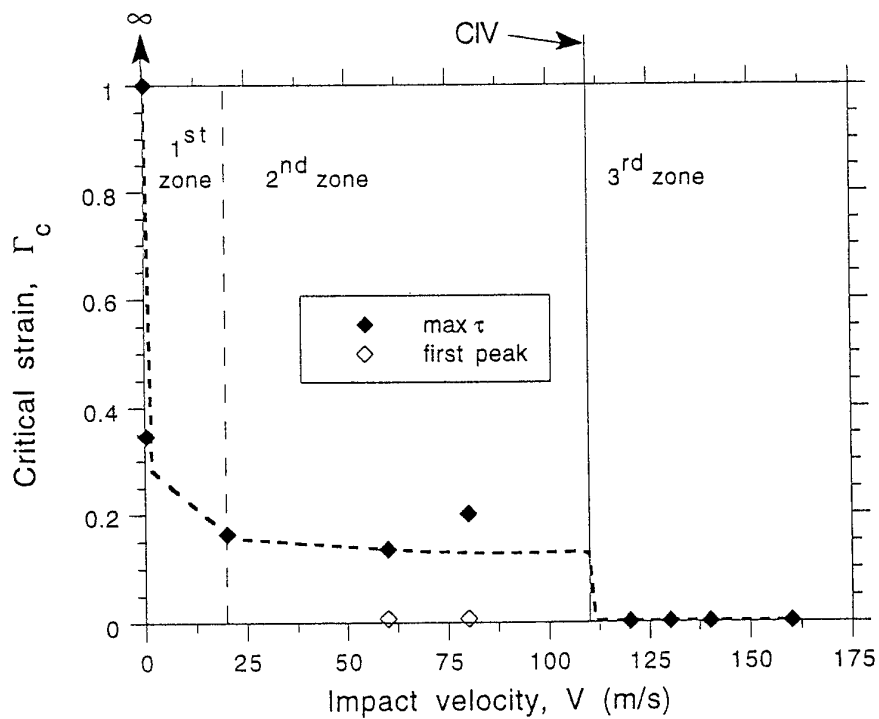


Fig. 87

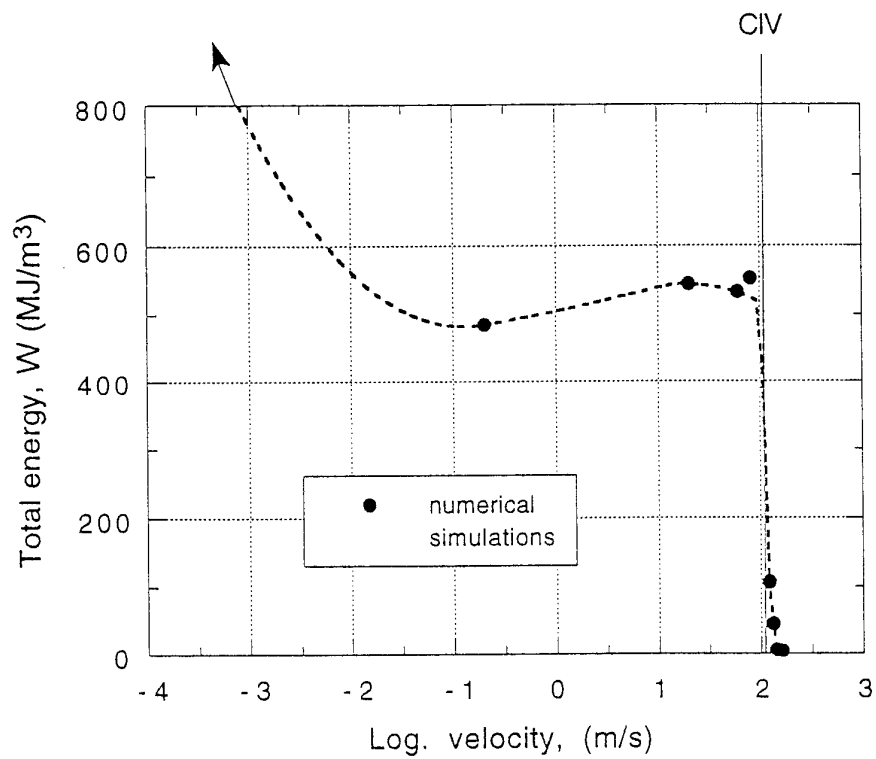


Fig. 88

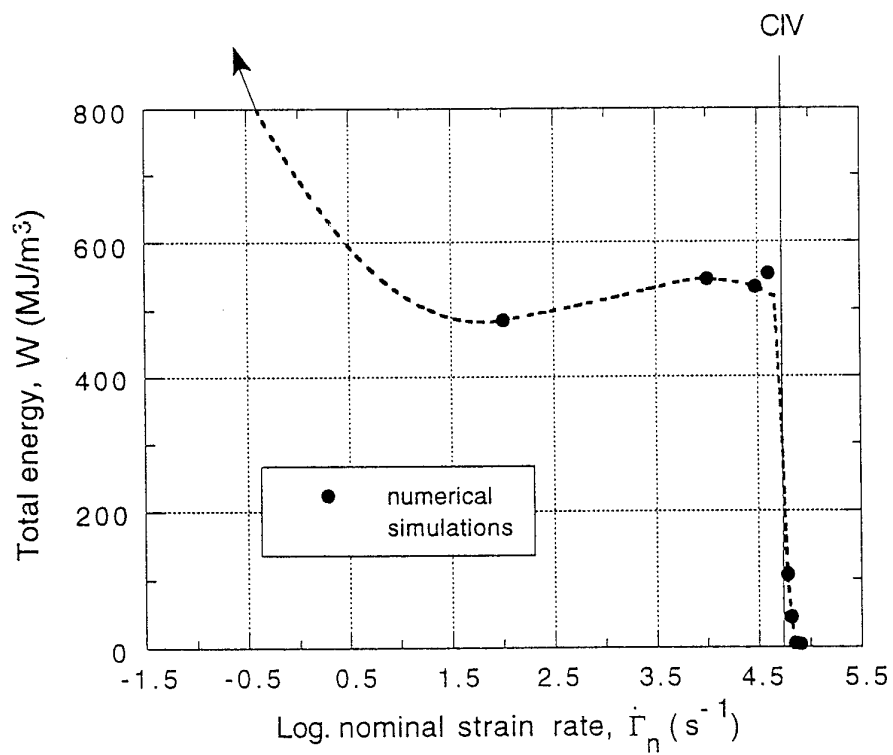


Fig. 89